



Modelling of windage and churning losses in high speed rolling element bearings

Wenjun Gao

► To cite this version:

Wenjun Gao. Modelling of windage and churning losses in high speed rolling element bearings. Mechanics [physics.med-ph]. Université de Lyon, 2018. English. NNT : 2018LYSEI048 . tel-02090821

HAL Id: tel-02090821

<https://theses.hal.science/tel-02090821>

Submitted on 5 Apr 2019

HAL is a multi-disciplinary open access archive for the deposit and dissemination of scientific research documents, whether they are published or not. The documents may come from teaching and research institutions in France or abroad, or from public or private research centers.

L'archive ouverte pluridisciplinaire **HAL**, est destinée au dépôt et à la diffusion de documents scientifiques de niveau recherche, publiés ou non, émanant des établissements d'enseignement et de recherche français ou étrangers, des laboratoires publics ou privés.



N° d'ordre NNT: 2018LYSEI048

THÈSE de DOCTORAT DE L'UNIVERSITÉ DE LYON

préparée au sein de
l'Institut National des Sciences Appliquées de Lyon

École Doctorale 162
Mécanique, Énergétique, Génie civil, Acoustique

Spécialité/ discipline de doctorat
MÉCANIQUE – GÉNIE MÉCANIQUE – GÉNIE CIVIL

Soutenue publiquement le 27 Juin, 2018, par:

Wenjun GAO

Modelling of Windage and Churning Losses in High Speed Rolling Element Bearings

Devant le jury composé de:

M. ARGHIR	Professeur (Université de Poitiers)	Rapporteur
J.L. BOZET	Professeur (Université de Liège)	Rapporteur
D. NELIAS	Professeur (INSA de Lyon)	Directeur de thèse
L. ZHANG	Associate Professeur (NWPU)	Examineur
Y. MARCHESSE	Professeur (ECAM)	Examineur
N. BOISSON	Professeur (INSA de Lyon)	Examineur
D. LECOUVREUR	Ingenieur, expert roulements(SAFRAN)	Examineur

LaMCoS - UMR CNRS 5514 - INSA de Lyon
20, avenue Albert Einstein, 69621 Villeurbanne Cedex (FRANCE)

Département FEDORA – INSA Lyon - Ecoles Doctorales – Quinquennal 2016-2020

SIGLE	ECOLE DOCTORALE	NOM ET COORDONNEES DU RESPONSABLE
CHIMIE	CHIMIE DE LYON http://www.edchimie-lyon.fr Sec : Renée EL MELHEM Bat Blaise Pascal 3 ^e étage secretariat@edchimie-lyon.fr Insa : R. GOURDON	M. Stéphane DANIELE Institut de Recherches sur la Catalyse et l'Environnement de Lyon IRCELYON-UMR 5256 Equipe CDFA 2 avenue Albert Einstein 69626 Villeurbanne cedex directeur@edchimie-lyon.fr
E.E.A.	ELECTRONIQUE, ELECTROTECHNIQUE, AUTOMATIQUE http://edeea.ec-lyon.fr Sec : M.C. HAVGOU DOUKIAN Ecole-Doctorale.eea@ec-lyon.fr	M. Gérard SCORLETTI Ecole Centrale de Lyon 36 avenue Guy de Collongue 69134 ECULLY Tél : 04.72.18 60.97 Fax : 04 78 43 37 17 Gerard.scorletti@ec-lyon.fr
E2M2	EVOLUTION, ECOSYSTEME, MICROBIOLOGIE, MODELISATION http://e2m2.universite-lyon.fr Sec : Sylvie ROBERJOT Bât Atrium - UCB Lyon 1 04.72.44.83.62 Insa : H. CHARLES secretariat.e2m2@univ-lyon1.fr	M. Fabrice CORDEY CNRS UMR 5276 Lab. de géologie de Lyon Université Claude Bernard Lyon 1 Bât Géode 2 rue Raphaël Dubois 69622 VILLEURBANNE Cédex Tél : 06.07.53.89.13 cordev@univ-lyon1.fr
EDISS	INTERDISCIPLINAIRE SCIENCES-SANTÉ http://www.ediss-lyon.fr Sec : Sylvie ROBERJOT Bât Atrium - UCB Lyon 1 04.72.44.83.62 Insa : M. LAGARDE secretariat.ediss@univ-lyon1.fr	Mme Emmanuelle CANET-SOULAS INSERM U1060, CarMeN lab, Univ. Lyon 1 Bâtiment IMBL 11 avenue Jean Capelle INSA de Lyon 696621 Villeurbanne Tél : 04.72.68.49.09 Fax : 04 72 68 49 16 Emmanuelle.canet@univ-lyon1.fr
INFOMATHS	INFORMATIQUE ET MATHEMATIQUES http://infomaths.univ-lyon1.fr Sec : Renée EL MELHEM Bat Blaise Pascal, 3 ^e étage Tél : 04.72. 43. 80. 46 Fax : 04.72.43.16.87 infomaths@univ-lyon1.fr	M. Luca ZAMBONI Bâtiment Braconnier 43 Boulevard du 11 novembre 1918 69622 VILLEURBANNE Cedex Tél : 04 26 23 45 52 zamboni@maths.univ-lyon1.fr
Matériaux	MATERIAUX DE LYON http://ed34.universite-lyon.fr Sec : Marion COMBE Tél: 04-72-43-71-70 –Fax : 87.12 Bat. Direction ed.materiaux@insa-lyon.fr	M. Jean-Yves BUFFIERE INSA de Lyon MATEIS Bâtiment Saint Exupéry 7 avenue Jean Capelle 69621 VILLEURBANNE Cedex Tél : 04.72.43 71.70 Fax 04 72 43 85 28 Ed.materiaux@insa-lyon.fr
MEGA	MECANIQUE, ENERGETIQUE, GENIE CIVIL, ACOUSTIQUE http://mega.universite-lyon.fr Sec : Marion COMBE Tél: 04-72-43-71-70 –Fax : 87.12 Bat. Direction mega@insa-lyon.fr	M. Philippe BOISSE INSA de Lyon Laboratoire LAMCOS Bâtiment Jacquard 25 bis avenue Jean Capelle 69621 VILLEURBANNE Cedex Tél : 04.72 .43.71.70 Fax : 04 72 43 72 37 Philippe.boisse@insa-lyon.fr
ScSo	ScSo* http://recherche.univ-lyon2.fr/scso/ Sec : Viviane POLSINELLI Brigitte DUBOIS Insa : J.Y. TOUSSAINT Tél : 04 78 69 72 76 viviane.polsinelli@univ-lyon2.fr	M. Christian MONTES Université Lyon 2 86 rue Pasteur 69365 LYON Cedex 07 Christian.montes@univ-lyon2.fr

*ScSo : Histoire, Géographie, Aménagement, Urbanisme, Archéologie, Science politique, Sociologie, Anthropologie

Acknowledges

This thesis is the result of a research work I have carried out between 2014 and 2018 at the Laboratory of Mechanic of Contacts and Structures (LaMCoS), funded by the China Scholarship Council.

I would like to express my gratitude to all those whole helped me during the completion of the thesis. Without their support and encourage, this thesis could not have reached its present form.

First and foremost, I want to extend my heartfelt gratitude to my supervisor, Professor Daniel NELIAS, whose patient guidance, valuable suggestion and constant encouragement make me successfully complete this thesis. He has walked me through all the stage of the writing of this thesis. His conscientious academic spirit and modest, open-minded personality inspire me both in academic study and daily life. He gives me much help and advice during the whole process of my writing, which has made my accomplishments possible.

Second, I would like to express my hearfelt gratitude to Mr. Nicolas BOISSON and Prof. Yann MARCHESSE, who do me a great favor in the work of this thesis. We have exchanged so many interesting discussions.

Also, I would like to express my sincere gratitude to all the persons that have contributed to this work, in many different manners: Alain COMBESURE, Fabrice VILLE, Lv ZHAO, Shaocheng ZHU, Wenfeng YE, Ye LU.

A special thanks for all of my friends that are present in the laboratory: Alexis BONETTO, Chao ZHANG, Deqi LIU, Lihan XIE, Meng WANG, Sami LACROIX, Shuai CHEN, Sonde Abayomi Emmanuel, Thomas JAILIN, Wenqi ZHU. They have allowed me to enjoy coffee breaks, lunches and so many other pleasant times. I hope continuing to see you regularly.

I wish to thank all professors who have taught me in this institute. Their instructions have helped broaden my horizon and their enlightening teaching has provided me with a solid foundation to accomplish this thesis and will always be of great value for my future career and academic research.

I would also like to thank the China Scholarship Council for supporting my study and life in Frence.

Last but not least, I would like to express my special thanks to my parents, whose care and support motivate me to move on and make me want to be a better person. A very special thanks to my wife Miao for her love, her support and for giving me so many reasons to be happy.

Abstract

In a rotating machinery system like turbine engine, high speed rolling element bearings play an important role in supporting the rotating shaft or rotor, and need lubrication to insure their function. Except a small quantity of oil is needed to form the elastohydrodynamic lubricant film in the contact zone, most of lubricant remains in suspension in air, forming an oil/air mixture. This phenomenon leads to excessive parasitic hydraulic losses when rolling elements translate and rotate into the fluid environment, which may constitute a relatively large portion of the bearing's total power loss, named windage drag and churning losses. For high speed applications, i.e. for rotational speed up to 3×10^6 Ndm, the contribution of drag/windage loss to the total one may reach up to 50%. However, so far there are few approaches used directly for drag and churning losses estimation, which could only provide a rather gross approximation.

In this thesis, the Computational Fluid Dynamics (CFD) method is employed to analyze first the flow around one finite-length circular cylinder with two free ends in an open space. Then the model is changed to several in-line circular cylinders sandwiched by two flat walls, which represents a simplified approach. The fluid here is regarded as incompressible, representing an equivalent one-phase fluid for the oil/air two-phase flow inside the bearing cavity with specified fluid properties. The results indicate that the flow around the finite length roller element is perturbed by its two free ends, the surrounding rings, the cage and other rolling elements. A relationship between the drag coefficient and the Reynolds number suitable for circular cylinder in roller bearings ($1 < L/D < 6$) is proposed, as well as a formulation for churning losses prediction.

The oil/air two phase flow inside the bearing cavity with under-race lubrication is also studied in this work. The coupled level-set volume of fluid (CLS-VOF) method is employed to demonstrate the lubricant distribution along the bearing circumference. The effect of various factors is studied, e.g. the oil injection velocity, the nozzle diameter, the oil properties, and the oil injecting angle. Rotational speed of all the bearing components are studied particularly to quantify their influence to the oil volume fraction inside the bearing cavity. The results demonstrate that not only the inner-ring relative rotational speed, but the cage speed itself could change the oil distribution. The results can be used for the precise lubrication design to optimize the oil distribution inside the bearing.

KEYWORDS: Numerical simulation, Rolling element bearing, Drag coefficient, Churning moment, Finite length, Free ends, Reynolds number, Oil volume fraction, Two-phase flow

Contents

Contents	i
List of Figures	iii
List of Tables	vii
General introduction	1
1 State of the art	5
1.1 Windage drag force in roller bearings	7
1.1.1 Drag coefficient of the cylinder	7
1.1.2 Flow behavior around the two-dimensional cylinder	8
1.1.3 Flow behavior around the finite-length circular cylinder	11
1.1.4 Drag coefficient of circular cylinder in roller bearings	14
1.2 Churning moments in roller bearings	16
1.2.1 Churning moment on the cylinder cylindrical surface	17
1.2.2 Churning moment on the cylinder circular ends	18
1.2.3 Churning moments in roller bearings	19
1.3 Two-phase flow in roller bearings	20
1.3.1 Two phase flow investigation in bearing chamber	22
1.3.2 Two phase flow investigation in bearing cavity	22
1.3.3 Two phase flow investigation in gearbox	24
1.3.4 The volume of fluid (VOF) model	26
1.3.5 Oil volume fraction in roller bearings	28
1.4 Novelty of this work	28
2 Flow structure around one circular cylinder with two free ends	31
2.1 Introduction	33
2.2 Numerical model	34
2.2.1 Problem definition and computational domain	34
2.2.2 The SST-SAS model and governing equations	34
2.2.3 Fluid properties	37
2.2.4 Boundary conditions	37
2.2.5 Mesh dependence	37

2.2.6	Numerical methods	37
2.3	Simulation results	38
2.3.1	Model validation	38
2.3.2	Flow pattern around the cylinder	39
2.3.3	Flow structure on the free end	42
2.3.4	Drag coefficient on the cylinder	44
2.4	Conclusions	47
3	Drag coefficient and churning moment in roller bearings	49
3.1	Introduction	51
3.2	Drag coefficient in roller bearings	51
3.2.1	The CFD model introduction	52
3.2.2	Flow around the isolated rotating cylinder	53
3.2.3	Drag coefficient of the isolated rotating cylinder	54
3.2.4	Flow around several in-line rotating cylinders	58
3.2.5	Drag coefficient of several in-line rotating cylinders	58
3.3	Churning moments in roller bearings	59
3.3.1	Churning moments on the isolated rotating cylinder	62
3.3.2	Churning moments on several rotating cylinders	71
3.4	Conclusion	79
4	Two-phase flow in bearing cavity	81
4.1	Introduction	83
4.2	Numerical model	84
4.2.1	Problem definition and computational domain	84
4.2.2	Meshes and boundary conditions	85
4.2.3	The CLS-VOF model and governing equations	86
4.2.4	Fluid properties	88
4.2.5	Numerical Methods	88
4.3	Calculation results	89
4.3.1	Nonuniform oil/air distribution	89
4.3.2	Parameters effects to oil volume fraction	90
4.4	Comparison with existing hydraulic loss models	103
4.4.1	Existing hydraulic losses prediction models	104
4.4.2	Calculation results	106
4.5	Conclusion	110
	General conclusions and perspectives	113
	Bibliography	117

List of Figures

1.1	Drag coefficient of isolated sphere and cylinder	8
1.2	Regimes of flow past a smooth two-dimensional cylinder	9
1.3	Model of a Karman Vortex Street	10
1.4	Pressure distribution around the two-dimensional cylinder with different Reynolds numbers	11
1.5	Schematic overview of flow behind a short wall mounted cylinder from Pattenden et al. [PAT 07]	13
1.6	Model of the flow field for a surface-mounted finite-height circular cylinder	13
1.7	Flow structure around the cylinder with two free ends [ZDR 89]	14
1.8	Isosurface plots of the vortical structure of the wakes behind cylinders with free hemispherical ends [SHE 04]	15
1.9	A simplified roller element bearing model	15
1.10	Drag coefficient estimated numerically and experimentally ($L=1.16D$) . .	15
1.11	Influence of the gap between consecutive balls on drag coefficient	16
1.12	Vorticity contours and streamlines of flow past three circular cylinders in tandem ($L=5D$) at $Re = 100$	16
1.13	Boundary layer on a flat plate	18
1.14	Fluid element with the thickness of δ	18
1.15	Boundary layer flow on a disk rotating in a fluid initially at rest [NEL 73]	19
1.16	Schematic of physical phenomena in bearing chamber [ZHA 15]	23
1.17	Velocity magnitude streamlines in bearing chamber [SIM 02]	23
1.18	Instantaneous oil volume fraction in a tapered roller bearing	24
1.19	The circumferential distribution of bearing cavity with different nozzle: (a) single-nozzle with seal (b) dual-nozzle with seal	24
1.20	Modelled geometry and boundary conditions[ADE 15]	25
1.21	Oil breakup into bearing chamber[ADE 15]	25
1.22	Simulation result of oil distribution around the gear	25
1.23	Simulation result of oil distribution in the gearbox	26
2.1	Geometry and boundary condition of the calculation domain	35
2.2	Cylinder in cross flow at Reynolds number of 3×10^6 : left - URANS, right - SAS, L - length scale of turbulence, D - cylinder diameter	35
2.3	View of the mesh around the short cylinder	38

2.4	Experiment test section of circular cylinder in wind tunnel [ZDR 89] . . .	39
2.5	Comparison between the simulation and experiment results with different aspect ratio	40
2.6	Pressure distribution around the circular cylinder with aspect ratio $L/D=1.5$	40
2.7	Flow patterns around the circular cylinder at $Re=45$	41
2.8	Steady-state wake behind the infinite cylinder at $Re = 40$ [SIN 10]	41
2.9	Flow patterns around the circular cylinder at $Re=450$	42
2.10	Flow patterns around the circular cylinder at $Re=4.5 \times 10^4$	42
2.11	Pressure distribution around the circular cylinder in different axis position	43
2.12	Pressure distribution around the cylindrical surface	43
2.13	Side view of stream line on the free end	44
2.14	Flow pattern from the laser light visualization on the free end surface [ROH 03]	44
2.15	Top view of stream line on the free end	44
2.16	Oil streak lines on the free end surface [ROH 03]	44
2.17	Turbulence kinetic energy distribuion on the free end with different aspect ratios ($Re = 4.5 \times 10^4$)	45
2.18	Vorticity magnitude around the circular cylinder with different aspect ratios	46
2.19	Pressure distribution around the circular cylinder with different aspect ratios	47
2.20	Drag coefficient of one circular cylinder with two free ends as a function of Reynolds number	48
3.1	Geometry and boundary condition of the configuration with one isolated cylinder (Configuration 1)	53
3.2	Geometry and boundary condition of the configuration with several in-line cylinders (Configuration 2)	53
3.3	Velocity pattern around the isolated cylinder with different rotating speed	54
3.4	Flow pattern prediction for the isolated rotating cylinder (10,000 rpm) . .	54
3.5	Flow pattern prediction for the isolated rotating cylinder (100,000 rpm) .	55
3.6	Pressure distribution around the isolated rotating cylinder (10,000 rpm) .	55
3.7	Velocity distribution around the isolated rotating cylinder (10,000 rpm) . .	55
3.8	Total pressure distribution around the isolated rotating cylinder (10,000 rpm)	56
3.9	The influence of the cylinder's rotating speed to its drag coefficient	56
3.10	The influence of the cylinder's aspect ratio to its drag coefficient	57
3.11	Drag coefficient of one isolated circular cylinder with two free ends	58
3.12	Flow pattern and velocity distribution of several in-line cylinders	58
3.13	Contour of velocity distribution around the several in-line cylinders	59
3.14	Contour of turbulent kinetic energy around the several in-line cylinders . .	59
3.15	Pressure coefficient around the single circular cylinder	60
3.16	Drag coefficient of several sandwiched in-line cylinders	60
3.17	Churning effects diagram of the rotating roller in the fluid	61
3.18	Comparison of churning moments between different calculation models . .	62

3.19	Influence of translational motion (roller orbiting) to the flow structure around the circular side (Configuration 1)	63
3.20	Influence of the roller orbital speed (i.e. the cage speed) on the churning moment (Configuration 1)	65
3.21	Influence of the roller rotational speed on the churning moment (Configuration 1)	66
3.22	Churning moment on the cylindrical surface as a function of the roller length (Configuration 1)	67
3.23	Influence of the roller aspect ratio on the churning moment (Configuration 1)	67
3.24	Churning moment on the roller as a function of the roller radius (Configuration 1)	68
3.25	Influence of the fluid density on the churning moment (Configuration 1) .	69
3.26	Influence of the fluid viscosity on the churning moment (Configuration 1)	70
3.27	Influence of the ring moving speed to churning moment on the cylindrical surface (Configuration 2)	72
3.28	Churning moment as a function of the roller orbital speed (Configuration 2)	73
3.29	Churning moment as a function of the roller rotational speed (Configuration 2)	74
3.30	Churning moment as a function of the roller length (Configuration 2) . . .	75
3.31	Churning moment as a function of the roller radius (Configuration 2) . . .	76
3.32	Churning moment as a function of the fluid density (Configuration 2) . . .	77
3.33	Churning moment as a function of the fluid viscosity (Configuration 2) . .	78
4.1	Cylindrical roller bearing structure	85
4.2	Configuration of the bearing with under-race lubrication	85
4.3	Computational mesh structure and boundary condition	86
4.4	Oil distribution evolution inside the bearing cavity with flow time	90
4.5	Oil volume fraction contours in the center cross-section with different rotational speeds	91
4.6	Oil volume fraction distributions around the circumference with different inner-ring rotational speeds	92
4.7	Simulation model for roller rotating validation	92
4.8	Average fluid density as a function of roller rotating speed	92
4.9	Oil volume fraction as a function of oil volume flow rate	94
4.10	Oil volume fraction as a function of oil inlet velocity	94
4.11	Oil volume fraction distributions with different oil inlet conditions	95
4.12	Oil volume fraction contours with different oil inlet conditions	95
4.13	Oil volume fraction distributions with different oil inlet velocity	96
4.14	Turbulence kinetic energy distributions with different oil inlet velocity . .	96
4.15	Oil volume fraction distributions with different oil inlet diameters	97
4.16	Oil volume fraction distributions around the rollers with different nozzle diameters	97

4.17	Oil volume fraction as a function of oil inlet diameter	98
4.18	Oil volume fraction distribution with different oil viscosities	98
4.19	Oil volume fraction as a function of oil viscosity	98
4.20	Oil volume fraction as a function of the bearing rotational speed	99
4.21	Oil volume fraction as a function of inner ring rotational speed	99
4.22	Oil volume fraction as a function of outer ring rotational speed	100
4.23	Oil volume fraction as a function of the cage rotational speed	100
4.24	Oil volume fraction as a function of inner ring-cage relative speed	101
4.25	Oil volume fraction distribution with different relative rotational speeds	102
4.26	Oil volume fraction distribution with a zero relative rotational speed	102
4.27	Comparison of oil volume distribution with different inlet nozzle number	102
4.28	Oil volume fraction distribution with dual-nozzle inlets	102
4.29	Oil volume fraction distributions with different oil inlet deflection angle	103
4.30	Configurations with different oil nozzle deflection direction	104
4.31	Turbulence kinetic energy distribution with different inlet nozzle deflection	104
4.32	Drag coefficient of the isolated sphere and cylinder	107
4.33	Hydraulic losses from different models at different inner ring rotating speed (Oil flow rate $2000 \text{ cm}^3/\text{min}$)	108
4.34	Hydraulic losses from different models at different inner ring rotating speed (Oil flow rate $3000 \text{ cm}^3/\text{min}$)	109
4.35	Hydraulic losses from different models at different inner ring rotating speed (Oil flow rate $4000 \text{ cm}^3/\text{min}$)	109
4.36	Hydraulic losses from different models at different oil flow rate (Inner ring rotating 72200 rpm)	110
4.37	Partial of hydraulic losses at different oil flow rate (Inner ring rotating 72200 rpm)	111

List of Tables

2.1	Roller bearing specifications	34
3.1	Index coefficient for the isolated cylinder in open space (Configuration 1)	67
4.1	Roller bearing specifications with under-race lubrication	84

General introduction

Rolling Element Bearings (REB) are key elements in turbine engines since they support the main-shaft(s), interact with the rotor dynamics through their stiffness and damping, and contribute to the safety of the whole engine in case of catastrophic events such as blade loss [HON 16]. In addition, their reliability should be optimized since the turbine engine can't operate with a broken or deteriorated bearing. This is to say that REBs in aerospace applications are very critical mechanical components that should require more attention [RUM 73]. Understanding heat generation mechanisms is a major issue for high-speed rolling element bearings (such that $N_{dm} > 10^6$) in consideration that additional heat generation and higher temperature due to excessive power losses within bearings adversely impact its contact fatigue and scuffing failure modes. Besides, the REBs play an important role for the fuel consumption and the CO₂ emission since they contribute up to 10kW per bearing to the total power losses within the engine [FER 93]. The amount of heat generated also dictates the quantity of lubricant required, as well as the capacity of the lubrication system. So that, a more efficient rotating shaft supporting system is pursued all the time, with less heat generation and hence, a better overall performance.

Sources of power loss in rolling element bearings can be classified into two groups [NEL 94]. (1) The load-dependent (friction induced) mechanical power losses are mainly due to friction losses at the loaded bearing contacts. (2) The load-independent (viscous) spin losses are caused by a host of factors including oil windage drag and churning that are present as a result of oil/air drag force and churning moment on the bearing element's surface. While there has been a large body of work dealing with load-dependent power losses [HOU 09][HUT 17], there are only a few studies available on modeling the windage drag and churning losses in rolling element bearings, which have been proven to be 50% approximately of the total power losses in bearings [FER 15].

Windage drag and churning losses are two different components of load-independent losses, or named hydraulic losses, caused by lubricant oil displacement in rolling element bearings [GUP 79]. Generally, the force exerted on the bearing element as it translates through the lubricant with the cage is called drag. It results from the shear stress by the lubricant viscosity and the compressive stress on the element [TRA 00]. Those stresses are exerted contrary to the rolling direction of the element and form the drag force. This drag force corresponds to the drag losses. And the moment imposed due to rotation of the element in the lubricant is called churning. It is mainly caused by the shearing of the oil at the rolling element surface. This churning torque corresponds to the churning losses [LIE 15].

For drag force acting on the rolling element, historically, it was taken into account using the result of one isolated element in an infinite medium by Harris [HAR 73], with a specified drag coefficient corresponding with the Reynolds number. The ball bearing is modeled by flowing past a sphere and the roller bearing is replaced by flowing past a two-dimensional cylinder, both of which are classical models in fluid dynamics. But, for ball bearing, a recent research carried by Yann and Pouly [POU 10a] contradicts this procedure as the physical behavior of high-speed REBs does not seem to be well represented. Experiments with several sets of in-line spheres show that the drag coefficient for one sphere of gap ratio similar to that in bearings was nearly divided by a factor 5 in comparison with the results for an isolated sphere.

For cylinder elements in roller bearing, this procedure is not suitable either. The model of flowing past a cylinder is two-dimensional and free of end effects. In other words, the wake structure, properties, and velocities do not change along the cylinder span. But, the circular cylinder in roller bearings is finite-length and there are two free-side ends submerged in the fluid. The flow that separates from the free ends interacts strongly with that on the cylindrical surface and results in a three-dimensional flow. Not only that, but the cylinder is sandwiched by two rings with micron-size clearance so that the air-oil mixture in bearing cavity could only flow bypass the free ends rather than the cylindrical surface. Besides, flow past several in-line cylinders could interact with each other, as found in ball bearings. As a result, drag coefficient for the cylinder in roller bearings has to be modeled with a fully-three-dimensional method and take the interference from all surroundings into consideration [YAN 15].

While for churning moments in rolling element bearings, the problem is even worse. Realistic estimates for churning moments on the various elements in a rolling bearing is an extremely difficult task and the various approaches used could only provide a rather gross approximation. In view of its difficulty, there is only one model proposed for cylindrical elements. Rumbarger and Filetti [RUM 73] provided an estimation of churning moment on cylindrical surface of rollers. And the churning moment on the sides of rollers is characterized by the flow over a rotating disk by von Karman. These formulas are referred by P. Gupta [GUP 12] and subsequent researchers [QIA 13][NIC 17]. However, it should be noted that in the model mentioned above, the fluid is initially assumed at rest and there is no relative translational motion between the roller and the fluid, which is entirely different with the case in an actual bearing. The interference from surrounding rings and rollers is ignored either, which has obvious effect on the flow around the rollers.

Finally, another important assumption in all the above models is that the bearing element is completely submerged in a uniform fluid having a specific viscosity and density. However, for most bearing applications, only a small fraction of the bearing cavity is filled with the lubricant oil, therefore, the effective contribution to drag and churning effects is made by an oil-air mixture. Traditionally, in rolling element bearing analysis, the two-phase mixture is equivalent to a one-phase fluid with an effective viscosity and density, relied on the oil/air volume fraction, which is difficult to be measured directly by experiments.

To sum up, most of the published models or formulas to predict windage drag and

churning losses are dependent on dimensional analysis of experiments or approximate hydrodynamic formulations. They provide only a first approximation to the actual losses in a bearing and the values predicted by the formulas are intended to be used only to establish general trends in a parametric design study. Knowing that 50% approximately of the power losses in rolling element bearings is due to churning and windage drag forces and torques, only empirically estimated nowadays, one can see the great advantage of developing a more reliable method to deeper understand where these losses come from.

It should be emphasized that, in view of the complicated internal geometry of the bearing and the operating conditions, a direct testing of hydraulic losses or visualization of the oil flow in rolling element bearings is difficult as yet [WU 16]. But, thanks to the recent developments in the computer science [KAJ 16], simulations are becoming an increasingly approach that can help the investigation. In last decade, a series of numerical studies are reported on the fluid dynamics in rolling element bearings and transmission gears with reliable results[CON 15][WU 17]. It demonstrates that the computational fluid dynamics (CFD) method is effective and efficient for this type of problem. In response to these facts, an aim is set to develop a more reliable and accurate estimation formulas for drag force and churning moments calculation in rolling element bearings with the numerical method. Besides, the oil/air two-phase flow inside the bearing cavity will be revealed as well, based on a numerical two-phase flow simulation. And in this thesis, the research is focused on the high-speed cylindrical roller bearings.

The first part of this work aims at proposing a more appropriate calculation model for drag force and churning moments on the cylinder element in roller bearings in a uniform flow environment. In roller bearings investigation, drag losses and churning losses, two parts of hydraulic losses, are often confused and it's difficult to distinguish them by experimental test. Besides, most available classical fluid dynamics models are not suitable directly for roller elements in bearings, which run in a special condition. Consequently, it's necessary and valuable to build one numerical model especially for roller bearings analysis and develop a more suitable estimation model for windage drag force and churning moments in roller bearings.

In Chapter 2, a simplified configuration is studied initially, with one isolated finite-length circular cylinder with two free ends in open space. The SST-based Scale-Adaptive Simulation (SST-SAS) model is used to solve this unsteady turbulent flow. This numerical model is then validated with a series of experimental test data. The effect of two free ends is demonstrated and for the application of roller bearings, the effect of the cylinder's aspect ratio to the flow is studied, together with the Reynolds number. The simulation results show that, the flow structure is changed completely by two free ends, compared with the infinite-length cylinder and the mounted cylinder with one free end.

In Chapter 3, the calculation configuration is changed to close to a real bearing, with several in-line circular cylinders sandwiched by two flat walls. With the periodic boundary condition, endless orbiting rollers sandwiched by two rings in bearing are represented. Then, the CFD method developed in Chapter 2 is conducted to quantify the influence of various factors on drag coefficient and churning moments on the cylinder, including operating conditions, roller geometry parameters, and fluid properties. A new relationship

of drag coefficient vs Reynolds number is obtained suitable for roller bearings. And a numerical-based formulaion is proposed for churning loss prediction in roller bearings.

The second part of this work focuses on the oil/air two-phase flow inside the bearing cavity. Motion of the many moving parts within the bearing cavity, in particular the pumping action of the rollers, will tend to induce an oil/air mixture within the bearing cavity, however its oil phase volume fraction is unknown. In Chapter 4, the numerical domain of the flow field inside the bearing cavity is built and a preliminary attempt is carried to analyze oil distribution after injecting from the rotating inner ring with the Coupled Level-Set Volume Of Fluid (CLS-VOF) model. As the simulation result is sensitive to the geometry structure and boundary conditions, only changing tendency of oil volume fraction versus different factors is valuable in view of the absence of experimental validation.

A general conclusion and perspectives of this work will be given at the end of this manuscript.

Chapter 1

State of the art

This chapter contains three parts, it presents the current situation of drag force, churning moments, and two phase flow research in high speed roller bearings. And its problem is put forward as well.

Contents

1.1	Windage drag force in roller bearings	7
1.1.1	Drag coefficient of the cylinder	7
1.1.2	Flow behavior around the two-dimensional cylinder	8
1.1.3	Flow behavior around the finite-length circular cylinder	11
1.1.4	Drag coefficient of circular cylinder in roller bearings	14
1.2	Churning moments in roller bearings	16
1.2.1	Churning moment on the cylinder cylindrical surface	17
1.2.2	Churning moment on the cylinder circular ends	18
1.2.3	Churning moments in roller bearings	19
1.3	Two-phase flow in roller bearings	20
1.3.1	Two phase flow investigation in bearing chamber	22
1.3.2	Two phase flow investigation in bearing cavity	22
1.3.3	Two phase flow investigation in gearbox	24
1.3.4	The volume of fluid (VOF) model	26
1.3.5	Oil volume fraction in roller bearings	28
1.4	Novelty of this work	28

In a rotating machinery system like turbine engine, roller bearings play an important part to support the rotating shaft or rotor. To keep its long time steady running, lubricant oil is needed to lubricate the friction contact and cool bearing components to a required temperature. In bearing cavity, only a small quantity of oil is needed to form the elastohydrodynamic lubricant (EHL) film in the contact zone, the EHL film thickness being less than a few tenth of micrometer. Most of lubricant remains in suspension in air, forming an oil/air mixture like a fog, which contributes to cool down the bearing components – with an effect somewhat proportional to the oil flow – but also acts as a heat source for high speed applications with an increase of dissipation roughly proportional to the square of the rotational speed. This phenomenon leads to excessive parasitic hydraulic losses when rolling elements translate and rotate into the fluid environment, which may constitute a relatively large portion of the bearing's total power loss, named windage drag and churning losses. For high speed applications, i.e. for rotational speed up to 3×10^6 Ndm, the contribution of drag/churning loss to the total one may reach up to 50%. This can be easily observed with a test bench by measuring the input shaft torque when shutting off the oil feed.

As has been mentioned at the Introduction, the force exerted on the bearing element as it translates through the lubricant causes the windage drag loss, and the moment imposed due to rotation of the element in the fluid environment leads to the churning loss. Up to now, several formulas have been proposed for computing drag force and churning moments in roller bearings, based on either classical fluid dynamics theories or experimental tests, and they could provide a first approximation to the actual hydraulic losses in bearings.

1.1 Windage drag force in roller bearings

For drag force acting on roller elements in bearings, Harris used the results for one isolated circular cylinder immersed in a uniform flow, which is one of classical problems in fluid mechanics [HAR 06]. The oil/air mixture in the bearing cavity is replaced by a fluid with specified characteristics and the effect of all surroundings is ignored. When the roller moves through the fluid environment, a shear stress is produced by the gradients of velocity at the surface of the roller with the no-slip condition. The shear stress sums to one part of the total drag force on the roller, called the viscous drag. Besides, the pressure of the fluid is greater on the front of the roller than on the back, which introduces the other part, called the pressure drag or form drag [MAL 14]. It should be emphasized that the model Harris used is two-dimensional which means that the cylinder is infinite-length and without free-ends effect.

1.1.1 Drag coefficient of the cylinder

The drag force acting on the cylinder is often non-dimensionalized as a function of Reynolds number. At very low Reynolds numbers (Re), the drag is mainly due to friction.

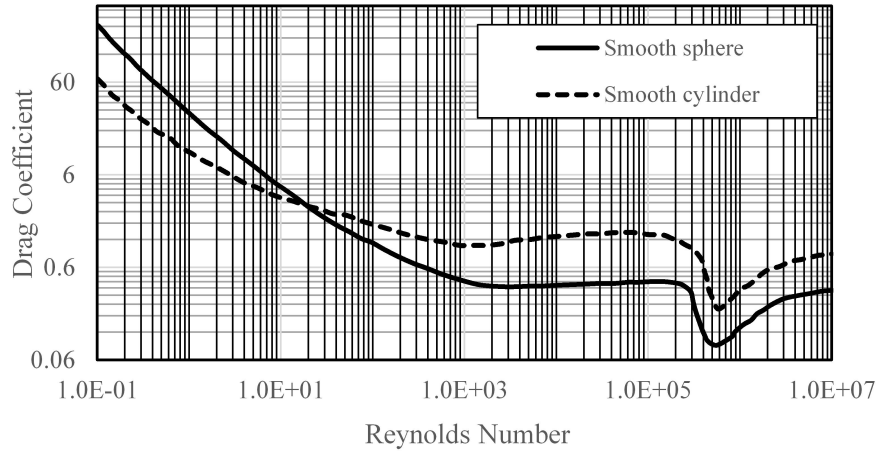


Figure 1.1: Drag coefficient of isolated sphere and cylinder

With the increase of Re , the contribution of the inertia forces begins to grow so that at high Reynolds numbers, the skin friction constitutes just a few percent of the total drag. A dimensionless expression of the total drag force is the drag coefficient defined by

$$C_d = \frac{F_d}{\frac{1}{2}\rho V^2 A} \quad (1.1)$$

Where ρ is the fluid density and A is the frontal area expressed by the body to the flow direction.

The relationship between the drag coefficient and the Reynolds number for one single element in the flow has been showed analytically and confirmed experimentally by many researchers [ABR 70][PAR 98]. As shown in the Figure 1.1, the full line is for one isolated sphere and the dash line is for the two-dimensional cylinder. Up to now, these two lines are referred by most researchers in the drag force calculation of rolling element bearings [LEB 09].

These two lines are separated to a series of flow regimes when going from small to large Reynolds numbers [PAT 85]. In the low Reynolds number range, C_d decreases significantly with increasing Reynolds number, mostly due to the skin friction contribution. In the subcritical regime, the drag coefficient changes insignificantly with Re . As the critical flow regime is reached, the drag coefficient decreases sharply with increasing Re . The wake becomes narrower by the turbulent boundary layer and the associated delayed separation. At higher Re , C_d is increasing again probably due to the development of a turbulent boundary layer already close to the front stagnation point.

1.1.2 Flow behavior around the two-dimensional cylinder

The changing of drag coefficient is corresponding with the flow structure developing around the cylinder, which is of fundamental importance for this fluid problem. The

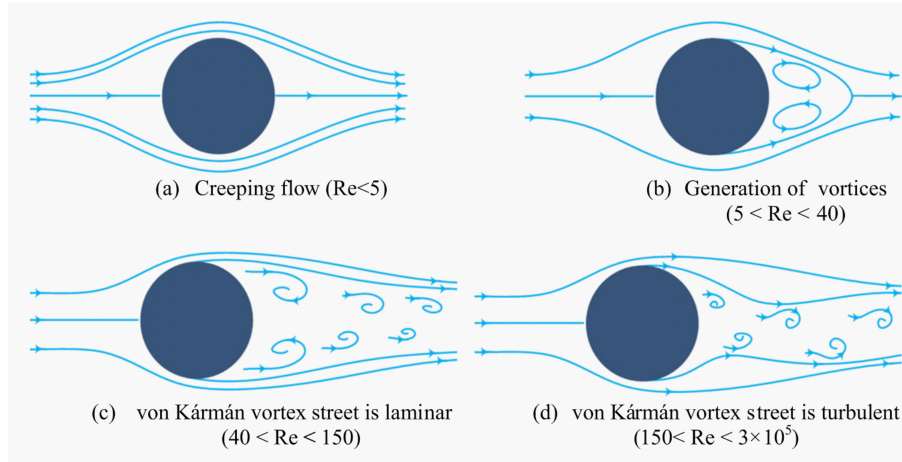


Figure 1.2: Regimes of flow past a smooth two-dimensional cylinder

flow pattern around the two-dimensional cylinder is complicated and the relative importance is expressed by the Reynolds number, as well, relied on the cylinder diameter d , the kinematic viscosity of the fluid μ , and the undisturbed free-stream velocity V . Recall that the Reynolds number represents the ratio of inertial to viscous forces in the flow, which reads

$$Re = \frac{\rho V d}{\mu} \quad (1.2)$$

As the fluid approaches the front side of the cylinder, the fluid pressure rises from the freestream value to the stagnation point value. The high pressure forces the fluid to move along the cylinder surface and boundary layers develop on both sides. The pressure force is counteracted by viscous forces and the fluid cannot follow the cylinder surface to the rear side but separate from both sides of the cylinder and form two shear layers. The innermost part of the shear layers is in contact with the cylinder surface and moves slower than the outermost part. As a result, the shear layers roll up. The flow pattern is dependent on the Reynolds number, and in Figure 1.2 principal description of the various occurring flow phenomena is provided [GOH 14].

At Reynolds numbers below 1, no separation occurs. The viscous forces cause the streamlines to move further apart on the downstream side than on the upstream side of the cylinder. In the Reynolds number range of $5 \leq Re \leq 45$, the flow separates from the rear side of the cylinder and a symmetric pair of vortices is formed in the near wake [SCH 96].

As the Reynolds number is further increased the wake becomes unstable and vortex shedding is initiated. At first, one of the two vortices breaks away and then the second is shed because of the nonsymmetric pressure in the wake. The intermittently shed vortices form a laminar periodic wake of staggered vortices of opposite sign. This phenomenon is often called the Karman vortex street [SUN 09]. Von Karman showed analytically and confirmed experimentally that the pattern of vortices in a vortex street follows a mathematical relationship, namely,

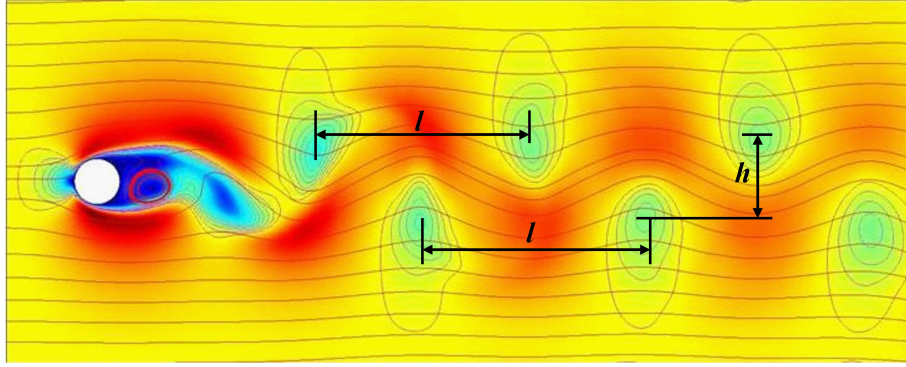


Figure 1.3: Model of a Karman Vortex Street

$$\frac{h}{l} = \frac{1}{\pi} \sinh^{-1} \{1\} = 0.281 \quad (1.3)$$

where h and l are explained in Figure 1.3.

In the Reynolds number range $150 < Re < 300$, periodic irregular disturbances are found in the wake. The flow is transitional and gradually becomes turbulent as the Reynolds number is increased.

The Reynolds number range $300 < Re < 1.5 \times 10^5$ is called subcritical (the upper limit is sometimes given as 2×10^5) [ROS 61]. The laminar boundary layer separates at about 80 degrees downstream of the front stagnation point and the vortex shedding is strong and periodic.

With a further increase of Re , the flow enters the critical regime [KAW 84b]. The laminar boundary layer separates on the front side of the cylinder, forms a separation bubble and later reattaches on the cylinder surface. Reattachment is followed by a turbulent boundary layer and the separation point is moved to the rear side, to about 140 degrees downstream the front stagnation point. As an effect the drag coefficient is decreased sharply.

For $Re \geq 6 \times 10^5$, the laminar to turbulent transition occurs in a nonseparated boundary layer, and the transition point is shifted upstream [KIM 15].

Corresponding with the different flow regimes, the various flow phenomena are reflected in the pressure distribution on the cylinder surface. Figure 1.4 provides a few distributions of the pressure coefficient C_p and the changes in the distributions are explained by the flow mechanisms described previously [SUN].

Particularly for $Re = 6.7 \times 10^5$, the separation of the laminar boundary layer and the reattachment is believed to be reflected in the behavior between $\theta \approx 100$ -110 degrees downstream the front stagnation point.

The nonsymmetrical pressure distribution results in a net force on the cylinder, and the existence of this force is the main cause of the pressure drop across the cylinder.

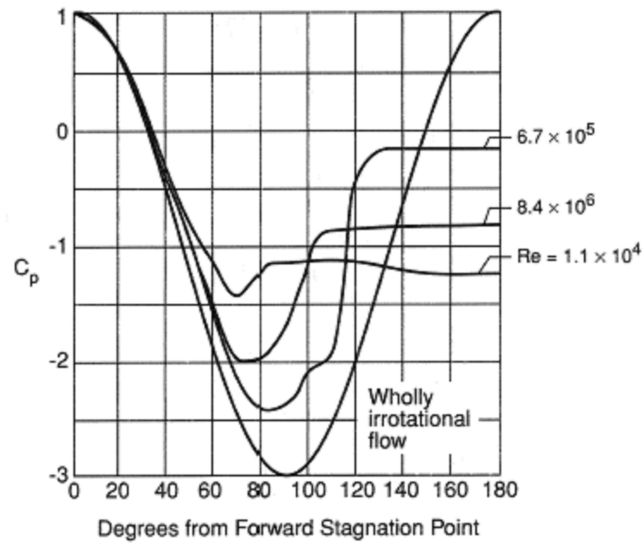


Figure 1.4: Pressure distribution around the two-dimensional cylinder with different Reynolds numbers

1.1.3 Flow behavior around the finite-length circular cylinder

Despite the two-dimensional infinite circular cylinder in a steady cross-flow is well-studied and a wealth of information about the flow behavior has been presented by many researchers, its results could not be used for the cylinder element in roller bearings directly, which is finite-length with two free ends [KUM 18]. Like the cylindrical element in roller bearings, in most practical applications there is at least one free end (chimney stacks, gas and oil storage reservoirs, etc), and sometimes two free ends (ship radar aerials, submerged vehicles, fibres, etc) [SUM 13][VAK 09]. When the cylinder is referred as finite length, its flow is effected by the end and then, the wake structure, properties, and velocities would change along the cylinder span [PAR 00].

For the flow around a finite circular cylinder mounted on the flat plate, remarkable research has been devoted to understand its characteristics [HES 03]. This finite-length circular cylinder has only one free end and a junction region between the cylinder and the flat wall. The flow pattern around the finite circular cylinder involves a horseshoe vortex system in the body-plate junction with its development downstream near the wall, a Karman-type vortex shedding in the main wake, and a three-dimensional separated flow structure around the free end surface [LEV 12].

Horseshoe vortices

Some of the early experimental studies of the flow around a wall-mounted cylinder was carried out by Baker [BAK 85]. He identified a horseshoe vortex system consisting of multiple vortices originating from the front of the wall-cylinder junction. These vortices wrap around the body moving downstream and forming a U-shaped vortex system. In the laminar case Baker identified vortex systems with 2, 4 and 6 individual vortices for

increasing Reynolds number.

Trailing vortices

Kawamura et al. [KAW 84a] focused their experimental investigations on the free end of a wall-mounted finite cylinder. They identified two trailing vortices emerging from the free end of the cylinder. For aspect ratios less than a critical ratio (L/D), these vortices, in conjunction with the horseshoe vortex system, suppress the von Karman vortex street.

It was suggested by Roh and Park [ROH 03] that there actually are four trailing vortices originating from the free end. From visualisation experiments they drew two pairs of counter-rotating vortices, where each vortex pair contains one vortex originating from the free end edge and one from the focal point at the free end surface. This proposition has been disputed by Pattenden et al. [PAT 05], Palau-Salvador et al. [PAL 10] and Krajnovia [KRA 11] who all show that there is only a single pair of vortices originating from the free end.

Arch vortex

Pattenden et al. [PAT 07] identified, experimentally and numerically, a pair of tip vortices and an arch vortex in the near wake of a short wall-mounted cylinder. This is shown in Figure 1.5 as a schematic drawing by Pattenden et al.

Frohlich and Rodi [FRÖ 04] showed that the tip vortices are joined together into the arch vortex just below the free end. This is not shown in Pattenden's figure, which otherwise gives a good summary of the flow features around a low aspect-ratio wall-mounted cylinder.

It has been found that the three-dimensional flow around the top surface developing into the wake considerably influences the wake flow pattern of the finite circular cylinder (Figure 1.5). The shedding frequency in the wake changes along the cylinder span and has minimum value in the tip region. It is caused by the existence of a cellular wake oscillating up and down in the tip region. The cellular wake originated from the vortical flow generated by the free end surface region. The fluctuating force acting on the cylinder in the traverse direction is also found to vary along the cylinder axis, as a result of the unsteady separated flow emanating from the top edge of the cylinder [KIA 16]. It is validated that the three-dimensional separated flow around the free end surface is a key element which determines the wake behavior of the finite cylinder.

For flow around a circular cylinder with two free ends, three-dimensional separated shear flow around two free ends makes the flow pattern more complex, while relatively scant attention has been attracted so far.

Okamoto & Yagita [OKA 73] assumed that an equivalent cylinder with two free ends is double of a cantilevered cylinder with one free end and it was symmetric about the plane boundary. But they ignored the combined action of two shear flow from two free ends. Without the boundary layer effect on the plate wall, the horseshoe vortex and arch-shaped vortex may change or disappear. After that, Wieselsberger and Zdravkovich [ZDR 03] experimentally measured drag coefficient and pressure distribution of one finite circular cylinder in the range $400 < Re < 8 \times 10^5$. G.J. Sheard [SHE 04] employed numerical methods to study flow past cylinder with free hemispherical ends and found that the quasi-

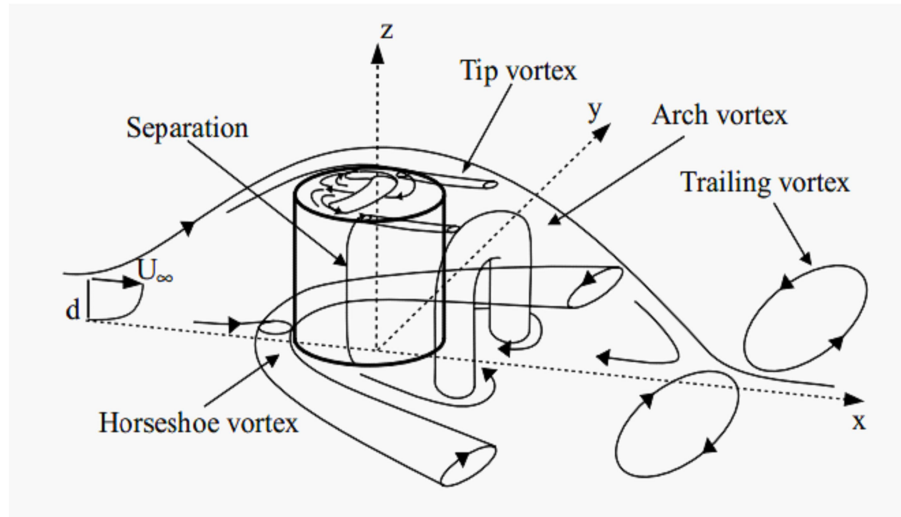


Figure 1.5: Schematic overview of flow behind a short wall mounted cylinder from Pat-tenden et al. [PAT 07]

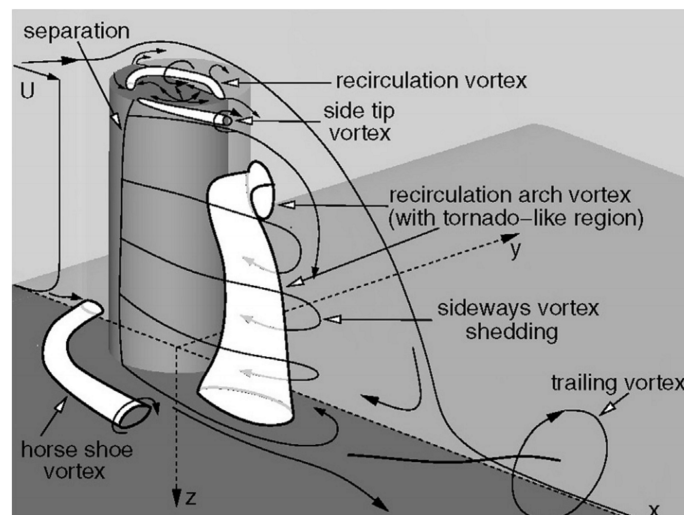


Figure 1.6: Model of the flow field for a surface-mounted finite-height circular cylinder

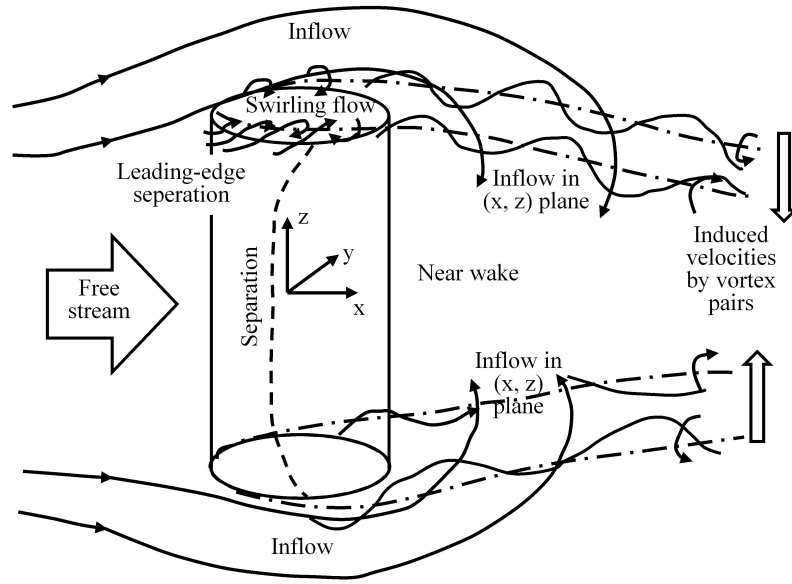


Figure 1.7: Flow structure around the cylinder with two free ends [ZDR 89]

two-dimensional wake behind the cylinder is deformed by the three-dimensional effects induced by the flow around the hemispherical ends, as shown in Figure 1.8.

It is demonstrated that the effect of two free ends on the flow past the cylinder is dramatic. Despite this, a detailed discussion on the flow around one finite circular cylinder with two free ends does not currently exist, which will be the main content of Chapter 2.

1.1.4 Drag coefficient of circular cylinder in roller bearings

Different with the isolated infinite-length or finite-length circular cylinder model, in real roller bearings, roller elements are not isolated and each one is adjacent with another two elements in up-stream and down-stream. And all rollers are sandwiched by two rings with micro-sized gap (Figure 1.9). It means that the fluid could only flow bypass the sharp edges circular ends, rather than passing through the cylindrical surface. And the vortex developing in rear side of the cylinder may be disturbed by other cylinders. As a result, for the drag force investigation, except for the two free ends, the effects from surroundings, such as the rings and adjacent rollers, should be considered as well [FLO 06].

The effect from adjacent elements has been verified in ball bearings. Yann and Pouly [MAR 14a] tested drag coefficient experimentally with several sets of in-line spheres and results show that the drag coefficient for one sphere of gap ratio similar to that in bearings was nearly divided by a factor 5 in comparison with the results for an isolated sphere, as shown in Figure 1.10 and Figure 1.11. Similar conclusion is also found in cylindrical roller bearings [HAR 10], with a two-dimensional model as shown in Figure 1.12. For the case of flow past three cylinders in tandem, it is observed that the downstream cylinder which lies in the wake of the upper cylinder experiences very large unsteady forces that can give rise to wake-induced flutter. This phenomenon is likely to be changed by the longitudinal

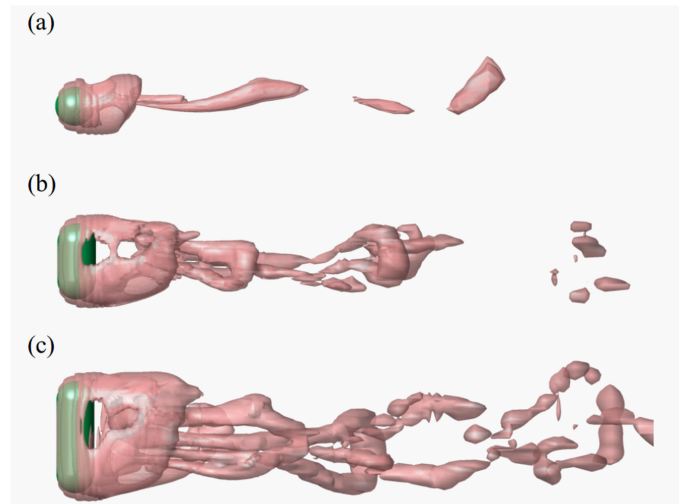


Figure 1.8: Isosurface plots of the vortical structure of the wakes behind cylinders with free hemispherical ends [SHE 04]

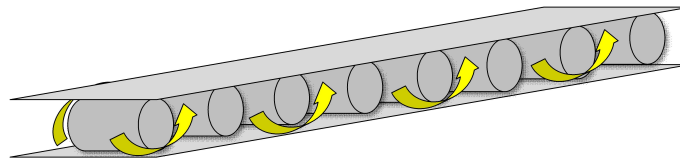


Figure 1.9: A simplified roller element bearing model

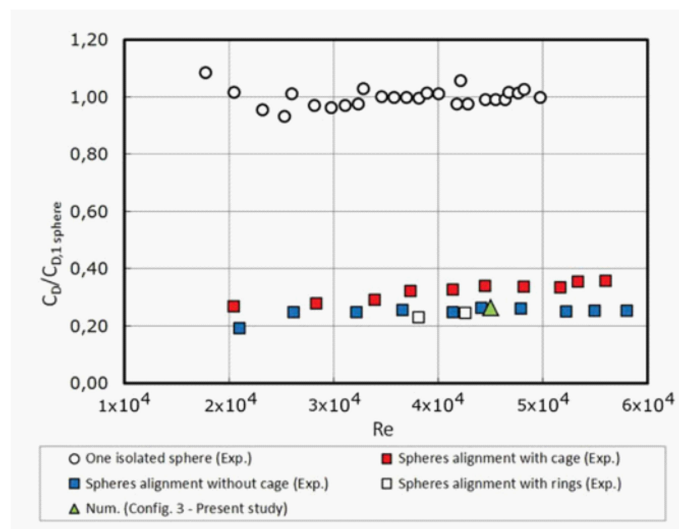


Figure 1.10: Drag coefficient estimated numerically and experimentally ($L=1.16D$)

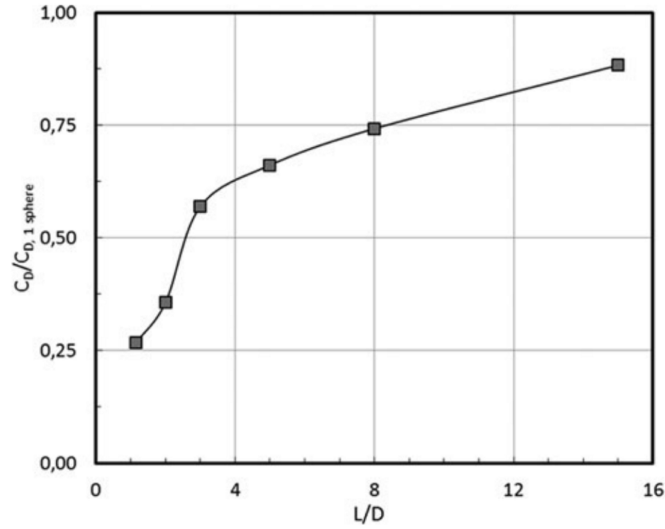


Figure 1.11: Influence of the gap between consecutive balls on drag coefficient

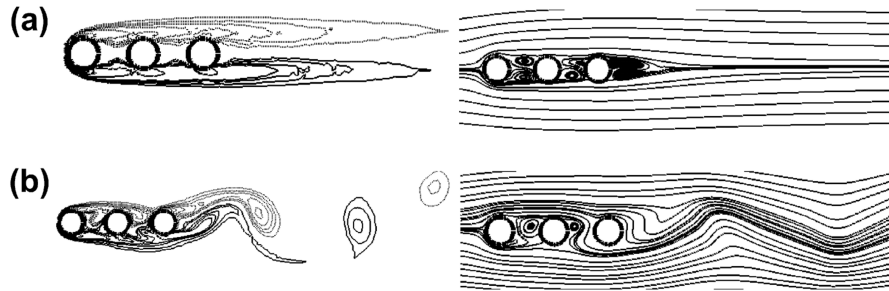


Figure 1.12: Vorticity contours and streamlines of flow past three circular cylinders in tandem ($L= 5D$) at $Re = 100$

gap.

Above all, drag coefficient for cylindrical elements in roller bearings has to be investigated with a three-dimensional model and consider the surrounding rings and rollers together, which is the main content of Chapter 3.

1.2 Churning moments in roller bearings

Churning losses in roller bearings are overlooked for a long time and few attention are focused on it individually. Like churning losses in a transmission gear pair, the rotating roller elements in bearings may cause remarkable churning losses. Generally, the moment imposed due to rotation of the cylinder element in the lubricant is called churning, which corresponds to the churning loss. Due to the difficulty in directly experimental testing, realistic estimates for churning moments in roller bearings is an extremely difficult task

and the various approaches used only provide a rather gross approximation [QIA 13]. Churning losses on a cylindrical body occur on both the cylindrical and free-end surfaces. Respectively, Rumbarger and Filetti provided an estimate of churning moment on cylindrical surface, and churning moment on the sides of rollers is characterized by the flow over a rotating disk by von Karman [VON 46]. These two models are referred by the well known computer program ADORE (Advanced Dynamics Of Rolling Elements) and bearing analysis program SHABERTH (Shaft Bearing Thermal Analysis) [NIC 17].

1.2.1 Churning moment on the cylinder cylindrical surface

From the standpoint of the dynamic solution of the interacting rollers, the most important factor is the calculation of the friction wall shear stresses on the element surfaces. In general, the moment on the cylindrical surface is described by an equation of the form:

$$M_c = \tau A r \quad (1.4)$$

Where A is the surface area; r is the reference radius from the center of rotation.

The wall shear stress, τ , is a function of the fluid properties, the motion of the surface with respect to the fluid body, and the proximity of other surfaces influenced by the same fluid. Fritz has investigated the wall shear stress phenomenon in journal bearings with vortex turbulent flow [FRI 70]. Examination of typical roller-cage clearance to roller radius ratios, and Reynolds and Taylor numbers representative of 1×10^6 DN and higher bearing operation clearly place such fluid flows in the turbulent vortex regime as defined by Fritz.

Then wall shear stress for a surface rotating in a viscous fluid is defined by the relation:

$$\tau = \frac{1}{2} f \rho U^2 \quad (1.5)$$

Where ρ is the mass density; U is the mass average velocity of the fluid; and f is the friction factor which is defined for two types of flow conditions:

Vortex turbulent flow:

$$\frac{f}{f_L} = 1.3 \left(\frac{Ta}{41} \right)_{Ta > 41}^{0.539474} \quad (1.6)$$

Couette turbulent flow:

$$\frac{f}{f_L} = 1.3 \left(\frac{Re}{2500} \right)_{Re > 2500}^{0.85596} \quad (1.7)$$

Where Re is the Reynolds number. Ta is the Taylor number.

And $f_L = 16/Re$ is the laminar friction factor for $Re < 2500$ or $Ta < 41$.

Should calculation yield a Reynolds number less than 2500, or a Taylor number less than 41, a circumstance virtually impossible in high speed roller bearings, the appropriate friction factor then can be taken as the laminar friction factor f_L . For typical high-speed roller bearings, the flow on the roller surfaces is generally best assumed as vortex turbulent.

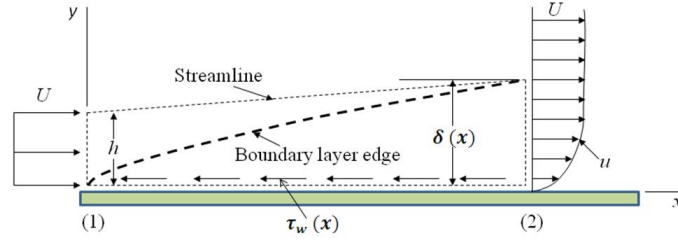


Figure 1.13: Boundary layer on a flat plate

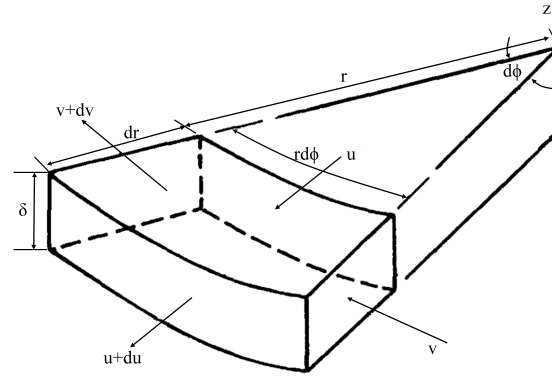


Figure 1.14: Fluid element with the thickness of δ

1.2.2 Churning moment on the cylinder circular ends

In addition to the fluid churning on the cylindrical surface, the roller ends provide an additional source of churning moment. The churning moment on the ends of rollers is characterized by the flow over a disk rotating in a fluid initially at rest [APP 15], and the boundary layer is three dimensional as shown in the Figure 1.14. As the disk begins to rotate, the fluid near the surface of the disk is strongly affected by the friction between the fluid layer, which adheres to the disk surface, and the layers of fluid which make up the boundary layer [CHU 10a].

To understand what forces contribute to the moment on a disk rotating in a viscous fluid, a disk force balance is undertaken [NEL 73].

Equations 1.8 and 1.9, are the steady-state momentum equations in the radial and circumferential directions for a differential fluid element of thickness δ . Higher order differentials have been neglected, and $p = p(z)$ has been assumed.

Radial direction

$$\frac{d}{dr} \left(2\pi r \rho \int_0^\delta u^2 dz \right) dr - 2\pi r \rho \left[\int_0^\delta \frac{v^2}{r} dz \right] dr = -2\pi r \tau_r dr \quad (1.8)$$

Where ρ is the density of the fluid, and τ is the shear in radial direction.

Circumferential direction

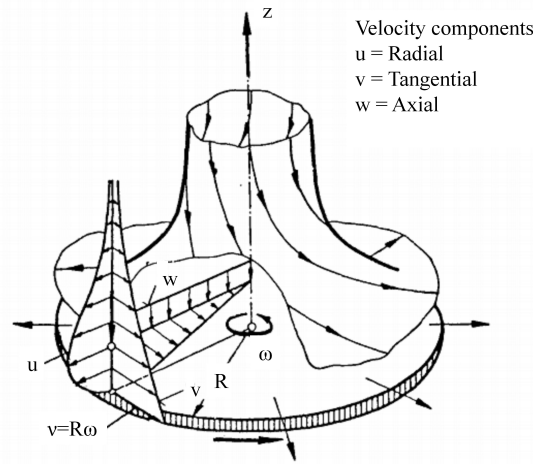


Figure 1.15: Boundary layer flow on a disk rotating in a fluid initially at rest [NEL 73]

$$\frac{d}{dr} \left(2\pi r^2 \rho \int_0^\delta u v dz \right) dr = -2\pi r^2 \tau_\phi dr = -dM \quad (1.9)$$

It is seen from Equation 1.9 that the resisting torque of a disk rotating in a fluid which is initially at rest is a measure of the circumferential shear forces acting on the disk surface and can be calculated if the radial and tangential velocities are known throughout the whole boundary layer.

By applying the boundary conditions of the flow around a rotating disk to the Navier-Stokes equations and continuity equation, von Karman and Cochran get the expression of the moment on one side of the disk:

$$M_e = \frac{1}{2} \rho \omega r^5 C_n \quad (1.10)$$

Where

$$C_n = \begin{cases} 3.87/Re^{0.5} & Re < 300,000 \\ 0.146/Re^{0.2} & Re > 300,000 \end{cases} \quad (1.11)$$

And the Reynolds number

$$Re = \frac{\rho r^2 \omega}{\mu} \quad (1.12)$$

1.2.3 Churning moments in roller bearings

In roller bearings, each roller element rotates by its own axis, and transfers along the circle runway together with the cage at the same time. Except for causing drag effect,

the roller's translational motion may change flow structure around it and then affect its churning moments. While for the models mentioned above, it should be noted that the fluid is all initially assumed at rest and there is no relative translational motion between the roller and the fluid, which is entirely different with the case in an actual bearing. Besides, similar with the drag coefficient modelling, the interference from surrounding walls and rollers is ignored either, which has remarkable effect on the flow around the roller. Therefore, a deeper understanding of the physical responsible of churning losses in roller bearings is needed to propose a more reliable estimation formula. Different parameters, e.g. roller rotational speed, roller translational speed (or called orbital speed), fluid properties, and roller geometry parameters, should be studied to quantify their effects individually, which will be presented in detail in Chapter 3.

1.3 Two-phase flow in roller bearings

Finally, another important assumption in all the above models is that the bearing element is completely flooded in a uniform fluid. It should be realized that high speed roller bearings never are completely flooded with lubricant oil, and seldom are more than 15 to 20 percent full of oil within the bearing for very high speed operation [ADE 15]. Motion of the many moving parts within the bearing, in particular the pumping action of the rollers, will tend to induce an oil/air mixture within the bearing cavity. It can be argued that for pure viscosity effects in a turbulent regime, this phenomenon will have little tendency to change the fluid behavior from that of a flooded bearing, since in general such effects are confined to relatively thin boundary layers adjacent to the surfaces.

This problem has been aware for a long time but in most bearing performance simulation tools, it's simply based on an empirical adjustment factor, to adjust the applicable density.

$$F_d = \frac{1}{2} \Phi_d C_d \rho V^2 A \quad (1.13)$$

Based on experimental experience, a value of 0.05 is typically used for many applications, like the SHABERTH [NIC 17]. Later, to improve the analytical description, an effective or equivalent air-oil density and viscosity are suggested.

$$\begin{aligned} \rho_{eff} &= (\rho_{oil} \times oilvolume + \rho_{air} \times airvolume) / totalvolume \\ &\cong \rho_{oil} \times \frac{oilvolume}{totalvolume} = \rho_{oil} \times XCAV \end{aligned}$$

$$\begin{aligned} \mu_{eff} &= (\mu_{oil} \times oilvolume + \mu_{air} \times airvolume) / totalvolume \\ &\cong \mu_{oil} \times \frac{oilvolume}{totalvolume} = \mu_{oil} \times XCAV \end{aligned}$$

Then, XCAV, the lubricating oil volume fraction in the bearing cavity, is used to instead the empirical adjustment factor Φ_d .

This method demonstrated significantly better correlation with existing experimental data than did the original Harris model. However, using of these formulas has to base on the value of oil volume fraction in bearing cavity, while the value of drag coefficients and corresponding oil volume fraction could only be adjusted together and artificially to correlate with experimental data. The calculation result is extremely sensitive to the oil volume fraction that a difference of 10 percent in oil/air ratio may produce a 2 percent difference in cage slip [SEL 11]. This may lead a significant error.

In previous, Parker [PAR 84] deduced an equation to calculate the oil percent volume in bearing cavity based on a range of experimental test. The computer program SHABERTH was used to calculate the thermal performance of three selected ball bearings for the comparison. The oil volume fraction was derived as a function of lubricant flow rate, shaft speed, and bearing pitch diameter.

$$XCAV = 10.0 \times 10^6 \frac{W^{0.37}}{nd^{1.7}} \quad (1.14)$$

Where W is the inlet oil flow (cm^3/min), n is the inner shaft speed (rpm), and d is the bearing pitch diameter (mm).

The predicted bearing heat generation, the inner- and outer-race temperatures, and oil-out temperatures agreed well with the experimental data, which proves that the predicted XCAV is reasonable. But in the program SHABERTH [RAG 80], drag coefficient used for the drag force calculation was still obtained from the model of flowing past one isolated element, which has been negated by descendants for its application in roller bearings. So that in Pouly's work [POU 10b], when drag coefficient of spheres in rolling element bearings was found to be 1/5 of that for one isolated element, the Parker's formula had to be multiplied by a factor of 5 at the same time.

$$\begin{cases} C_{dbearing} = 0.2 * C_{dsphere} \\ XCAV = 5 * 10.0 \times 10^6 \frac{W^{0.37}}{nd_m^{1.7}} \end{cases} \quad (1.15)$$

Obviously, it is unreliable to correlate drag coefficient with the oil volume fraction, which are both uncertain so far. Hence, the oil volume fraction in bearing cavity has to be studied individually, with an oil/air two-phase flow investigation, regardless of other unknown.

Except that, in Parker's model, only the inner ring is rotating and the lubricant oil is supplied from an fixed jet. Physically, the cage speed should be more important than the inner-ring rotational speed. This is of particular importance when cage skidding occurs or when the outer ring is also rotating. To account for an oil feeding through the inner ring or by an external jet that is fixed, it may be useful to consider not the absolute cage speed but the relative speed between the cage and the incident oil jet. Finally, Parker's model does not consider the effect of the roller guidance type, which should significantly affect

the quantity of oil, especially that entrapped in the bearing cavity. Therefore, the original Parker formula has been modified in the following way by G.Cavallaro [CAV 05].

$$XCAV = K_{OFT} 10^7 \frac{W^{0.37}}{n_c \frac{d_m}{d_m/2 - r} d_m^{1.7}} \quad (1.16)$$

Where n_c , is the relative cage speed (i.e., the real cage speed if the lubricant is provided through an external and fixed pipe or the difference between the inner ring speed and the cage speed if the lubricant is provided through the inner ring) and K_{OFT} is the oil feed type coefficient that equals 1 when the ring roller guides are located on the outer ring and equals 0.5 when the rollers are guided by the inner ring.

According to this definition of oil/air mixture ratio, it becomes clear that the air-oleo-dynamic force acts to drag the rollers when the lubricant is provided by an external jet and conversely acts to propel the rollers when the lubricant is provided through the inner ring. It should be mentioned that, the modification proposed by G.Cavallaro is reasonable, however, the coefficient in the changed formula lacks experimental or theoretical support.

In view of the difficulty in testing the oil flow inside the bearing cavity experimentally, the CFD method looks more feasible. The effect of the relative cage speed should be investigated in detail, no matter how the oil is supplied or how the bearing's two rings rotate.

1.3.1 Two phase flow investigation in bearing chamber

In lubrication system of turbomachinery, two phase flow exists widely, like roller bearings, gearbox, the scavenge pipe, etc. For roller bearings, the two phase flow in bearing chamber has been investigated a lot experimentally and numerically (Figure 1.16)[ZHA 15]. And the works mainly focus on oil film formation, droplet adhesion, and thermal convection. Peduto et al. [PED 11] employed the volume of fluid method (VOF) to calculate the lubricating oil movement on bearing chamber and oil return pipe wall. Chengxin and Gosman [BAI 96] and O'Rourke and Amsden [O'R 96] established oil film motion calculation models taking into account of the oil droplet/oil film interaction, evaporation of the high temperature lubricating oil, air shearing and heat transfer of air/oil film/wall, combination with the experimental results. Simmons et al. [SIM 02] applied Euler-Lagrange model as implemented in the commercial CFD package CFX4.2 to calculate the oil-gas two-phase flow and droplet trajectories in the bearing chamber (Figure 1.17), and they also analyzed the effect of shear forces to the droplet motion.

1.3.2 Two phase flow investigation in bearing cavity

Comparing to the oil/air two-phase flow in bearing chamber, the flow field inside the bearing cavity is complicated because of the strong interaction between the air flow and the lubricant oil flow which is greatly affected by the bearing rotating components. To predict the influence of lubricant displacement on the total friction torque, the Institute for

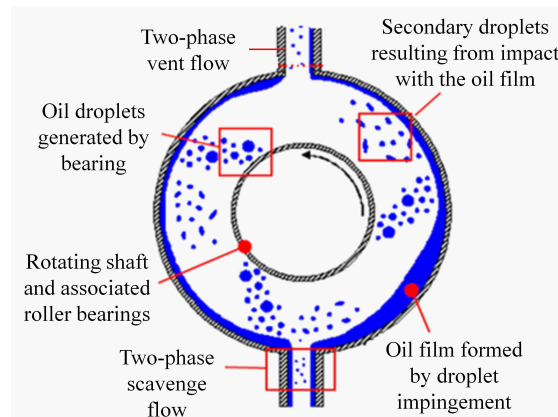


Figure 1.16: Schematic of physical phenomena in bearing chamber [ZHA 15]

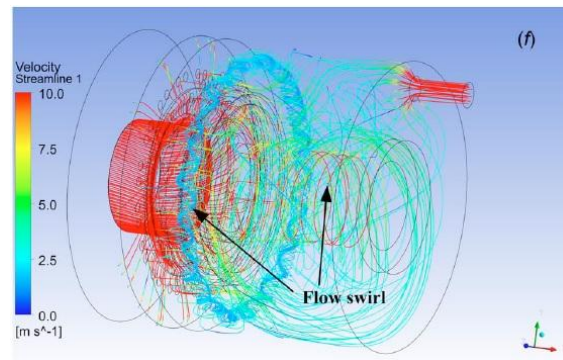


Figure 1.17: Velocity magnitude streamlines in bearing chamber [SIM 02]

Machine Elements, Gears and Transmissions (MEGT) and the Institute for Tribology and Energy Conversion Machinery (ITR) investigate the effects associated with oil lubrication on axially loaded bearings with a vertical axis of rotation [LIE 15], as shown in Figure 1.18. The solution for complex fluid mechanical tasks inside a bearing is based on the volume-of-fluid method (VOF).

Additionally, Wei Wu et al. built two experimental apparatuses for the flow pattern and temperature distribution test of the ball bearing [WU 16]. The oil/air two-phase flow in bearing cavity is numerically simulated as well, to investigate the air-oil flow inside jet cooling ball bearings and to optimize the lubrication system (Figure 1.19). The VOF method is used to track the oil distribution and the oil volume fraction. Several parameters, like the rotating speed, nozzle number, and oil volume flow rate, are tested numerically and experimentally [HU 14].

Besides, Akinola A. Adeniyi et al. [ADE 17] present a computational fluid dynamics transient simulation of the oil/air two-phase flow in the bearing cavity with an attempt boundary condition using a coupled level-set VOF approach (Figure 1.20). It is found that the rate at which oil exits in the bearings is directly proportional to the shaft speed

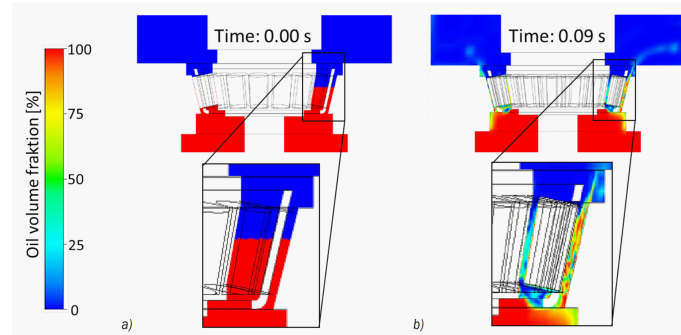


Figure 1.18: Instantaneous oil volume fraction in a tapered roller bearing

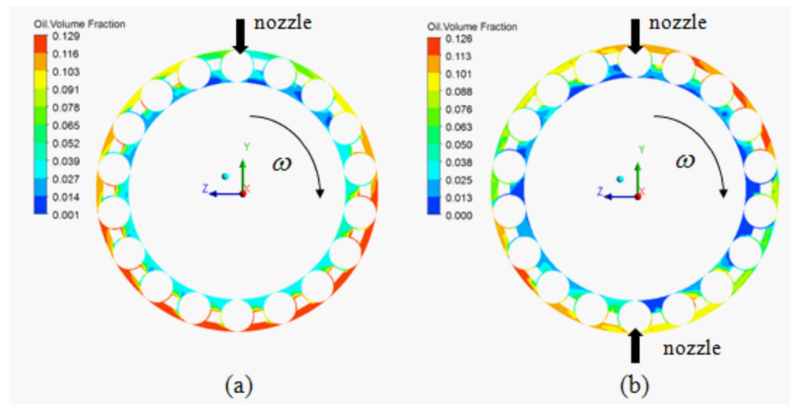


Figure 1.19: The circumferential distribution of bearing cavity with different nozzle: (a) single-nozzle with seal (b) dual-nozzle with seal

and decreases with the oil inlet flow rate, as shown in Figure 1.21.

1.3.3 Two phase flow investigation in gearbox

For the VOF method, it has been applied widely in the churning losses prediction in gear transmission system, as shown in Figure 1.22 and Figure 1.23 [FER 15][LAR 17]. Marchesse et al. [MAR 14b], Hill et al. [HIL 11], and Gorla et al. applied the VOF method in the computational fluid dynamic (CFD) simulation for studying load-independent losses of gearboxes. The results of different researchers have shown the effectiveness of the CFD approach for the characterization and the optimization of the oil distribution around gears [LIU 17a].

The validated capability developed in the earlier work has motivated the focus of the present study: to use a CFD model to interrogate the oil distribution within the bearing cavity with oil feeding through the inner ring. Thus, in the thesis, the VOF method is used to track the oil/air two-phase flow and obtain the changing rule of oil volume fraction in bearing cavity.

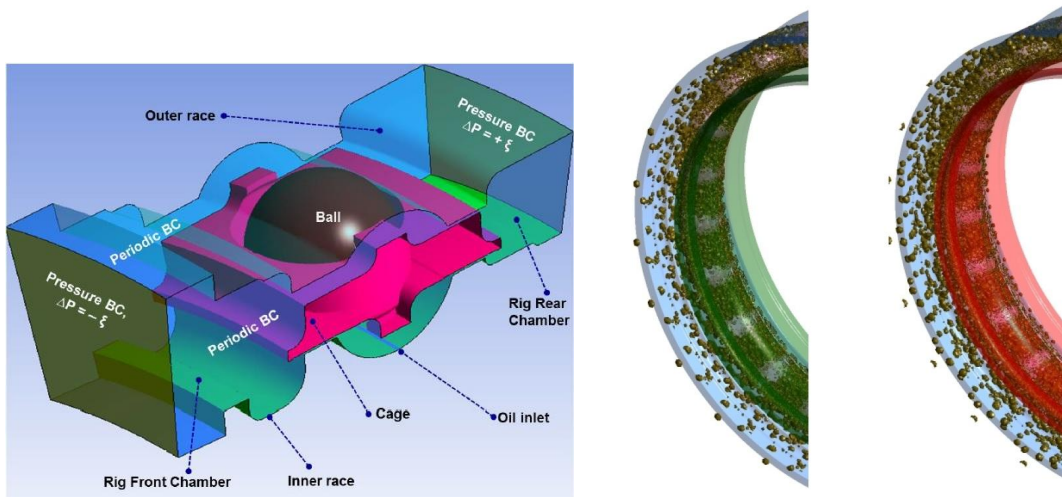


Figure 1.20: Modelled geometry and **Figure 1.21:** Oil breakup into bearing chamber[ADE 15]

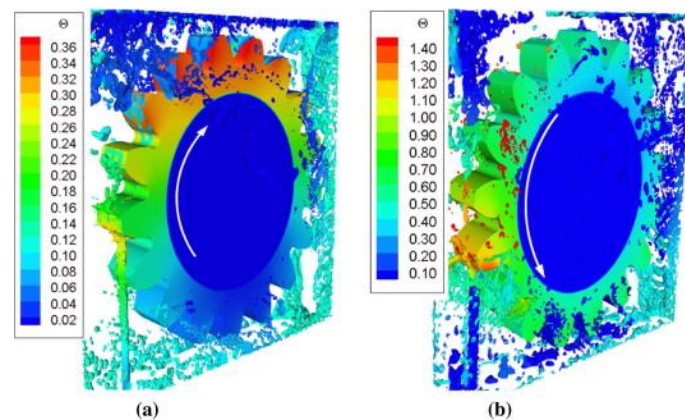


Figure 1.22: Simulation result of oil distribution around the gear

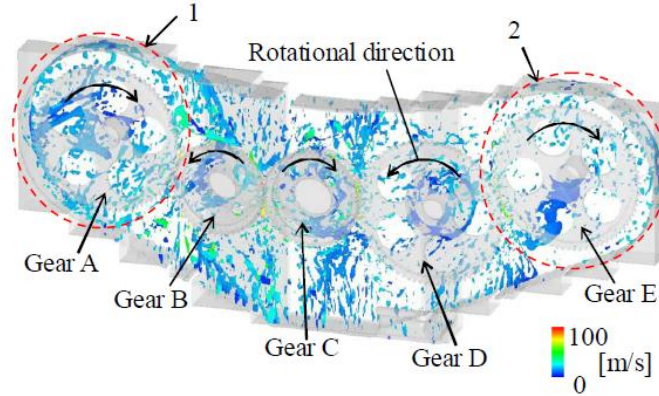


Figure 1.23: Simulation result of oil distribution in the gearbox

1.3.4 The volume of fluid (VOF) model

Like the oil/air flow in the bearing cavity, a large number of flows encountered in nature and technology are a mixture of phases. In the roller bearing cavity, the lubrication oil is injected to the gas environment and impacts on the bearing's components, splashing to countless droplets. The flow regime is gas-liquid two-phase mixture flow. Advances in computational fluid mechanics have provided the basis for further insight into the dynamics of multiphase flows. Currently there are two approaches for the numerical calculation of multiphase flows: the Euler-Lagrange approach and the Euler-Euler approach [MIC 16]. And the VOF model is one of the Euler-Euler approach models.

In the Euler-Euler approach, the different phases are treated mathematically as interpenetrating continua. Since the volume of a phase cannot be occupied by the other phases, the concept of phasic volume fraction is introduced. These volume fractions are assumed to be continuous functions of space and time and their sum is equal to one. Conservation equations for each phase are derived to obtain a set of equations, which have similar structure for all phases.

The VOF model was developed by Hirt and Nichols [HIR 81] in 1981. It can model two or more immiscible fluids by solving a single set of momentum equations and tracking the volume fraction of each of the fluids throughout the domain. It relies on the fact that two or more fluids (or phases) are not interpenetrating. For each additional phase that you add to your model, a variable is introduced: the volume fraction of the phase in the computational cell [KLE 05]. In each control volume, the volume fractions of all phases sum to unity. The fields for all variables and properties are shared by the phases and represent volume-averaged values, as long as the volume fraction of each of the phases is known at each location. Thus the variables and properties in any given cell are either purely representative of one of the phases, or representative of a mixture of the phases, depending upon the volume fraction values. In other words, if the q th fluid's volume fraction in the cell is denoted as α_q , then the following three conditions are possible:

$\alpha_q = 0$: The cell is empty (of the fluid).

$\alpha_q = 1$: The cell is full (of the fluid).

$0 < \alpha_q < 1$: The cell contains the interface between the fluid and one or more other fluids.

Based on the local value of α_q , the appropriate properties and variables will be assigned to each control volume within the domain.

The continuity equation

The tracking of the interface(s) between the phases is accomplished by the solution of a continuity equation for the volume fraction of one (or more) of the phases. For the q th phase, this equation has the following form:

$$\frac{1}{\rho_q} \left[\frac{\partial}{\partial t} (\alpha_q \rho_q) + \text{div} \cdot (\alpha_q \rho_q \vec{v}_q) \right] = S_{\alpha_q} + \sum_{p=1}^n (\dot{m}_{pq} - \dot{m}_{qp}) \quad (1.17)$$

where \dot{m}_{qp} is the mass transfer from phase q to phase p and \dot{m}_{pq} is the mass transfer from phase p to phase q .

The volume fraction equation will not be solved for the primary phase; the primary phase volume fraction will be computed based on the following constraint:

$$\sum_{q=1}^n \alpha_q = 1 \quad (1.18)$$

Noting that the properties appearing in the transport equations are determined by the presence of the component phases in each control volume. In a two-phase system, for example, if the phases are represented by the subscripts 1 and 2, and if the volume fraction of the second of these is being tracked, the density in each cell is given by

$$\rho = \alpha_2 \rho_2 + (1 - \alpha_2) \rho_1 \quad (1.19)$$

All other properties (e.g., viscosity) are computed in this manner.

The Momentum Equation

A single momentum equation is solved throughout the domain, and the resulting velocity field is shared among the phases. The momentum equation, shown below, is dependent on the volume fractions of all phases through the properties ρ and μ .

$$\frac{\partial}{\partial t} (\rho \vec{v}) + \nabla \cdot (\rho \vec{v} \vec{v}) = -\nabla p + \nabla \cdot [\mu (\nabla \vec{v} + \nabla \vec{v}^T)] + \rho \vec{g} + \vec{F} \quad (1.20)$$

One limitation of the shared-fields approximation is that in cases where large velocity differences exist between the phases, the accuracy of the velocities computed near the interface can be adversely affected.

The Energy Equation

The energy equation, also shared among the phases, is shown below.

$$\frac{\partial}{\partial t} (\rho E) + \nabla \cdot (\vec{v} (\rho E + p)) = \nabla \cdot (k \nabla T) + S_h \quad (1.21)$$

The properties ρ and k (effective thermal conductivity) are shared by the phases. The source term, S_h , contains contributions from radiation, as well as any other volumetric heat sources.

As with the velocity field, the accuracy of the temperature near the interface is limited in cases where large temperature differences exist between the phases. Such problems also arise in cases where the properties vary by several orders of magnitude. For example, if a model includes liquid metal in combination with air, the conductivities of the materials can differ by as much as four orders of magnitude. Such large discrepancies in properties lead to equation sets with anisotropic coefficients, which in turn can lead to convergence and precision limitations [KOL 11].

1.3.5 Oil volume fraction in roller bearings

With regard to the reviewed numerical work, it can be concluded that the application of the VOF method is considered to be the suitable tool for the simulation of oil flow distribution in roller bearings. In Chapter 4, a roller bearing model is established with the flow field inside the bearing cavity. The lubricant oil flow injected from the inner ring is analyzed with the VOF method, and different parameters are tested numerically to reveal the changing rule of the oil volume fraction inside the bearing cavity.

1.4 Novelty of this work

Rolling Element Bearings (REB) are very critical mechanical components in rotating machinery, that should require deep understanding of its heat generation mechanisms. Windage drag and churning losses are a major issue for high-speed rolling element bearings (such that $Ndm > 10^6$) in consideration that they may represent up to 50% of the total power dissipated.

Both measurement and prediction of windage drag and churning losses in high speed rolling bearings are extremely difficult tasks. Except several empirical total hydraulic losses prediction formulas, there are few approaches used directly for the windage drag or churning losses prediction, which could only provide a rather gross approximation.

The Computational Fluid Dynamics (CFD) method has been becoming an effective and efficient approach for this fluid mechanics problem. The numerical approach can be of considerable value to quantify the interaction between the fluid and roller elements, to demonstrate oil/air flow pattern inside the bearing cavity, and furthermore, to analyze influencing factors such as running conditions, fluid properties, the geometry parameters.

The objective of this PhD work is to develop a reliable and accurate estimation formulas for drag force and churning moments calculation in rolling element bearings with the numerical method. Three main points addressed in this thesis are:

1. The development of an accurate numerical simulation method to analyze the flow around roller elements, which is a special finite cylinder with two free ends, and surrounded by two rings and adjacent rollers.

2. The development of accurate and reliable formulas for drag coefficient and churning moments on the roller in high speed rolling bearings, in an equivalent one-phase environment.

3. The development of an accurate numerical simulation method to analyze the oil/air two-phase flow inside the bearing cavity, to illustrate the oil volume fraction varying with factors such as oil volume flow rate, oil property, bearing rotational speed, *etc.*

Point 1 and 2 will be addressed in Chapter 2 and 3. Chapter 2 presents the development of the numerical model in the CFD approach. The flow structure around one isolated finite circular cylinder with two free ends in open space is investigated in a wide range of aspect ratios and Reynolds numbers, with the SST-SAS turbulent model. Vortex structure around the cylinder is represented. This is of basic for the windage drag and churning losses investigation in roller bearings. Chapter 3 conducts the CFD method developed in Chapter 2 to predict drag coefficient and churning moments on the roller elements. A configuration with several in-line circular cylinders sandwiched by two flat walls is studied in one-phase environment, which represents a simplified approach. A relationship between drag coefficient and Reynolds number is summarized and a formulation for churning moments prediction is proposed, based on a series of tests to various factors, *e.g.* operating conditions, roller geometry parameters, and fluid properties.

Point 3 will be addressed in Chapter 4. In Chapter 4, the CLS-VOF method is proposed to track the oil/air two-phase flow inside the bearing cavity with the under-race lubrication, and furthermore, to predict the oil volume fraction, which is necessary for the one-phase flow equivalent conversion. The influence of different factors, such as the oil volume flow rate, the oil injection velocity, the lubricant oil property, and especially the bearing components rotational speed (Inner ring, the cage, outer ring, respectively). The effect of the nozzle scheme to the oil distribution along the bearing circumference is discussed as well.

The manuscript ends with a conclusion and perspectives for this work.

Chapter 2

Flow structure around one circular cylinder with two free ends

In this chapter a numerical investigation is conducted to reveal flow structure around one circular cylinder with two free ends, which is the basic for analysing of windage and churning losses in roller bearings.

Contents

2.1	Introduction	33
2.2	Numerical model	34
2.2.1	Problem definition and computational domain	34
2.2.2	The SST-SAS model and governing equations	34
2.2.3	Fluid properties	37
2.2.4	Boundary conditions	37
2.2.5	Mesh dependence	37
2.2.6	Numerical methods	37
2.3	Simulation results	38
2.3.1	Model validation	38
2.3.2	Flow pattern around the cylinder	39
2.3.3	Flow structure on the free end	42
2.3.4	Drag coefficient on the cylinder	44
2.4	Conclusions	47

2.1 Introduction

As pointed out in Chapter 1, windage drag loss in roller bearings is estimated with the model of flow around one circular cylinder in a disturbance-free stream, which has attracted a great deal of attention over the years. This approach is however too simplified since the model used previously is two-dimensional which is infinite-length and free of end effect. While the circular cylinder in roller bearing is finite-length and there are two free-side ends immersed in the oil/air two-phase fluid environment. The flow that separates from free ends may interact strongly with that from the cylindrical surface and result in a three-dimensional flow phenomena [KIA 16]. Using results of two-dimensional infinite model cannot truly capture phenomena such as alternating vortex shedding, and may cause large fluctuating pressure forces, noise, vibrations and even structural failure when the vortex shedding frequency coincides with the body's own natural frequency [KIA 16]. In fact, though the two-dimensional infinite circular cylinder in a steady cross-flow has been one of the classical problems in fluid mechanics, the flow around short circular cylinder with two free ends remains relatively unexplored.

Investigation results of flow around one mounted circular cylinder show that, the existing of free end makes the problem more complicated, with highly turbulent vertical structures in the flow field around the cylinder [BLA 15]. For circular cylinder with two free ends, despite the geometry is simple, the interaction between the flow separating from two free ends and the wake separating from the cylindrical surface is not well understood. In addition, as the roller in bearings, in most practical applications there is at least one free end and sometimes two free ends, such as ship radar aeriels, etc [SUM 13]. Such a flow configuration represents a more realistic situation. Therefore, understanding the dynamics of three-dimensional flow around one circular cylinder with two free ends can provide valuable basic fluid mechanical knowledge, accompanying with both fundamental and practical importance.

So far, a detailed discussion on the flow around one finite circular cylinder with two free ends does not currently exist. Hence in this chapter, a numerical modelling method is presented to explore its flow pattern and turbulent structure primarily, to build the basic for windage drag and churning losses investigation in roller bearings [JAV 14]. Turbulent flow over the cylinder with different Reynolds numbers and different aspect ratios is studied and compared with previous work. The influence of two free ends on the pressure distribution and drag coefficient is analyzed. The present numerical study will add significantly to our understanding of the flow around one finite circular cylinder with two free ends.

This chapter is structured as following. Section 2.2 presents the numerical method for the flow simulation. The computation domain is defined with corresponding boundary conditions. The SST-based Scale-Adaptive Simulation (SST-SAS) model is introduced, which is used to catch the detail of vortices in the fluid field in acceptable calculation time. Some setup to solve the complicated problem is presented in the employed commercial software ANSYS Fluent.

In section 2.3, the CFD simulations are carried out to model flow structure around the

Tableau 2.1: Roller bearing specifications

Pitch diameter(mm)	48.5
Bearing width (mm)	14
Number of rollers	16
Roller diameter(mm)	7.14
Roller length(mm)	10

finite-length circular cylinder with two free ends. Experimental data from other literatures is used to validate the numerical model. Then flow structure and pressure distribution around the cylinder are demonstrated. Its characteristics with different aspect ratios are discussed and explained. This work builds the foundation for numerical investigation of windage drag and churning losses in roller bearings in the following chapters.

2.2 Numerical model

2.2.1 Problem definition and computational domain

To simulate flow structure around one finite circular cylinder with two free ends, a simplified ideal model is built, with one isolated finite-length circular cylinder in a domain without wall effects. The geometry of calculation fluid domain and the boundary condition are shown in Figure 2.1. The cylinder center is placed 5 times diameter of the cylinder (5D) downstream of the inlet and 15D upstream of the outlet. The other four sides are 5D far from the center of the cylinder, far enough away from the cylinder to have a uniform far field flow. The aspect ratio is defined as the length to diameter ratio L/D . The roller and corresponding bearing specification used in the numerical investigation is listed in Table 2.1. The fluid domain is dispersed with structured hexahedron grid with the software ANSYS ICEM 16.9.

2.2.2 The SST-SAS model and governing equations

The classical Navier-Stokes equations are solved for this incompressible flow, to describe the fluid behavior [CHU 10b]. The finite volume discretization method is used to approximate the N-S equations by a system of algebraic equations for the variables at some set of discrete locations in space.

To catch the detail of vortices in the fluid field in acceptable calculation time, the SST-based Scale-adaptive Simulation (SAS) model is used [MEN 10]. The SAS approach represents a new class of the URANS models. Different from the conventional RANS formulations, the SAS model adjusts the turbulence length scale to the local flow inhomogeneities [LIU 17b]. As a measure of the local flow length scale, a classic boundary layer length scale introduced by von Karman is generalised for arbitrary three-dimensional

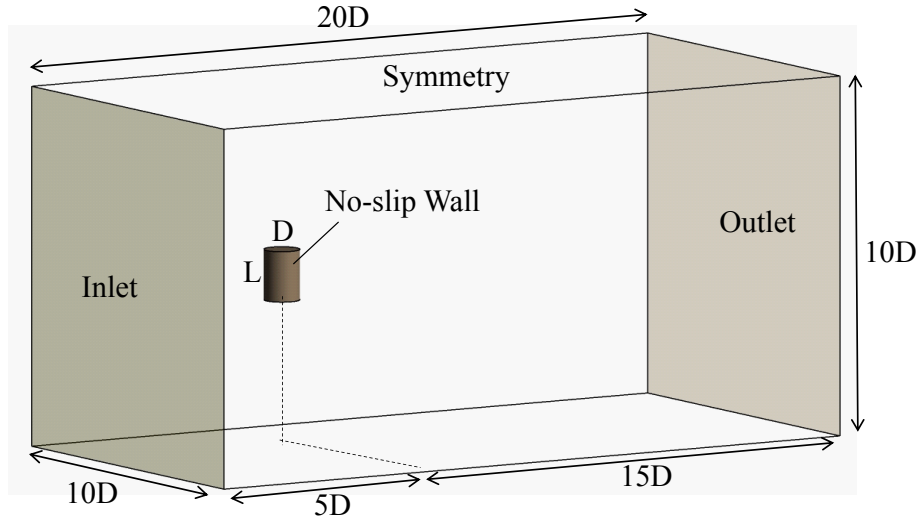


Figure 2.1: Geometry and boundary condition of the calculation domain

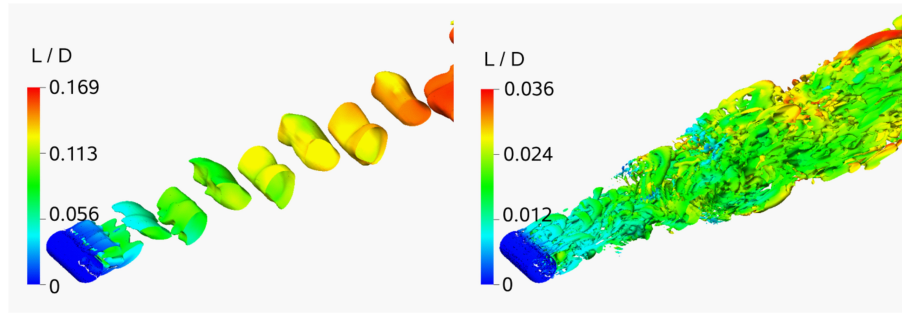


Figure 2.2: Cylinder in cross flow at Reynolds number of 3×10^6 : left - URANS, right - SAS, L - length scale of turbulence, D - cylinder diameter

flows [ZAC 16]. The von Karman length scale explicitly enters the transport equations of the turbulence model. The resulting model remains a RANS model, as it delivers proper RANS solutions for stationary flows and maintains these solutions through grid refinement. On the other hand, for flows with transient instabilities like those in the massive separation zones, the model reduces its eddy viscosity according to the locally resolved vortex size represented by the von Karman length scale. The SAS model can under those conditions resolve the turbulent spectrum down to the grid limit and avoids RANS-typical single-mode vortex structure as shown in Figure 2.2.

The governing equations of the SST SAS model are followed,

$$\frac{\partial \rho k}{\partial t} + \nabla \cdot (\rho U k) = P_k - \rho c_\mu k \omega + \nabla \cdot \left[\left(\mu + \frac{\mu_t}{\sigma_k} \right) \nabla k \right] \quad (2.1)$$

$$\frac{\partial \rho \omega}{\partial t} + \nabla \cdot (\rho U \omega) = \alpha \frac{\omega}{k} P_k - \rho \beta \omega^2 + Q_{SAS} + \nabla \cdot \left[\left(\mu + \frac{\mu_t}{\sigma_\omega} \right) \nabla \omega \right] + (1 - F_1) \frac{2\rho}{\sigma_{\omega 2}} \frac{1}{\omega} \nabla k \nabla \omega \quad (2.2)$$

The equations of the SST-SAS model equations differ from those of the RANS model by the additional SAS source term Q_{SAS} in the transport equation for the turbulence eddy frequency, ω . The additional source term Q_{SAS} reads

$$Q_{SAS} = \max \left[\rho \zeta_2 k S^2 \left(\frac{L}{L_{vk}} \right)^2 - C \cdot \frac{2\rho k}{\sigma_\Phi} \max \left(\frac{|\nabla \omega|^2}{\omega^2}, \frac{|\nabla k|^2}{k^2} \right), 0 \right] \quad (2.3)$$

In homogeneous turbulence, the SAS source term Q_{SAS} is zero and the model parameters in the SAS source term are:

$$\zeta_2 = 3.51, \sigma_\Phi = 2/3, C = 2 \quad (2.4)$$

The value L in the SAS source term is the length scale of the modelled turbulence, and the Von Karman length scale L_{vk} is a three-dimensional generalization of the classic boundary layer, which imposes the limiter to prevent the SAS equilibrium eddy viscosity from decreasing below the LES subgrid-scale eddy viscosity.

$$L = \sqrt{k} / \left(c_\mu^{1/4} \cdot \omega \right) \quad (2.5)$$

$$L_{vk} = k \left| \frac{U'}{U''} \right| \quad (2.6)$$

$$\mu_t^{eq} \geq \mu_t^{LES} \quad (2.7)$$

The first velocity derivative $\frac{\partial U}{\partial y}$ is represented in L_{vk} by U' , which is equal to S , a scalar invariant of the strain rate tensor $S_{,j}$:

$$U' = S = \sqrt{2 \cdot S_{,j} S_{,j}}; S_{,j} = \frac{1}{2} \left(\frac{\partial U_i}{\partial x_j} + \frac{\partial U_j}{\partial x_i} \right) \quad (2.8)$$

Note that the same S also directly participates in Q_{SAS} and in turbulence production term $P_k = \mu_t S^2$. The second velocity derivative U'' is generalized to 3D using the magnitude of the velocity Laplacian:

$$U'' = \sqrt{\frac{\partial^2 U_i \partial^2 U_i}{\partial x_k^2 \partial x_j^2}} \quad (2.9)$$

The model also provides a direct control of the high wave number damping. This is realized by a lower constraint on the L_{vk} value in the following way:

$$L_{vk} = \max \left(k \left| \frac{U'}{U''} \right|, C_S \sqrt{\frac{k \eta_2}{(\beta/c_\mu) - \alpha}} \cdot \Delta \right), \Delta = \Omega_{CV}^{1/3} \quad (2.10)$$

This limiter is proportional to the mesh cell size, which is calculated as the cubic root of the control volume size ω_{CV} . The purpose of this limiter is to control damping of the finest resolved turbulent fluctuations. The structure of the limiter is derived from analyzing the equilibrium eddy viscosity of the SST-SAS model.

The SST SAS model has been proven to be reliable enough for the unsteady flow with complex turbulence structure.

2.2.3 Fluid properties

In view of the running conditions in roller bearings, the oil used to lubricate the contacting surface is generally scattered by the movement of the solids. A mixture of air and oil is then supposed to exist around the rollers. In a steady running bearing, the fluid environment into the bearing cavity could also be regarded as steady. So that the rollers are assumed to be flooded in a uniform one-phase flow. Since the average oil volume fraction in high speed small bore roller bearing is usually less than 5%, the fluid property is set the same as air in normal pressure and temperature (1.225 kg/m^3 , $1.789 \times 10^{-5} \text{ kg/m-s}$).

2.2.4 Boundary conditions

As shown in the Figure 2.1, the inlet boundary condition consists of uniform velocity, turbulent intensity, and turbulence length respectively equal to 1% of one cylinder diameter. To compare the numerical results with previous experiment tests, the Reynolds number is respected to the value of $Re=8.8 \times 10^4$ at the beginning. The average pressure is maintained constant over the downstream surface, with four side surfaces as symmetry. The inlet velocity value is set to match a required Reynolds number.

$$V = \frac{Re * \mu}{\rho d} \quad (2.11)$$

2.2.5 Mesh dependence

The transient state equations are solved on inhomogeneous structured meshes for the flow domain with a strong clustering close to the walls. To capture the near-wall turbulent region with the turbulence model chosen here, the dimensionless wall distance y^+ is required to be less than 5 [WEH 15]. It is defined as $y^+ = \rho y u_r / \mu$, where y is the distance from the center of the first cell to the wall and u_r is the wall friction velocity. To match this requirement for all calculation cases, much finer cells are used around the cylinder, with a total cell number of approximately 1.25 million. It appears that using smaller cells does not significantly change the numerical solution.

2.2.6 Numerical methods

The commercial software ANSYS Fluent code is employed in this study to figure out the complicated flow problem [FLU 11][WIL 93] with the finite volume method to solve

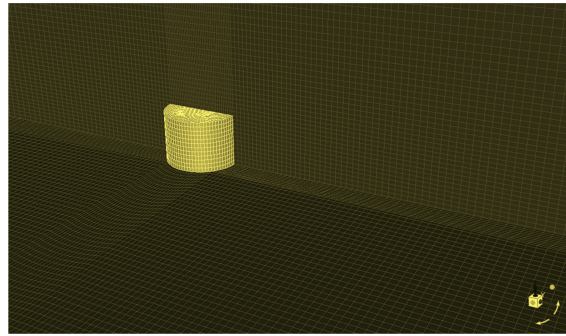


Figure 2.3: View of the mesh around the short cylinder

the governing equation. The second-order upwind difference is adopted for the momentum equation and turbulent kinetic energy. The pressure is adopted for the second order format. The semi-implicit method for pressure-linked equations-consistent (SIMPLEC) method is adopted for the coupling solution of pressure and velocity. The convergence is reached when both the normalized residuals of the equations fall below 10^{-5} and the three aerodynamic components behave periodically in accordance with structure detachments. Then a time-averaged estimation of all the data (streamlines, drag coefficient, etc.) is made using one single period. By changing different inlet velocity and fluid properties, the flow pattern with different Reynolds number is calculated. The effect of aspect ratio is explored with different geometry structures as well. The simulation results will be presented in detail.

2.3 Simulation results

2.3.1 Model validation

Before analysing flow behavior around the finite circular cylinder with two free ends, the numerical simulation method should be evaluated primarily, by comparing with available experimental and numerical results in the literature.

M.M.Zdravkovich [ZDR 89] built a test set to measure the drag force acting on short circular cylinders with two free ends. In the experimental arrangement, a circular cylinder with different length-diameter ratios is supported by two fixed vertical struts in the working section of the wind tunnel, which could provide continuous variation of velocity in the range of 15m/s to 35 m/s. The free stream longitudinal turbulence intensity in the empty working section was 0.3%. A six-component balance is situated immediately above the working section and is capable of measuring all three forces and three moments by using a set of load cells. The test section is shown in Figure2.4 and the drag force, pressure distribution are measured in the experimental investigation and are used to validate the CFD calculation results. Among them, the measured drag force was reduced to a drag coefficient by dividing drag by the free stream dynamic pressure and the area, taken to

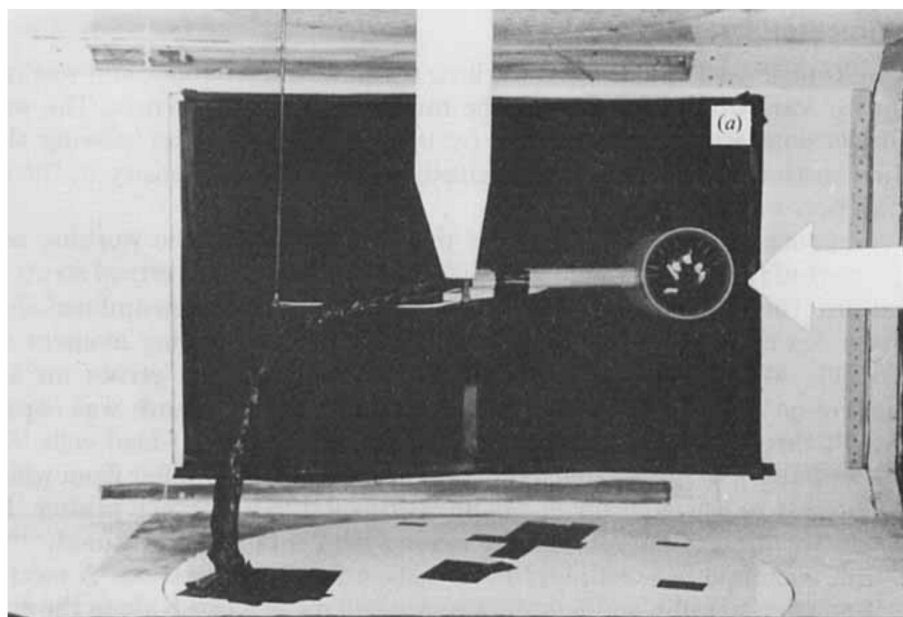


Figure 2.4: Experiment test section of circular cylinder in wind tunnel [ZDR 89]

be length times diameter of the cylinder. The free stream velocity was expressed by the Reynolds number based on the cylinder diameter.

In this regard, Figure 2.5 illustrates drag coefficient of cylinders for a various of aspect ratios and its comparison with other researchers' data at $Re=8.8 \times 10^4$. Also, Figure 2.6 compares the pressure distribution around the cylinder for the aspect ratio $L/D=1.5$ at $Re=2.55 \times 10^5$. As it can be seen, the simulation results are perfectly matched with the experimental results, demonstrating that the numerical method is sufficient to resolve flow structure around one finite circular cylinder with two free ends.

In Figure 2.5, it could be found that, for short cylinders, $1 < L/D < 6$, there is a very small change rate of drag coefficient and the trend appears almost as a horizontal line. It could be explained that the inflow is restricted by the sharp edge of the free ends for relative short cylinder [SUM 04]. The shape of the free end becomes a governing factor. To highlight the influence of the separated flow from two free ends to the wake behavior behind the cylinder, the aspect ratio in the present study is fixed to 1.5.

2.3.2 Flow pattern around the cylinder

Figure 2.7 shows the simulated streamlines around the cylinder when the flow reaches the steady state for the case of $Re = 45$. Major complexity of the flow structure occurs at the free ends of the cylinder because of the flow interaction with cylinder leading edge. Formation of these vortices inclines upstream flow slightly over the free end, named up-wash. As the flow passes over the cylinder tip, it is brought down into low pressure central wake region, called down-wash. With the attraction of the low pressure region behind the cylinder, the downwash flow turns back to the cylinder, forming the unsteady

2. Flow structure around one circular cylinder with two free ends

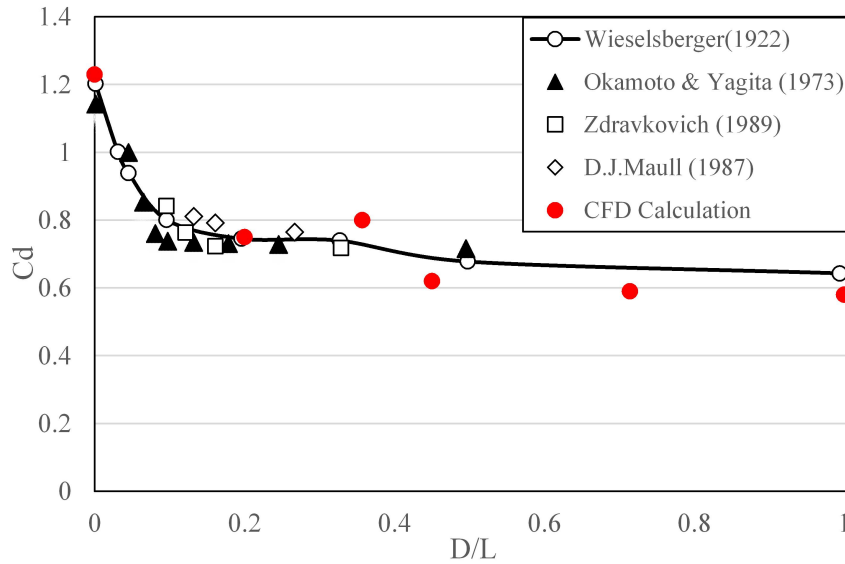


Figure 2.5: Comparison between the simulation and experiment results with different aspect ratio

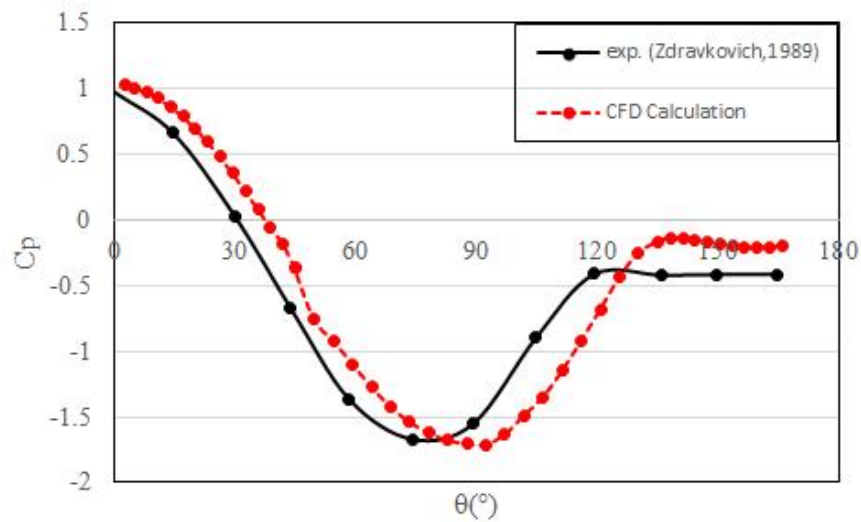


Figure 2.6: Pressure distribution around the circular cylinder with aspect ratio $L/D=1.5$

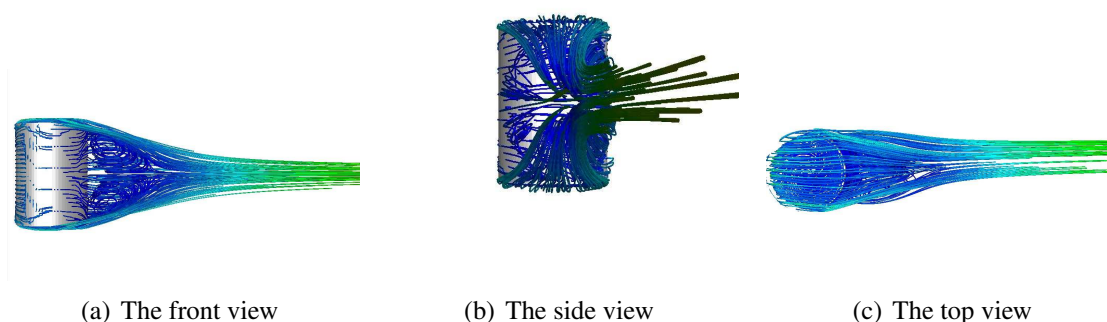


Figure 2.7: Flow patterns around the circular cylinder at $Re=45$

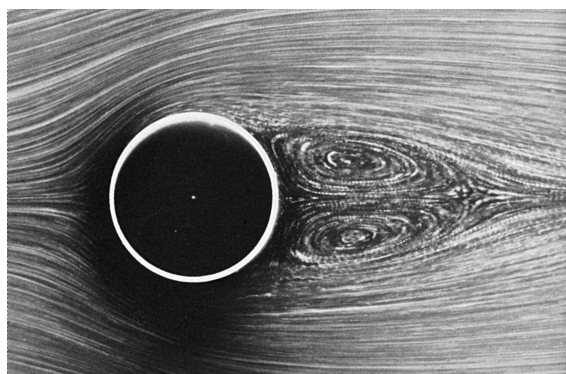


Figure 2.8: Steady-state wake behind the infinite cylinder at $Re = 40$ [SIN 10]

recirculation flow [ZHU 17]. It can be seen clearly that there are a pair of stationary recirculation eddies behind the cylinder. The same phenomenon was found in the two-dimensional model, as shown in Figure 2.8. The difference is that here the eddy appears in the axis direction of the cylinder. With symmetrical structure, the two recirculation flows developed from two free ends are symmetrical about the cylinder mid-span.

For a higher Reynolds number, $Re=450$, its near wake structures are visualized with streamlines from different directions in Figure 2.9. The flow begins to turn into unsteady, while the recirculating region remains behind the cylinder. In contrast, the recirculating region disappears at Reynolds numbers in excess of about 100 for the two-dimensional cylinder [SOH 15]. Besides, it could be found that the length of the recirculating region, which is from the nearest point of the cylinder to the end of the eddy, increases with the Reynolds number.

Another important phenomena occurs between the downwash flow from the free ends and the wake separated from the cylindrical surface. Shear flow from two free ends converges with the wake shedding from two sides of the straight cylinder, rolling up into four trilling spiral vortices in the flow direction, which is totally different with the Karman-type vortex in two-dimensional infinite cylinder model or the horseshoe vortex in the mounted

2. Flow structure around one circular cylinder with two free ends

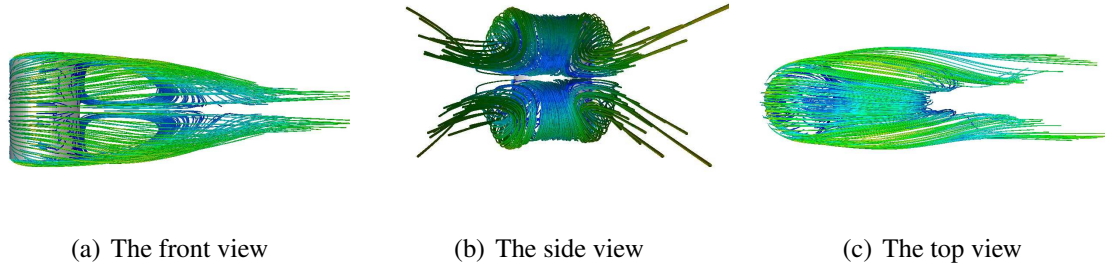


Figure 2.9: Flow patterns around the circular cylinder at $Re=450$

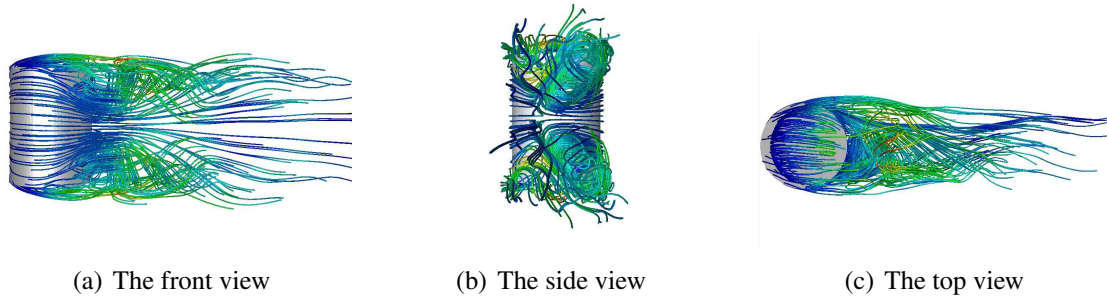


Figure 2.10: Flow patterns around the circular cylinder at $Re=4.5 \times 10^4$

finite circular cylinder with one free end. Every two adjacent vortex are counter-rotating.

If we continue to increase the Reynolds number, to the value of $Re=4.5 \times 10^4$, the flow becomes unsteady further as shown in Figure 2.10. The inflow of the downwash stream is pushed to further downstream by the two-dimensional wake from the straight cylinder. Four spiral vortexes are still symmetrical about the mid-span of the cylinder. But the centers of the vortexes swing in the circumferential direction regularly, showing a Karman-vortex-street-like behavior in the radial direction. The pressure distribution around the cylinder along the axis direction is monitored in Figs. 2.11 and 2.12. It corresponds with the flow pattern around the cylinder. Caused by the leakage from the free ends, pressure around two tips of the cylinder on the backside is obviously higher than that of the central part.

2.3.3 Flow structure on the free end

As previously mentioned, the flow structure at the free end is complex as a result of the sharp leading edge. In order to investigate the flow on the free end surface, a detail stream line pattern is shown in Figs. 2.13 and 2.15. The up-wash flow separates the end surface at the leading edge, producing a low pressure zone in the fore portion of the end surface, which attracts a wall-attached backflow from the rear portion. A crestline is formed at the intersection position of these two flows. This phenomenon is similar with that on the free

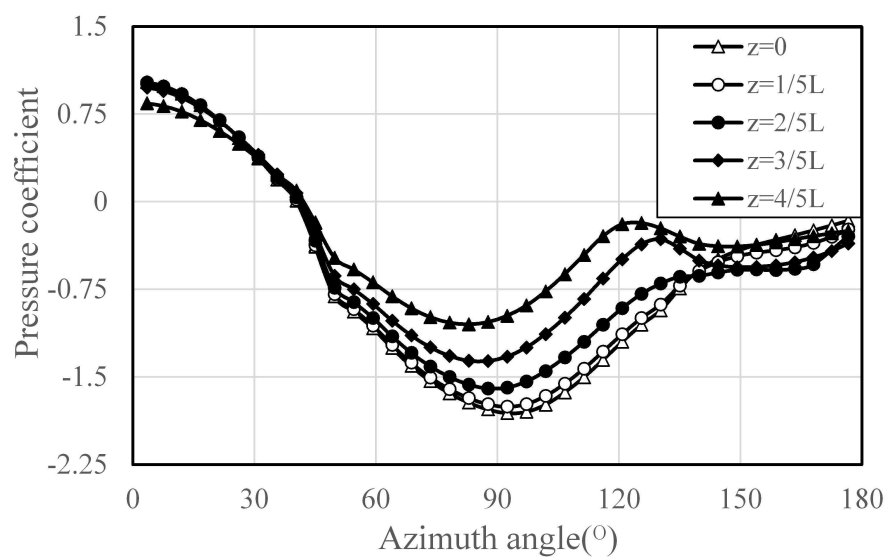


Figure 2.11: Pressure distribution around the circular cylinder in different axis position

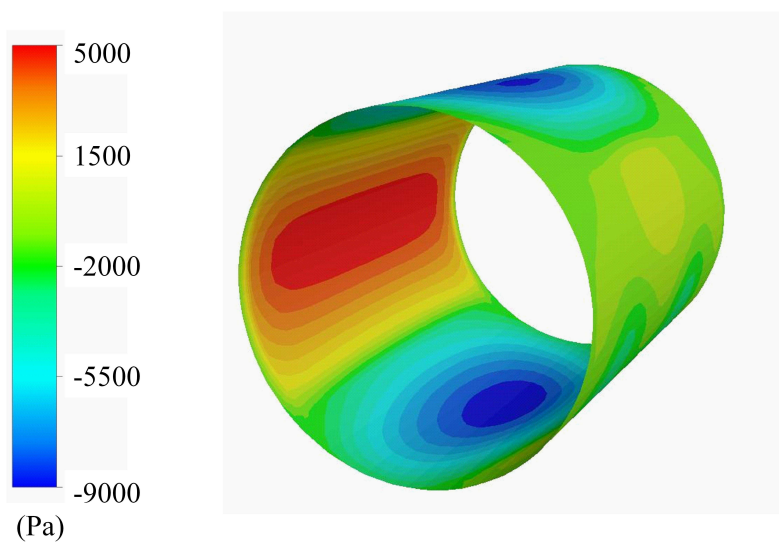


Figure 2.12: Pressure distribution around the cylindrical surface

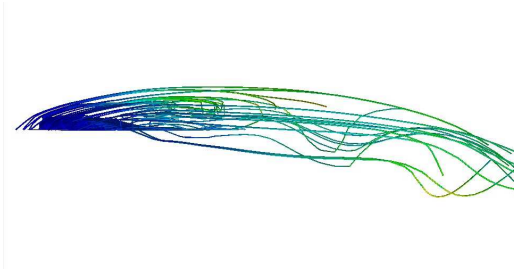


Figure 2.13: Side view of stream line on the free end



Figure 2.14: Flow pattern from the laser light visualization on the free end surface [ROH 03]

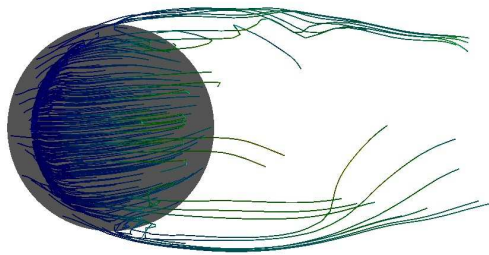


Figure 2.15: Top view of stream line on the free end

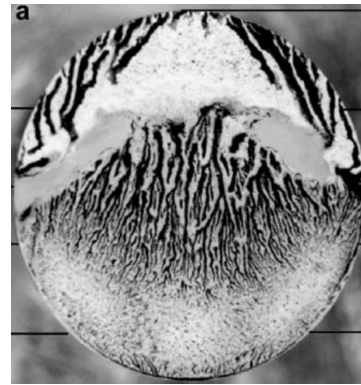


Figure 2.16: Oil streak lines on the free end surface [ROH 03]

end of one finite mounted circular cylinder, as shown in Figs. 2.14 and 2.16 [ROH 03].

Figure 2.17 shows turbulence kinetic energy distribution on the free end with different aspect ratios. With a higher aspect ratio, the strong vortex region moves from the rear portion to the fore part with the intensity weakened. It means that the shear flow separating from the circumferential leading edge of the free end is harder to turn to the recirculating region behind the cylinder with a higher aspect ratio. It could be explained that with a higher aspect ratio, the wake separating from the cylindrical surface pushes the down-wash to a further position away from the cylinder.

2.3.4 Drag coefficient on the cylinder

When the fluid flows past the cylinder, a shear stress is produced by the gradients of velocity at the surface of the cylinder with the no-slip condition. The shear stress sums to one part of the total drag force, called the viscous drag. Besides, the pressure of the fluid

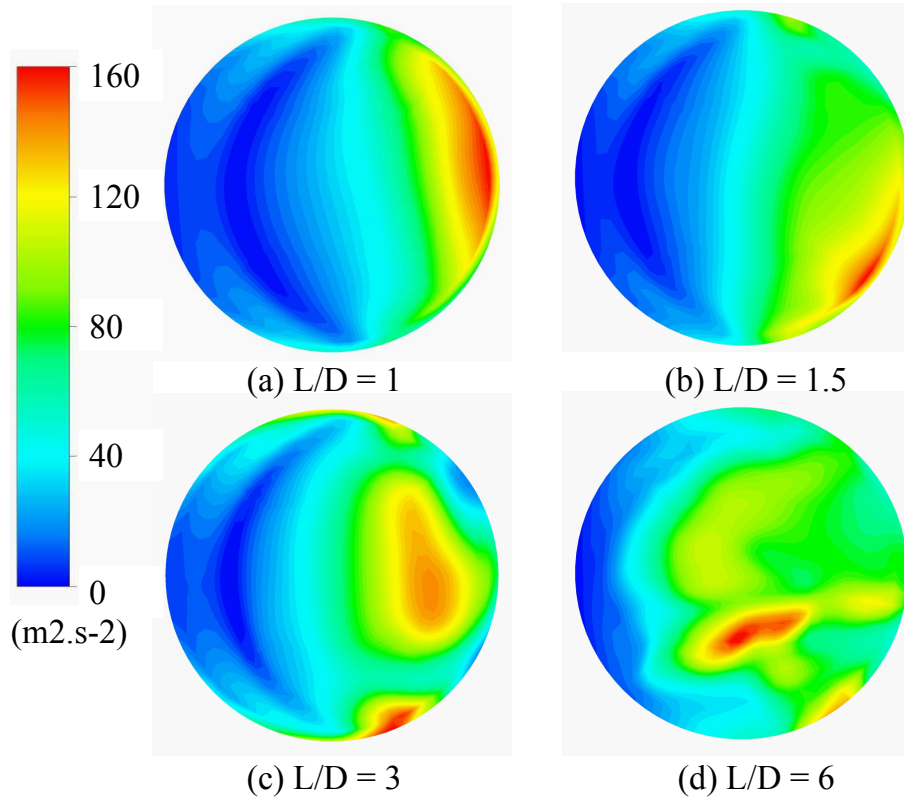


Figure 2.17: Turbulence kinetic energy distribuion on the free end with different aspect ratios ($Re = 4.5 \times 10^4$)

is greater on the unwind side of the cylinder than on the backside, which introduces the other part, called the pressure drag or form drag. A dimensionless expression of the total drag force is the drag coefficient defined by

$$C_d = \frac{F_d}{\frac{1}{2}\rho V^2 A} \quad (2.12)$$

Where ρ is the fluid density and A is the frontal area expressed by the body to the flow direction.

2.3.4.1 Effection of the aspect ratio to drag coefficient

Figure 2.5 illustrates the drag coefficient of the cylinder varying with its aspect ratio. Since the inflow or back flow could increase pressure distribution over the backside of the cylinder (see Figure 2.19), the pressure drag is reduced obviously so that the drag coefficient is lower than that of the infinite cylinder. Additionally, it could be observed that the reduction of the aspect ratio L/D continually decreases the drag coefficient. Figure 2.18 explains this phenomenon with vorticity magnitude around the cylinder with different aspect ratios. For the shorter cylinder, the three-dimensional separating flow around the

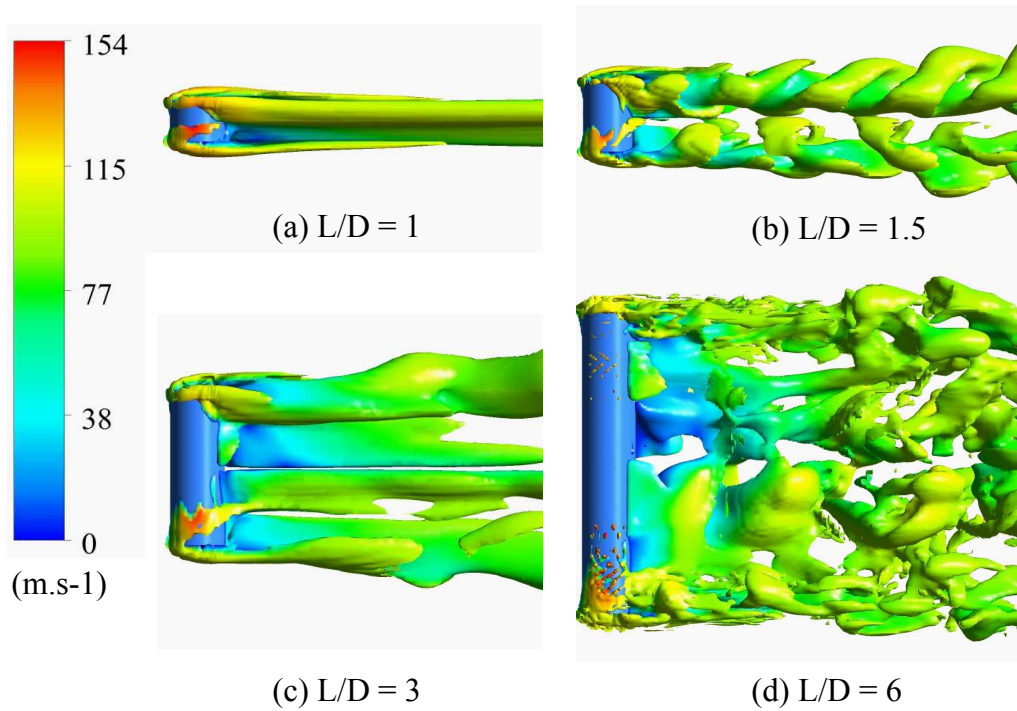


Figure 2.18: Vorticity magnitude around the circular cylinder with different aspect ratios

free ends develops to almost all the straight part of the cylinder while for the longer one, its effect only focuses on its two tips [TUM 17]. With the increasing of aspect ratio, the wake flow shedding from the straight cylinder becomes dominant in the flow region and its behavior becomes closing to the two-dimensional infinite model as shown in Figure 2.19.

Noting that, the aspect ratio of the cylinder could be reduced down to zero when, presumably, the drag coefficient won't be zero, as a result of the viscous drag on the free ends.

2.3.4.2 Effect of the Reynolds number to drag coefficient

In the previous section, it has been demonstrated that the flow structure around the cylinder with two free ends changes with the Reynolds number. The variation of drag coefficient with Reynolds number is crucial for fluid dynamic application. Up to now, typical drag coefficient of basic shapes in cross-flow has been measured except the finite circular cylinder with two free ends [TSU 11]. Based on the numerical simulation results with different fluid properties or boundary conditions, a line for drag coefficient as a function of Reynolds number suitable for short circular cylinder ($L/D=1.5$) with two free ends is obtained in Figure 2.20 in the range $4.6 < Re < 10^6$. Different from the two-dimensional model, in this range, there is no critical regime where exists a quick drop of drag coefficient due to the transition from laminar to turbulent separation of the boundary layer. As mentioned previously, the aspect ratio changes drag coefficient slightly with the aspect

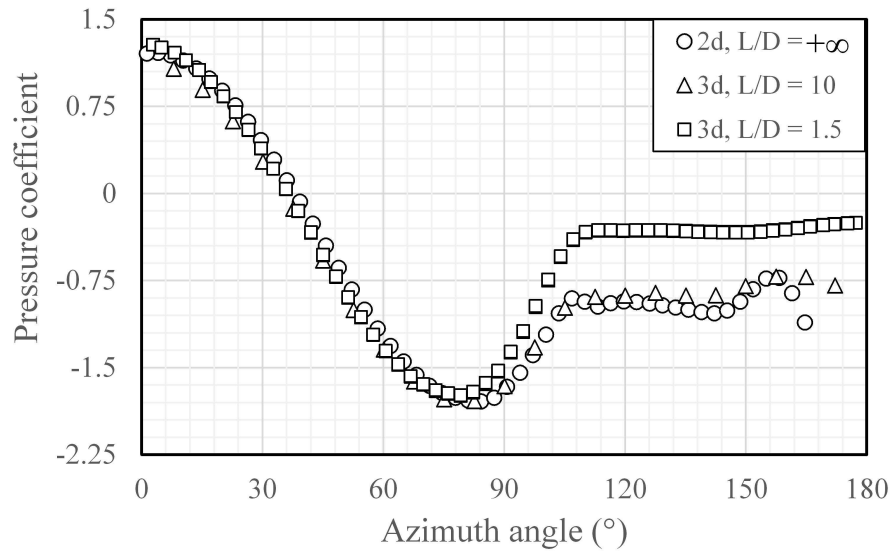


Figure 2.19: Pressure distribution around the circular cylinder with different aspect ratios

ratio $1 < L/D < 6$, so that this line could be employed considerably to all short circular cylinder with two free ends in this range.

2.4 Conclusions

Flow characteristics around one circular cylinder with two free ends is investigated in this chapter, with a validated numerical method. With different Reynolds numbers and aspect ratios, the effect of two free ends to the cylinder's flow structure, pressure distribution and drag coefficient is analyzed. The results show that

(1) The flow structure around one finite circular cylinder with two free ends is totally different from that of the infinite cylinder or the finite circular cylinder with one free end.

(2) With the decreasing aspect ratio, three-dimensional separating flow from the end surface develops to almost all the cylinder and the wake flow shading from the straight cylinder is extruded and reshaped. With a bigger aspect ratio, the down-wash flow is restricted by the wake from the cylindrical surface.

(3) A pair of recirculating eddies appears behind the cylinder in the axis direction at low Reynolds number. With the increasing of Reynolds number, the flow turns unsteady and four spiral vortices are formed in the stream direction by the interaction of the two separated flows from two free ends and the wake flow.

(4) Compared with the two-dimensional cylinder model, the inflow passing from two free ends increases pressure distribution over the backside of the cylinder and thus decreases its drag force. A new relationship of drag coefficient corresponding with Reynolds numbers is proposed, especially for short circular cylinder with two free ends with the aspect ratio $1 < L/D < 6$.

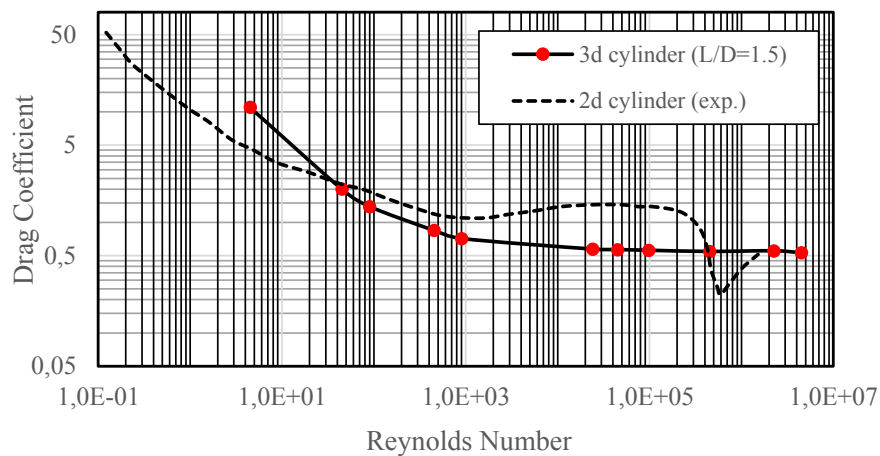


Figure 2.20: Drag coefficient of one circular cylinder with two free ends as a function of Reynolds number

Chapter 3

Drag coefficient and churning moment in roller bearings

In this chapter the drag coefficient and churning moment on the cylinder element in roller bearings are investigated numerically based on the one-phase-environment assumption.

Contents

3.1	Introduction	51
3.2	Drag coefficient in roller bearings	51
3.2.1	The CFD model introduction	52
3.2.2	Flow around the isolated rotating cylinder	53
3.2.3	Drag coefficient of the isolated rotating cylinder	54
3.2.4	Flow around several in-line rotating cylinders	58
3.2.5	Drag coefficient of several in-line rotating cylinders	58
3.3	Churning moments in roller bearings	59
3.3.1	Churning moments on the isolated rotating cylinder	62
3.3.2	Churning moments on several rotating cylinders	71
3.4	Conclusion	79

3.1 Introduction

As mentioned previously, the roller element in bearings is a special finite-length circular cylinder with two free ends. In the last chapter, a numerical simulation method is proposed and the flow around one finite circular cylinder with two free ends is analyzed in detail. It should be noted that this model is too simplified and could only serve as a basis for further investigation. In a real roller bearing, except being driven or braked by the cage, all roller elements are sandwiched by two rings with micron-size clearance. It means that the oil-air mixture in bearing cavity could only flow bypass the roller's free ends rather than flowing past its cylindrical surface. Besides, each roller element is adjacent with another two rollers in up-stream and down-stream respectively. Flow around these endless in-line cylinders with small gap could interact with each other. In conclusion, for the windage drag force and churning moment investigation, a three-dimensional model with all influence factors is essential.

Except that, for churning losses in roller bearings, there are few approaches used directly for its estimation, which could only provide a rather gross approximation. It should be emphasized that in the model mentioned in Chapter 1, the fluid is initially assumed at rest and there is no relative translational motion between the roller and the fluid, which is entirely different with the actual situation in a bearing. So that it's necessary to develop a new formula for churning losses prediction in roller bearings based on the numerical investigation.

In this chapter, with the CFD simulation method verified in the last chapter, the configuration with one single circular cylinder in open space is studied further. The circular cylinder is set to rotate by its own axis, like the roller in bearings. Drag force and churning moments acting on the cylinder surface are monitored in the calculation. After that, the geometry structure is changed to close to the real bearing configuration, with several in-line rotating cylinder elements sandwiched by two flat walls. Interference between different elements and all surroundings is presented. A new relationship of drag coefficient varying with Reynolds number suitable for cylindrical elements in roller bearings is obtained. In the numerical investigation, different parameters, e.g. roller rotating speed, roller orbital speed, fluid properties, and roller geometry parameters, are studied to quantify their effects. Finally, a numerical-based formula is proposed suitable for churning losses prediction in roller bearings. To our knowledge, this is the first time that the drag force and churning moment in roller bearings are analyzed with the CFD method separately.

3.2 Drag coefficient in roller bearings

As mentioned in Chapter 1, in high speed roller bearings, drag force acting on roller elements by the oil-air mixture in bearing cavity is frequently obtained from a two-dimensional model of flow past one infinite-length cylinder. Whereas in roller bearings, all cylinder elements are sandwiched by inner and outer rings with micron-size clearance

so that the flow could only bypass the sharp-edge circular ends, rather than the cylindrical surface. In addition, every cylinder is accompanied with another two cylinders in front and rear, which may strongly interact with each other. Consequently, drag coefficient for cylindrical elements in roller bearings has to be investigated with a three-dimensional model and take the surroundings into account.

In this part, a numerical CFD modelling method is presented to study the flow around circular cylinders with two free ends in roller bearings, to clarify drag force acting on its surface. First, the numerical model with one isolated circular cylinder in open space, which has been investigated and verified in Chapter 2, is used and studied further, to validate the effect of the cylinder's rotating and the changing rule of its drag coefficient. Then the model is changed to close to real bearing configuration, with several in-line circular cylinders sandwiched by two flat walls. Finally a relationship between drag coefficient and Reynolds number suitable for circular cylinder in roller bearings is summarized. More than that, the geometry of this research is a simple three-dimensional bluff body so that the flow is of fundamental importance and its result could be applied to more complicated situation.

3.2.1 The CFD model introduction

Based on the fact mentioned above, the numerical investigation is splitted into two steps with for each of them two different configurations. Firstly, one isolated rotating circular cylinder in an open space (Configuration 1) is studied, within a uniform stream. The calculation configuration and the boundary conditions are shown in Fig. 3.1, which is the same as that in Chapter 2.

After that, the configuration (Configuration 2) with three in-line rotating cylinders, sandwiched by two flat walls with periodic boundary conditions, is investigated, to reveal flow characteristics in roller bearings. That represents a simplified arrangement of cylindrical roller bearings (see Fig. 3.2). Two flat walls replace the inner and outer rings and three in-line cylinders replace the endless rollers orbiting in the bearing cavity, with the periodicity boundary condition. The curvature of the rings is ignored, without regard to the cage either. In order to avoid low mesh quality, the radial clearance between rollers and rings is assumed here two times bigger than that in a real bearing. The fluid domain is meshed with a structured hexahedron grid with the commercial software ANSYS ICEM, with about 2.9 million cells.

For the solution methods, the SST SAS model is used to catch the details of the vortices in the fluid field within an acceptable calculation time. The second-order upwind difference is adopted for the momentum equation and turbulent kinetic energy. The semi-implicit method for pressure-linked equations consistent (SIMPLEC) method is adopted for the coupling solution of pressure and velocity. In Configuration 1, the inlet velocity is equal to the roller orbital speed along with the cage, and the cylinder rotational speed is set as the roller rotating speed by its own axis. While in Configuration 2, the roller orbital speed is taken place by the fluid volume flow rate of the periodic boundaries.

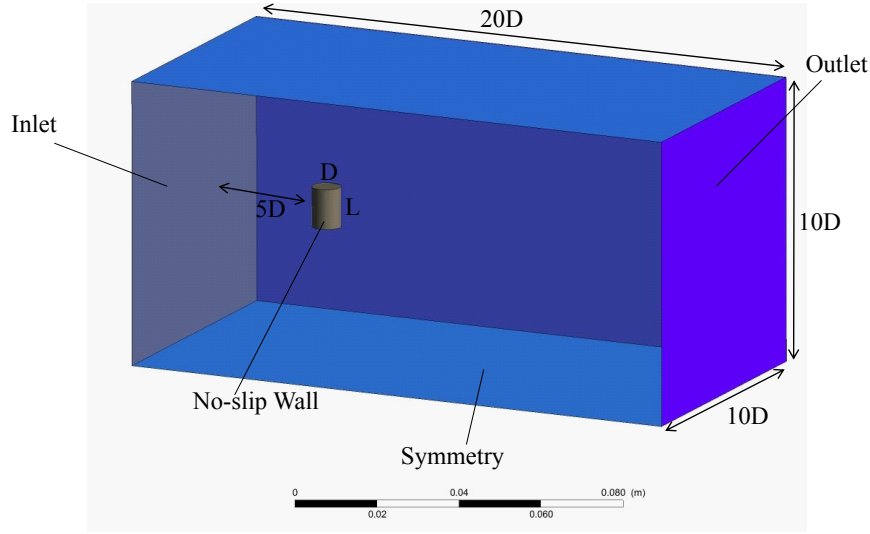


Figure 3.1: Geometry and boundary condition of the configuration with one isolated cylinder (Configuration 1)

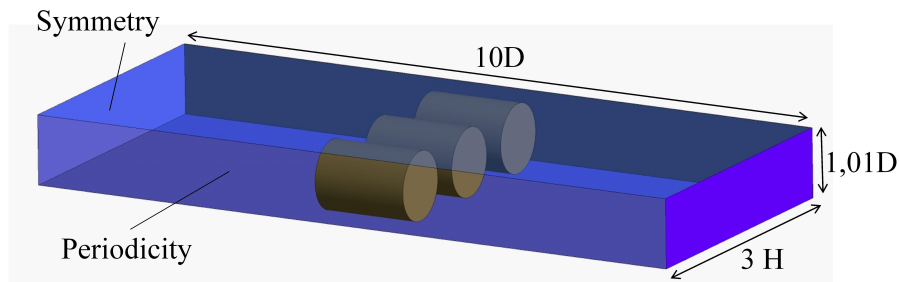


Figure 3.2: Geometry and boundary condition of the configuration with several in-line cylinders (Configuration 2)

3.2.2 Flow around the isolated rotating cylinder

In Chapter 2, flow around one isolated circular cylinder with two free ends is studied. Unlike that model, in roller bearings, each roller element rotates by its own axis. This rotation may change the flow around the cylinder. For a nominal shaft rotational speed at 30,000 rpm, the roller rotating speed by its own axis could catch up to 100,000 rpm and the maximum linear velocity of the roller surface could be over 30 m/s. So that the influence of the roller's rotating to the flow pattern around the isolated cylinder should be put forward.

Fig. 3.4 illustrates flow pattern around the rotating cylinder with a rotating speed of 10,000 rpm and flow speed of 92 m/s. In this case, the maximum linear velocity of the roller surface is about 3.7 m/s, which is 1/30 of the flow speed. It could be found that the flow pattern around the rotating cylinder is similar to that of the cylinder without rotating, which means that the effect of the roller rotating could be ignored.

While if we continue to increase the roller rotational speed, up to the value of 100,000 rpm. The maximum linear velocity of the cylinder surface is about 37 m/s, more than 1/3 of the flow speed. By comparing velocity pattern with different rotating speed in Fig. 3.3, it could be found that the separating position of the wake from the cylindrical surface is deflected along the rotating direction. The faster the cylinder rotates, the greater the deflection is.

But, as shown in Fig. 3.5, the simulated streamline around the cylinder shows that the roller's rotation has slight effect to its flow structure. The vortices around the cylinder with different rotating speed are similar. These facts indicate that for one finite circular cylinder with two free ends, the swirling vortices separating from free ends are the key element which determines the wake behavior of the finite-length cylinder, which has been proven in Chapter 2.

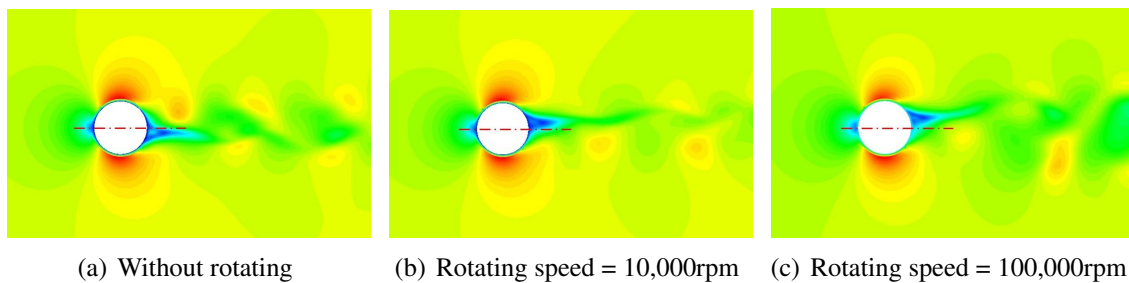


Figure 3.3: Velocity pattern around the isolated cylinder with different rotating speed

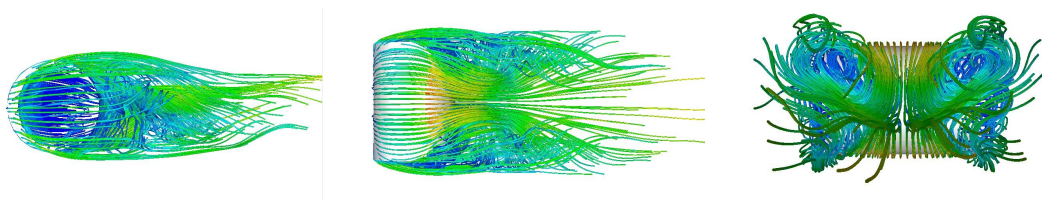


Figure 3.4: Flow pattern prediction for the isolated rotating cylinder (10,000 rpm)

3.2.3 Drag coefficient of the isolated rotating cylinder

For the influence of the cylinder's rotating to its drag coefficient, previous study demonstrates that there is no relationship between them. This conclusion is confirmed again by our numerical simulation results, as shown in Fig. 3.9.

In Chapter 2, the effect of aspect ratio to drag coefficient has been mentioned. For relative short cylinders, $1 < L/D < 6$, there is a very small change rate of drag coefficient versus the aspect ratio, which is a normal range in roller bearings. So that it could be

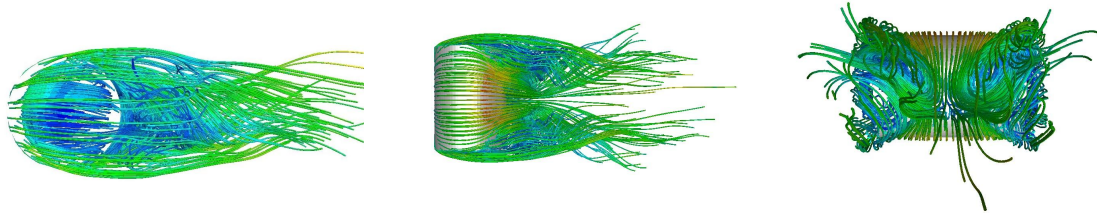


Figure 3.5: Flow pattern prediction for the isolated rotating cylinder (100,000 rpm)

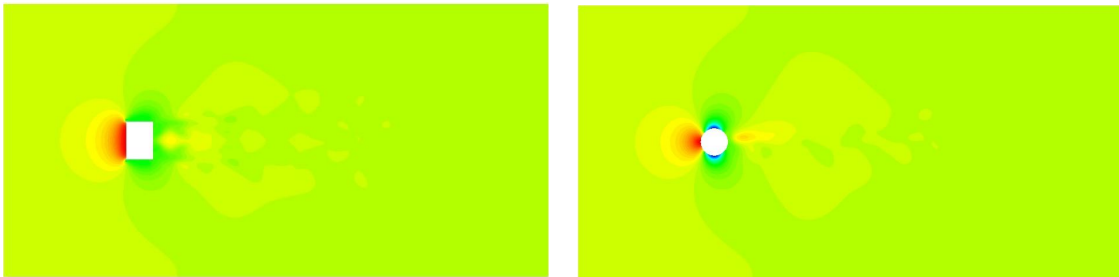


Figure 3.6: Pressure distribution around the isolated rotating cylinder (10,000 rpm)

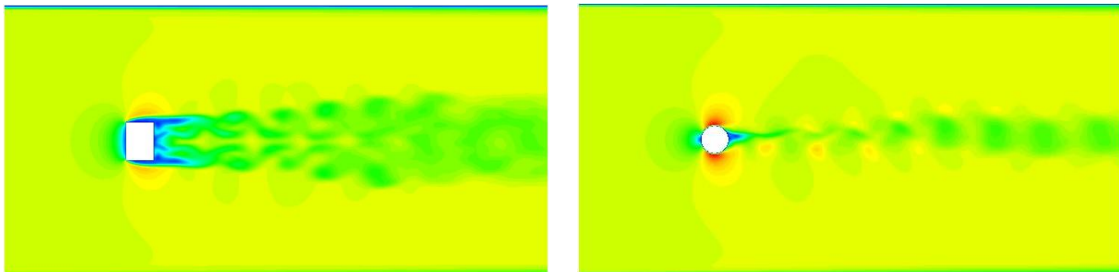


Figure 3.7: Velocity distribution around the isolated rotating cylinder (10,000 rpm)

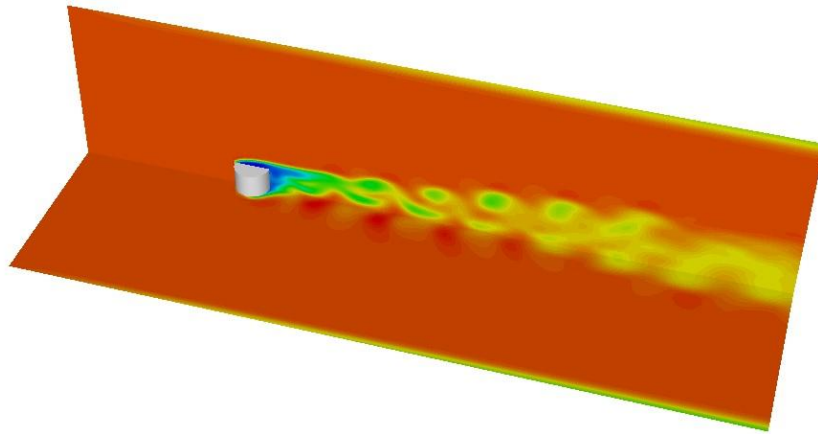


Figure 3.8: Total pressure distribution around the isolated rotating cylinder (10,000 rpm)

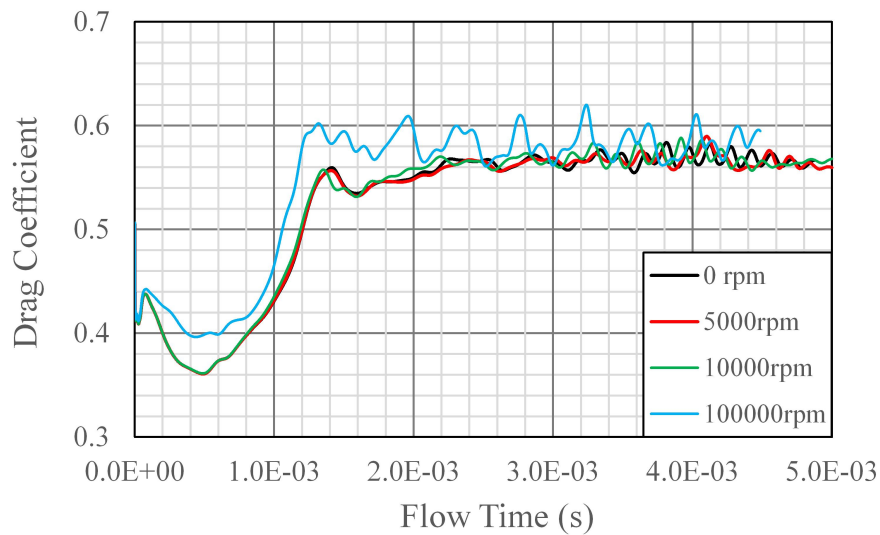


Figure 3.9: The influence of the cylinder's rotating speed to its drag coefficient

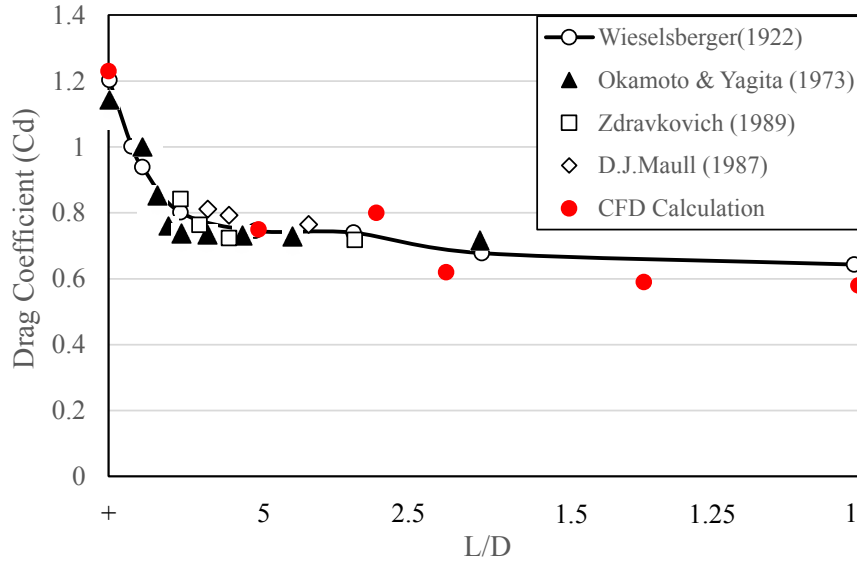


Figure 3.10: The influence of the cylinder's aspect ratio to its drag coefficient

assumed that in the application of roller bearings, the L/D of circular cylinder does not change its drag coefficient and the effect of aspect ratio could be ignored (see Fig. 3.10).

Except the aspect ratio, Reynolds number is another crucial factor changing drag coefficient of circular cylinder. Up to now, typical drag coefficient of basic shapes in cross-flow has been measured except the finite circular cylinder with two free ends. Based on numerical simulation, a relationship between drag coefficient and Reynolds number suitable for circular cylinder ($1 < L/D < 6$) in open space is obtained in the range $4.6 < Re < 10^6$, which is definitely different with the one for two-dimensional model (Fig.3.11). In the zone around $Re = 8.8 \times 10^4$, drag coefficient keeps stable to the value of 0.6, compared with the coefficient of 1.25 for two-dimensional circular cylinder model. Different from the 2d model, in this range, there is no critical regime with a quick drop of drag coefficient due to the transition from laminar to turbulent separation of the boundary layer.

A simple expression for the drag coefficient versus the Reynolds number suitable for drag force calculation of one finite circular cylinder with two free ends in an open space is obtained.

$$C_d = 37.5 \times Re^{-0.8515} + 0.5671 \quad (3.1)$$

As mentioned above, the aspect ratio changes drag coefficient slightly with the aspect ratio $1 < L/D < 6$, so that this line could be employed considerably to short circular cylinder with two free ends in this range.

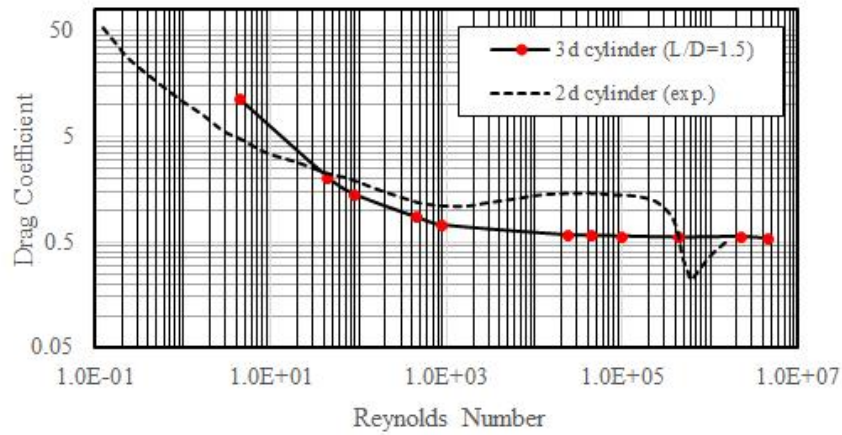


Figure 3.11: Drag coefficient of one isolated circular cylinder with two free ends

3.2.4 Flow around several in-line rotating cylinders

The flow pattern around several in-line circular cylinders is definitely different with the isolated cylinder. In view that all cylinder elements are sandwiched by inner and outer rings with micron-size clearance, the flow could only bypass the sharp-edge circular ends rather than the cylindrical surface. Besides, with relative short gap between two adjacent rollers, the wake cannot freely extend like the isolated cylinder, causing several local vortex in the gap between two cylinders (Fig. 3.12). Differential pressure is almost offset between the windward side and the leeward side of the cylinder.

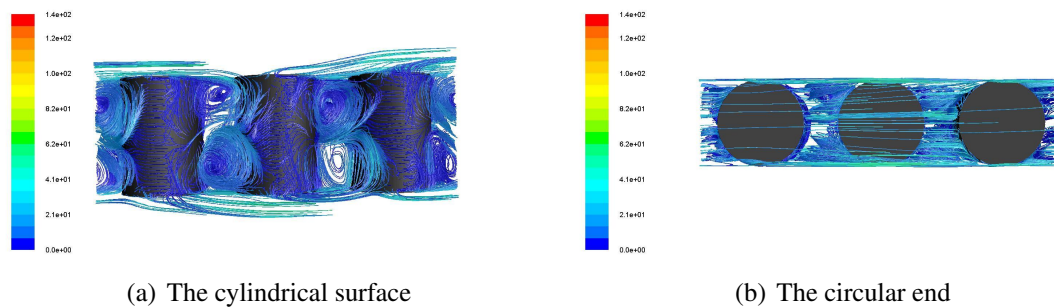


Figure 3.12: Flow pattern and velocity distribution of several in-line cylinders

3.2.5 Drag coefficient of several in-line rotating cylinders

In that viscous drag is mainly decided by the fluid property, the drag coefficient is thus highly reduced compared to the isolated cylinder. When the distance between every adjacent cylinder centers is $H = 1.4 \times D$, drag coefficient of several in-line cylinders is about $C_d = 0.025$ at $Re = 8.8 \times 10^4$. Corresponding with the change of H , pressure distribution

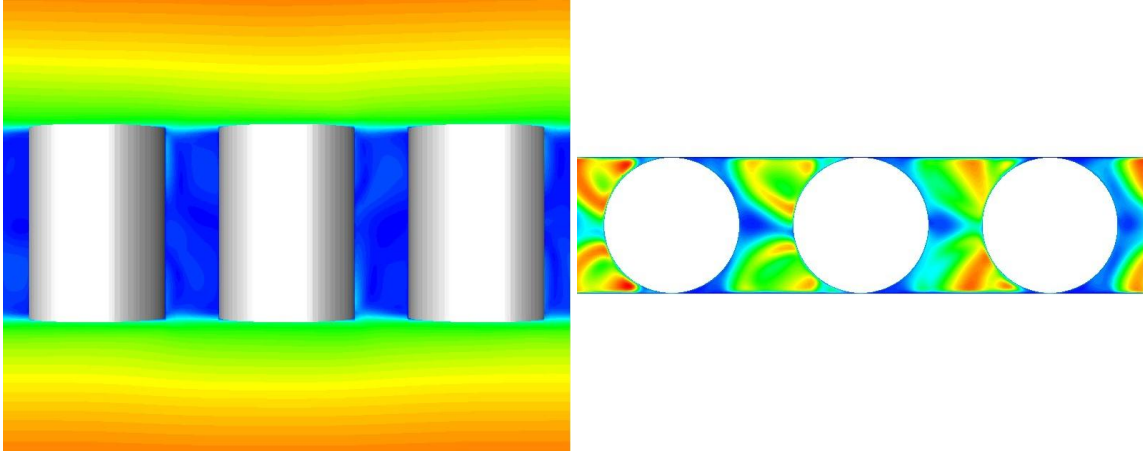


Figure 3.13: Contour of velocity distribution around the several in-line cylinders

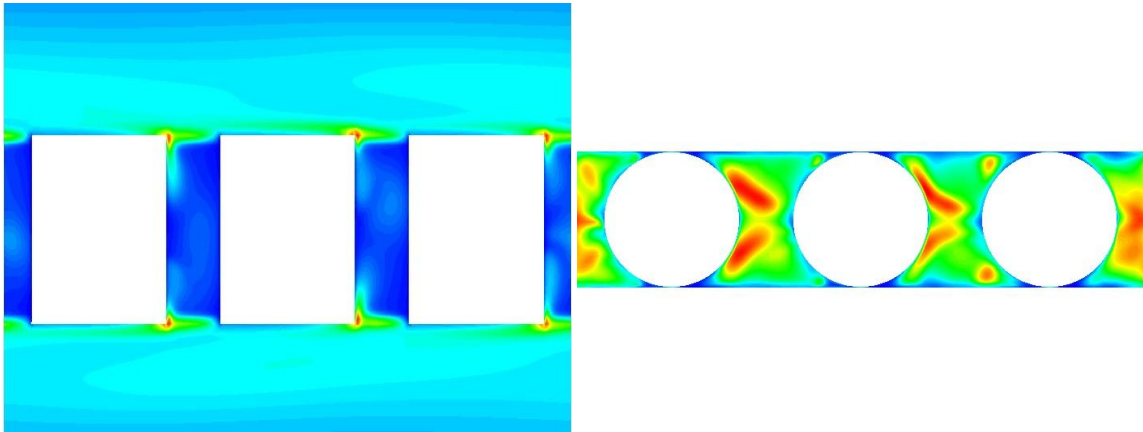


Figure 3.14: Contour of turbulent kinetic energy around the several in-line cylinders

around these circular cylinders changes in a small range (Fig.3.15) but here it's not mentioned particularly for the roller bearing application. The whole drag coefficient variation in the range $4.6 < Re < 10^6$ for several sandwiched in-line cylinder is demonstrated in Fig.3.16, which is more suitable for drag force calculation in roller bearings.

Finally, a simple expression for the drag coefficient versus the Reynolds number suitable for drag force calculation in roller bearings ($1 < L/D < 6$) is finally obtained.

$$C_d = 35.02 \times Re^{-0.9899} + 0.05975 \quad (3.2)$$

3.3 Churning moments in roller bearings

In rolling bearings, each rolling element orbits along the circle runway together with the cage, and rotates by its own axis at the same time. As the churning phenomenon

3. Drag coefficient and churning moment in roller bearings

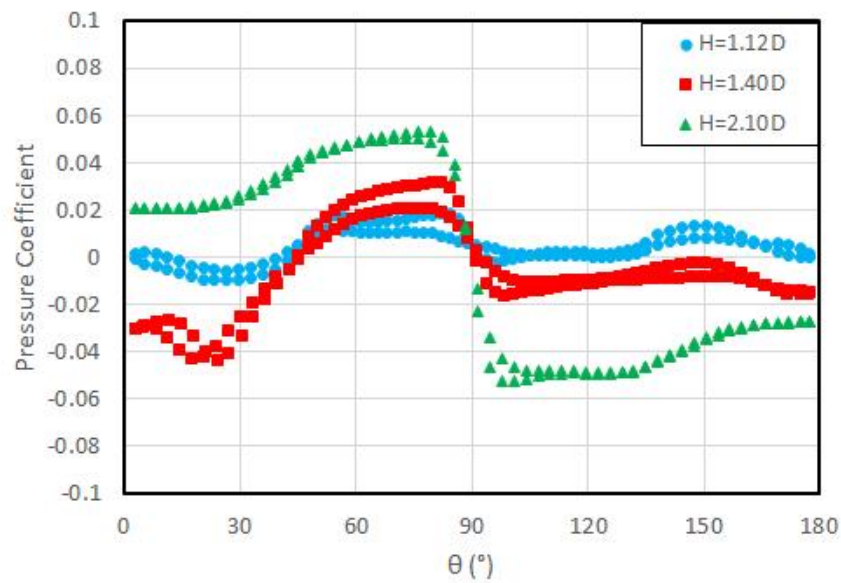


Figure 3.15: Pressure coefficient around the single circular cylinder

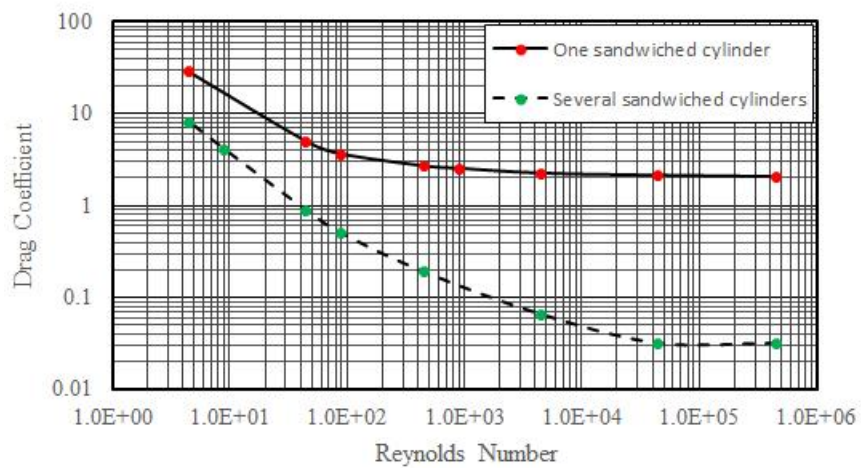


Figure 3.16: Drag coefficient of several sandwiched in-line cylinders

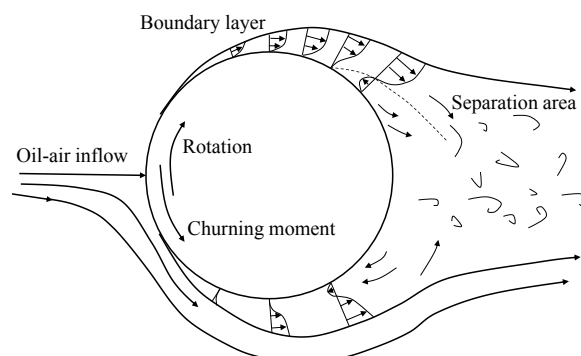


Figure 3.17: Churning effects diagram of the rotating roller in the fluid

in gearbox, the rotating roller elements churn the surrounding fluid, causing considerable churning losses, as shown in Fig. 3.17. The churning losses come from churning moments acting on the roller surface, which have attracted least attention so far. Both measurement and estimation of churning losses in (high-speed) rolling bearings are extremely difficult tasks.

Rumbarger and Filetti provided an estimate of churning moment on cylindrical surface of rollers [NIC 17]. Moreover the churning moment on the side of rollers is characterized by the flow over a rotating disk by von Karman [APP 15]. It should be noted that in the model mentioned above, the fluid is initially assumed at rest and there is no relative translational motion between the roller and the fluid, which is entirely different from the actual situation in a bearing. Besides, each roller is sandwiched by two rings with micro-size gap, and is adjacent with another two rollers in up-stream and downstream respectively. In previous models the interference from surrounding walls and rollers is ignored either, which has obvious effect to the flow around rollers [MAR 15]. Therefore, a deeper understanding to the physical responsible of churning losses in cylindrical roller bearings is needed to propose a more reliable and accurate estimation formula. In last decade, a series of numerical studies are reported on the fluid churning loss in transmission gears with reliable results [LAR 17, LIU 17a]. It demonstrates that the Computational Fluid Dynamics (CFD) method is effective for this type of problems.

In this section, the CFD simulation method used for the drag coefficient study is employed. The main object of this numerical investigation is to vary different operating parameters and analyze their influence on the churning moments for a finite cylinder moving and rotating in a uniform fluid, and propose a reliable physics-based churning losses prediction formula suitable for cylindrical roller bearings. To evaluate the effect of the roller orbiting motion, the first configuration is primarily tested and its results are compared with previous empirical and theoretical results. Then, the second configuration is investigated. The effect of a series of parameters are analyzed, including roller geometry parameters such as cylinder diameter and length, lubricant properties such as lubricant viscosity and density, and operating parameters such as cylinder rotational speed and orbital speed (the flow inlet speed). Finally, a churning moment prediction formula for roller element in bearings is proposed [GAO 18]. The numerical simulation results

will be presented in detail.

3.3.1 Churning moments on the isolated rotating cylinder

For churning moments on the isolated rotating cylinder, the formulas proposed by Rumbergar and Von Karman indicate that the oil properties, the roller geometry parameters, and the running condition all have a significant impact on the churning moments. But, the roller's orbiting motion with the cage is ignored. Besides, the fluid is initially assumed at rest and there is no relative translational motion between the roller and the fluid, which is entirely different from the actual situation in a bearing.

To quantify the influence of the roller's translational motion (roller orbiting) on its churning moment, the configuration with one isolated rotating circular cylinder in open space is studied, with a specific-velocity uniform stream. Its results are compared with previous empirical and theoretical work. The effect of a series of parameters are analyzed, including roller geometry parameters such as cylinder diameter and length, lubricant properties such as lubricant viscosity and density, and operating parameters such as cylinder rotating speed and orbital speed (the flow inlet speed). Finally, a churning moments prediction formula for the isolated rotating cylinder is summarized. The numerical simulation results will be presented in detail.

3.3.1.1 Comparison of different models

In Rumbergar and Von Karman's formulas, the effect of roller orbital speed or the cage speed is ignored. To illustrate its difference, two numerical simulations are carried with or without inlet speed (no translational motion), and their results are compared with the results of Rumbergar and Von Karman's formulas. In this regard, Fig. 3.18 demonstrates the difference of churning moments in these two conditions on the cylindrical surface and circular end respectively. Rumbergar and Von Karman's result is close to the case without translational motion, while churning moments on the rotating cylinder moving in the fluid are obviously larger.

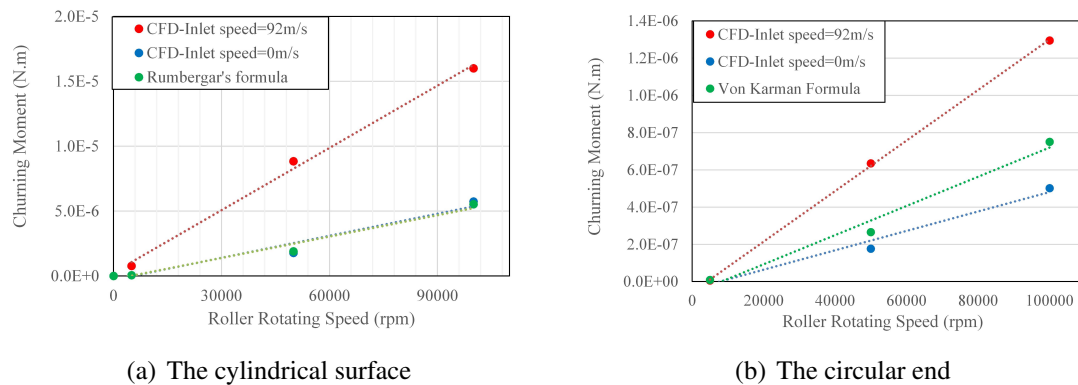


Figure 3.18: Comparison of churning moments between different calculation models

3.3.1.2 Parameters that effect the churning moment

Although the effect of roller orbital speed or the cage speed in rolling bearings is ignored by previous researchers, it is an important factor that should be accounted for carefully. This is represented by the stream flow speed in the numerical model. To quantify its influence, flow pattern around the rotating cylinder in stream flow is compared with that of a rotating cylinder in a steady fluid. Fig. 3.19 shows flow streamline around the cylinder in stream flow and in a steady fluid, respectively. Compared with pure rotating in a steady fluid, the effect of stream flow is dominant that is to say the three-dimensional separated shear flow around the end surface turns into the wake zone downstream near the cylindrical surface, which considerably influences the wake behavior around the cylinder. Besides, Fig. 3.18 demonstrates the difference of churning moments in these two conditions on the cylindrical surface and roller end, respectively. It illustrates that Rumbergar and von Karman's result is close to the case without orbiting motion, while churning moments on the rotating cylinder moving in the fluid are obviously larger.

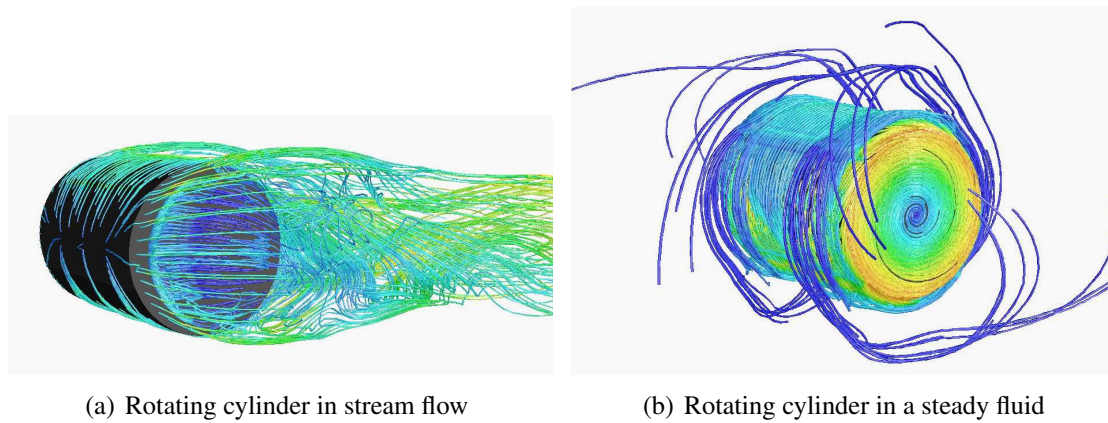


Figure 3.19: Influence of translational motion (roller orbiting) to the flow structure around the circular side (Configuration 1)

As shown in Fig. 3.20, churning moments on the cylindrical surface and the cylinder end are both linear with respect to the roller orbital speed. It should be noted that when the roller orbital speed is zero, the corresponding churning moment is not zero. Its value should be equal to the Rumberger and von Karman's formulas, which corresponds to the case without translational motion. In our study, this component of churning moment is called the static churning moment, while the other component caused by the roller orbital speed is called the dynamic churning moment. The churning moment on the cylindrical surface and the roller end is the sum of these two parts. So that the equations for churning moment on the isolated circular cylinder in open space could be written as following.

For the cylindrical surface,

$$M_c = M_{c0} + M_{c1} = M_{c0} + C_p^a \mu^b V^c \omega^d L^e r^f \quad (3.3)$$

For the roller end,

$$M_e = M_{e0} + M_{e1} = M_{e0} + C_e \rho^g \mu^h V^i \omega^j L^k r^l \quad (3.4)$$

Fig. 3.21 shows the relationship between churning moment on the isolated roller surface and its rotating speed on its own axis. Similar to the roller orbital speed, churning moment on the roller surface is proportional to its rotating speed, both for the cylindrical surface and the roller end. The difference is that the moment would be zero when the roller doesn't rotate.

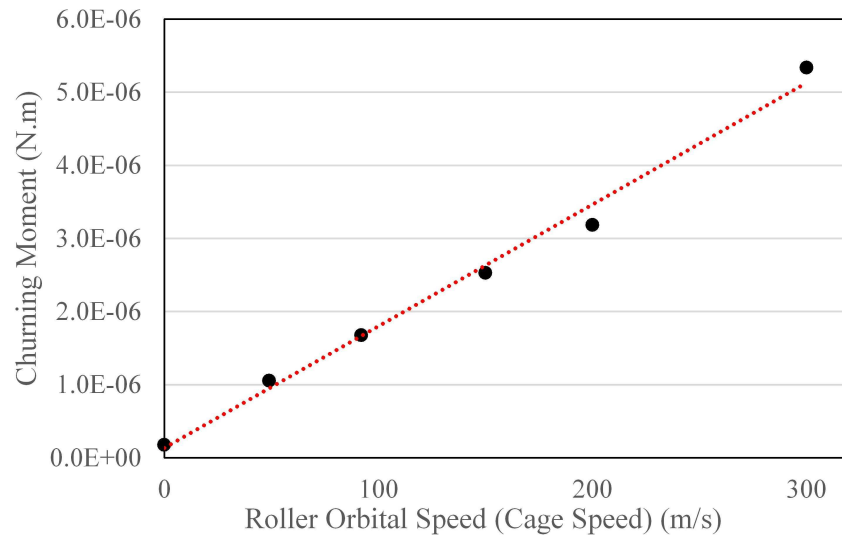
The effect of the roller length is first to change the area of the cylindrical surface, which is linear to the moment in Rumberger's formula. For the isolated finite-length cylinder element, the linear relationship is also found for the cylindrical surface, as shown in Fig. 3.22. Whereas, the length of the roller shows slight influence to the moment acting on the roller end (see Fig. 3.23). For the roller with a radius $r=3.57\text{mm}$, with the length changing from 1mm to 10mm, the churning moment on the end changes less than 8%, and from 1 mm to 40 mm, the moment changes less than 20%. This phenomenon is similar with the drag coefficient on the finite circular cylinder. As shown in Fig. 3.10, for relative short cylinders, $1 < L/D < 6$, there is a very small change rate of drag coefficient and the curve appears almost as a horizontal line. So that it could be assumed that in the application of cylindrical roller bearing which has a limited range of aspect ratio L/D , the length of circular cylinder does not change churning moment on the roller end significantly, so that its effect could be ignored in the formulation.

While for the radius of the roller, it changes not only the area of the cylindrical surface and the roller end, but the Reynolds number of the flow around the cylinder. In account that the Reynolds number is also related to the fluid property, the roller radius is outjected and analyzed independently, instead of the dimensionless Reynolds number which is used in Rumberger and von Karman's formula. It is found that the moment on the cylindrical surface is proportional to the third power of the roller radius, while the moment on the roller end is proportional to the four power of the roller radius, as shown in Fig. 3.24.

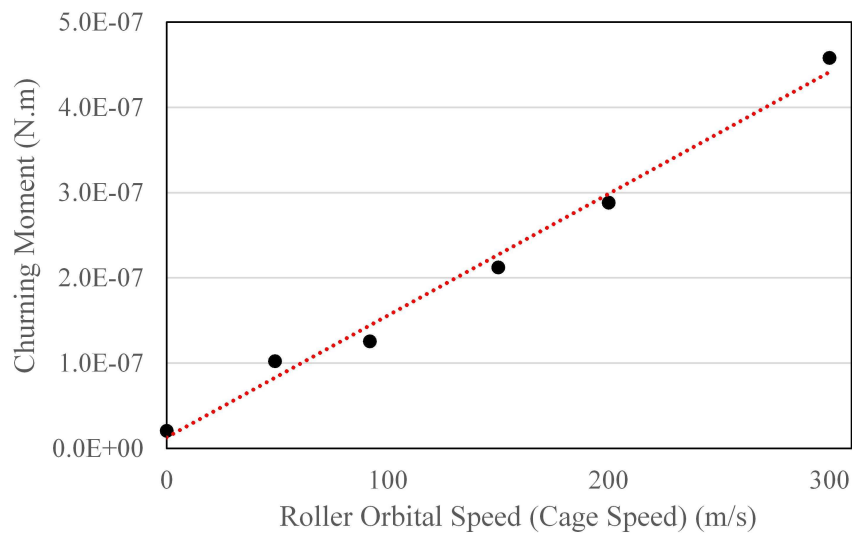
Similarly, for the fluid properties, in Rumberger and von Karman's model, the fluid density is not only related directly in the formula, but appears also both in the dimensionless Reynolds and Taylor numbers, together with the fluid viscosity. By comparing the five lines in Fig. 3.25, it could be found that the churning moment on the roller cylindrical surface is almost linear to the fluid density. It is the same for the churning moment on the roller end.

The viscosity is one of the most important physical properties of the lubricant, which is a key element in improving the bearing efficiency and performance. As shown in Figure 3.26, based on a series of calculations, the relationship between the churning moments and the fluid viscosity is found to be exponential, both for the cylindrical surface and the roller end.

To sum up, the index factors in the Eq. 3.4 are shown in Table 3.1.



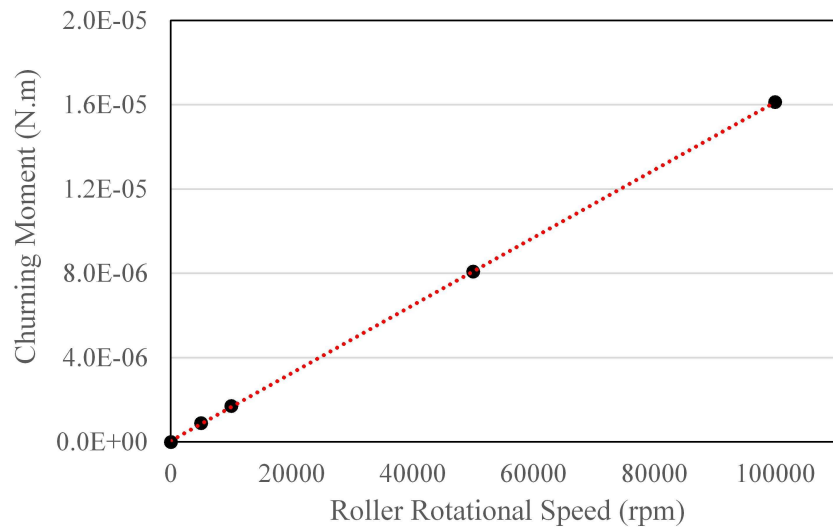
(a) Cylindrical surface



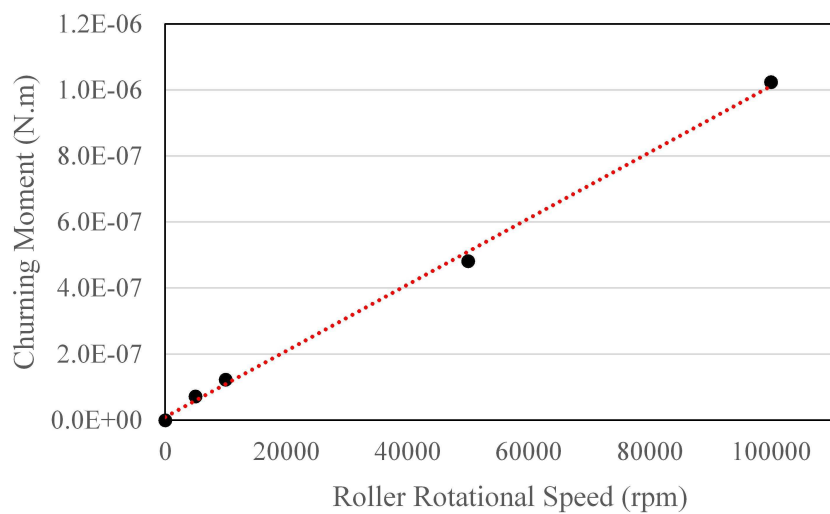
(b) Roller end

Figure 3.20: Influence of the roller orbital speed (i.e. the cage speed) on the churning moment (Configuration 1)

3. Drag coefficient and churning moment in roller bearings



(a) Cylindrical surface



(b) Roller end

Figure 3.21: Influence of the roller rotational speed on the churning moment (Configuration 1)

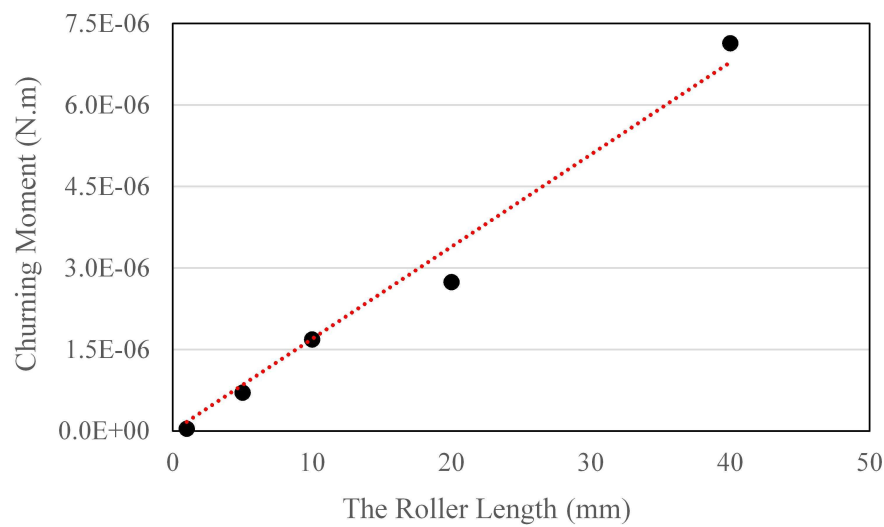


Figure 3.22: Churning moment on the cylindrical surface as a function of the roller length (Configuration 1)

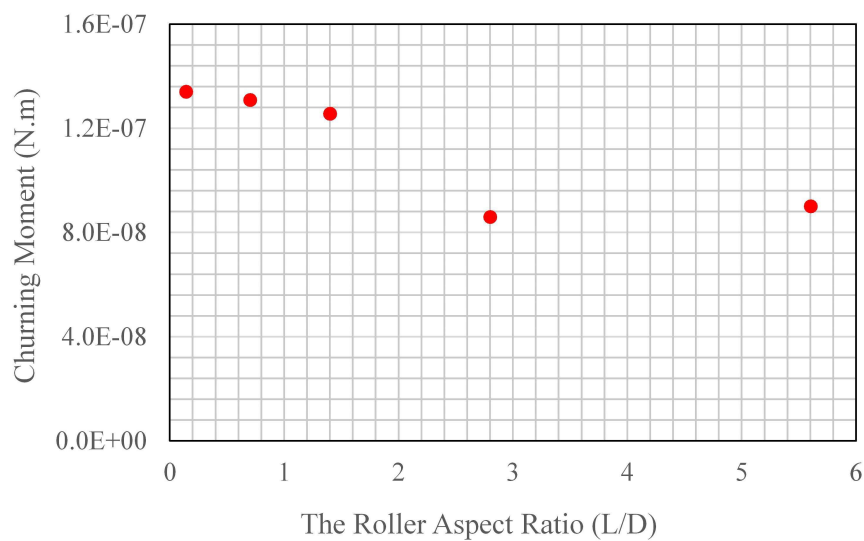
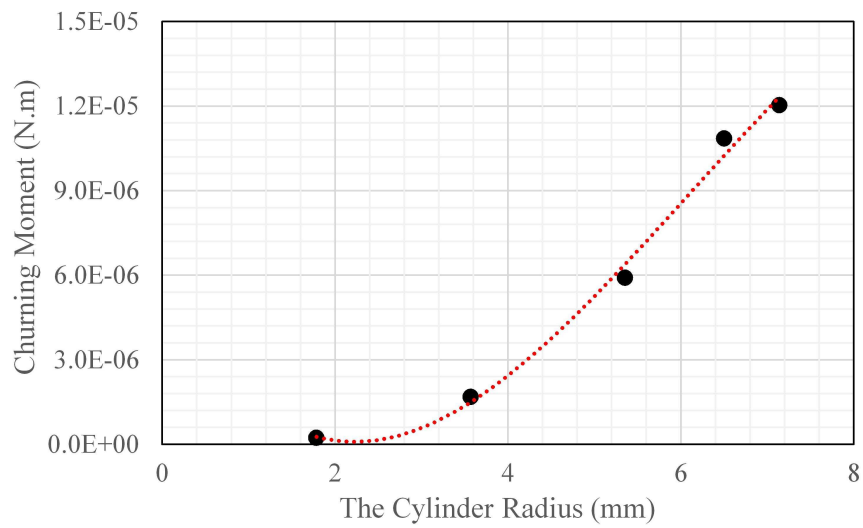


Figure 3.23: Influence of the roller aspect ratio on the churning moment (Configuration 1)

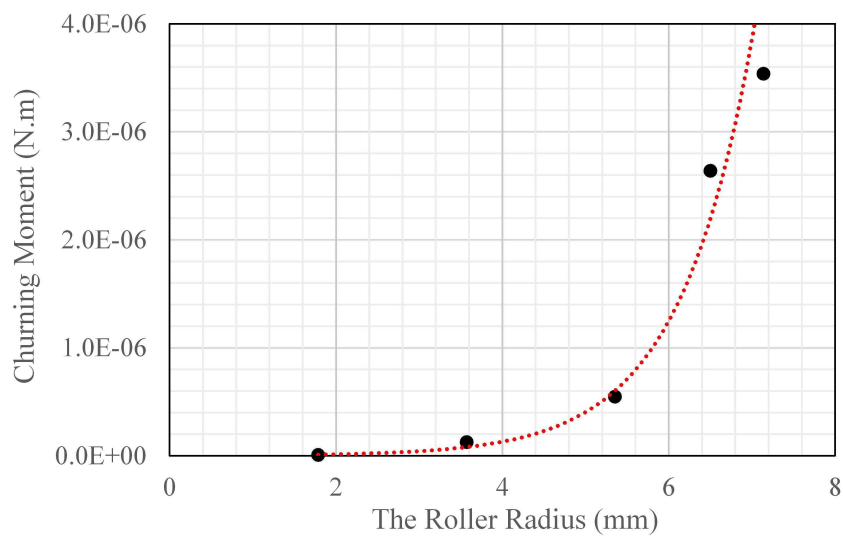
Tableau 3.1: Index coefficient for the isolated cylinder in open space (Configuration 1)

Location	ρ	μ	V	ω	L	r
Cylindrical surface	1	0.263 (Re<900)	1	1	1	3
		0.871 (Re>900)				
Roller ends	1	0.536	1	1	0	4

3. Drag coefficient and churning moment in roller bearings

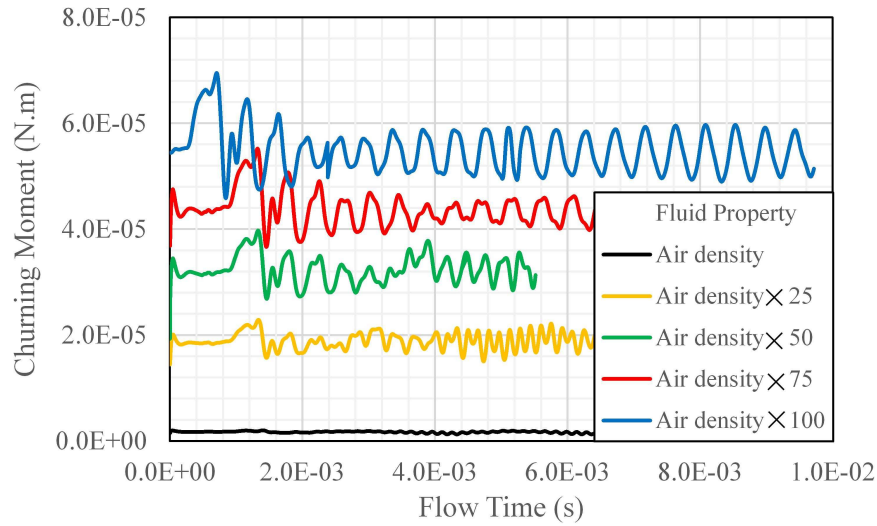


(a) Cylindrical surface

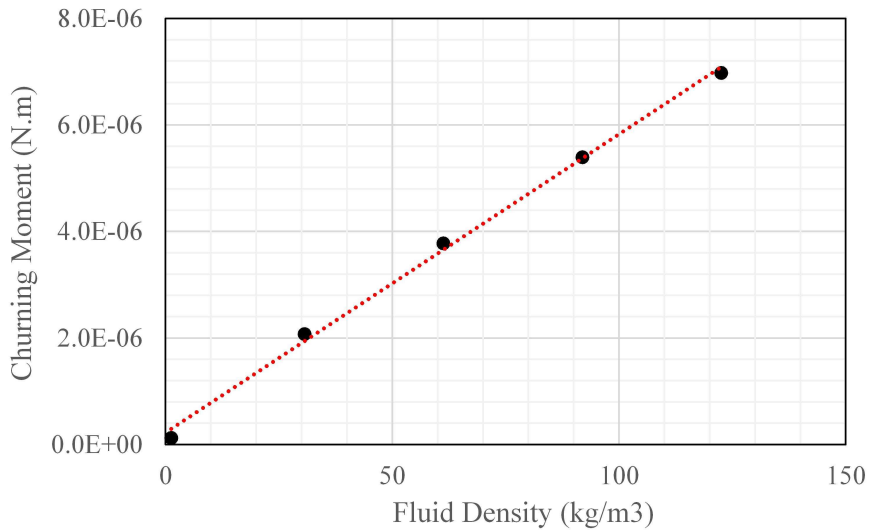


(b) Roller end

Figure 3.24: Churning moment on the roller as a function of the roller radius (Configuration 1)



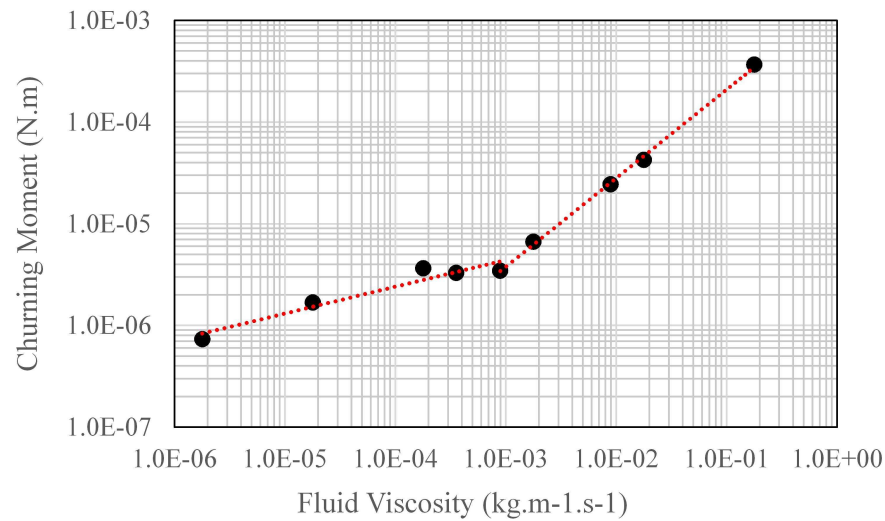
(a) Cylindrical surface



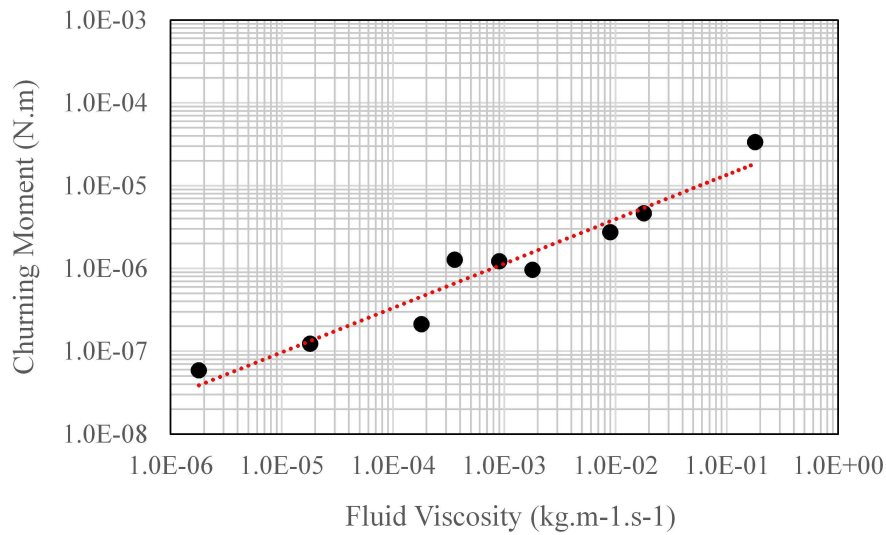
(b) Roller end

Figure 3.25: Influence of the fluid density on the churning moment (Configuration 1)

3. Drag coefficient and churning moment in roller bearings



(a) Cylindrical surface



(b) Roller end

Figure 3.26: Influence of the fluid viscosity on the churning moment (Configuration 1)

3.3.1.3 Formula fitting

With all the computational database in hand, a formula suitable for predicting churning moments on the isolated finite-length circular cylinder in stream flow could be proposed. In the formulation, the roller length and radius are replaced by the area surface. The formula of churning moment on the cylindrical surface summarized from the CFD simulation could be written as:

$$M_c = M_{c0} + M_{c1} \quad (3.5)$$

$$M_{c0} = \tau A_c r \quad (3.6)$$

$$M_{c1} = \begin{cases} C_1 \rho V \omega A_c r^2 \mu^{0.263} & \text{if } Re < 900 \\ C_2 \rho V \omega A_c r^2 \mu^{0.871} & \text{if } Re \geq 900 \end{cases}, C_1 = 7.864 \times 10^{-2}, C_2 = 4.2 \quad (3.7)$$

And the formula of churning moment on the roller end should be

$$M_e = M_{e0} + M_{e1} \quad (3.8)$$

$$M_{e0} = \frac{1}{2} C_{e0} \rho \omega^2 r^5 \quad (3.9)$$

$$M_{e1} = C_{e1} \rho V \omega A_e r^2 \mu^{0.536}, C_{e1} = 8.984 \quad (3.10)$$

It should be noted that, because the Reynolds number considers several parameters, including the density, the viscosity and the radius, it is difficult to meet the dimension restriction and the exponential relationship at the same time. So that in the formula fitting, the dimension restriction is given up.

3.3.2 Churning moments on several rotating cylinders

Different from the model of one isolated finite-length circular cylinder in stream flow, as in rolling bearings, each roller element is not isolated and is surrounded by rings and other rollers front and back. So that the configuration with three in-line finite circular cylinders is investigated numerically to reveal the characteristics of churning moment in rolling bearings. As the isolated circular cylinder model, different running conditions and fluid properties are analyzed to obtain their relationship with the roller's churning moments.

It should be emphasized that in Configuration 2, two flat walls replace the inner and outer rings and the ring's rotation is ignored whose influence has been proved to be slight (see Figure 3.27). So that both the flat walls are set to be fixed in the calculation.

As shown in Figs. 3.28 and 3.29, the churning moments acting on the cylindrical surface and the roller end are all linear with the roller orbital speed and the roller rotating

3. Drag coefficient and churning moment in roller bearings

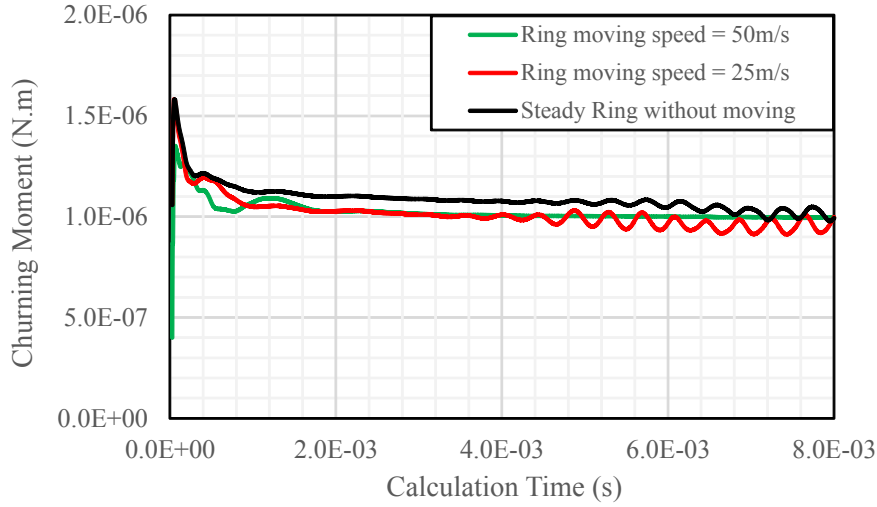


Figure 3.27: Influence of the ring moving speed to churning moment on the cylindrical surface (Configuration 2)

speed, as for the isolated cylinder model. In addition, the churning moments are not zero when the roller orbital speed is zero, conversely to the formula by Rumberger and von Karman's, as for a static component.

For the roller length, the relationship is verified to be the same as that in the model of one isolated circular cylinder, which is linear to the churning moment on the cylindrical surface, as shown in Figure 3.30. Besides, it doesn't change the moment acting on the cylinder end obviously. For the effect of the radius of the roller to its churning moments, the relationship obtained in the first configuration is proved to be suitable for the model with several in-line circular cylinders, as shown in Figure 3.31.

While for the fluid properties, including the fluid density and viscosity, their relationships with the churning moments are illustrated in Figs. 3.32 and 3.33. Respectively, the churning moment on the rollers is linear to the fluid density and exponential to the fluid viscosity.

To sum up, the formula suitable for churning moments prediction in rolling bearings could be proposed. For the churning moment on the cylindrical surface,

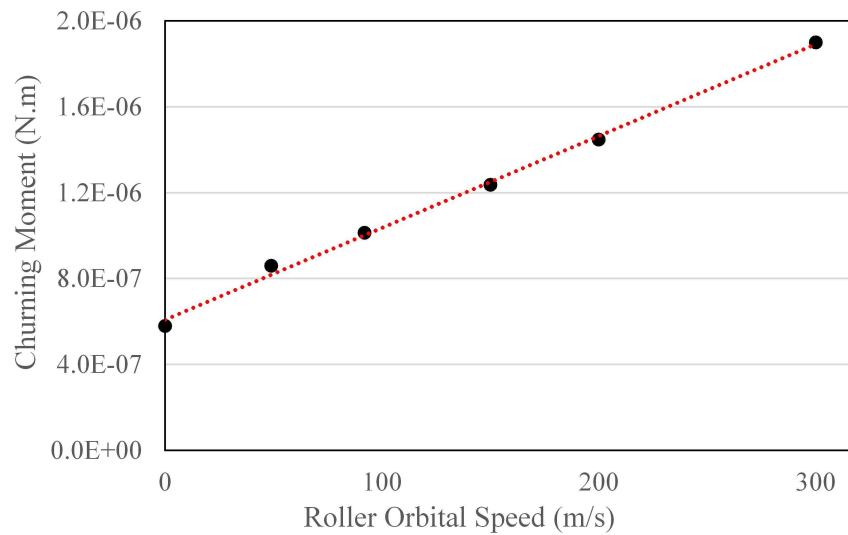
$$M_c = M_{c0} + M_{cs} \quad (3.11)$$

$$M_{c0} = \tau A_c r \quad (3.12)$$

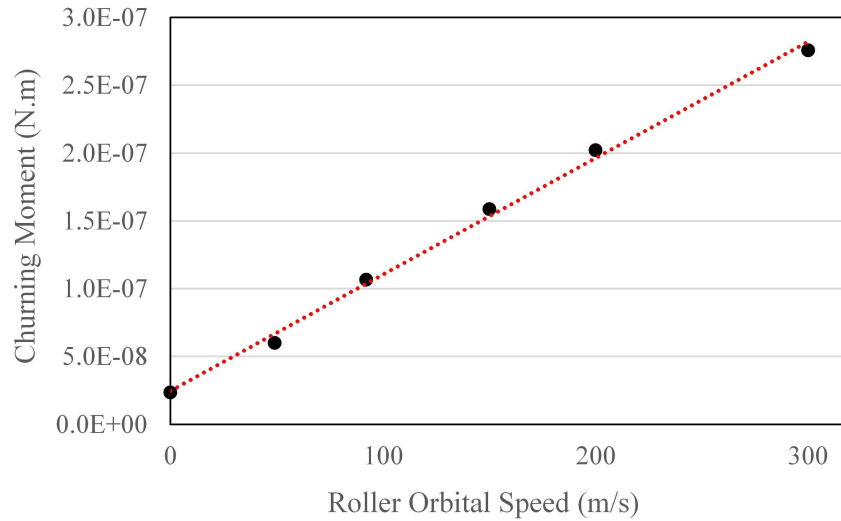
$$M_{cs} = C_{cs} \rho V \omega A_c r^2 \mu^{0.818}, C_{cs} = 30.745 \quad (3.13)$$

And the formula of churning moment on the roller end should be

$$M_e = M_{e0} + M_{es} \quad (3.14)$$



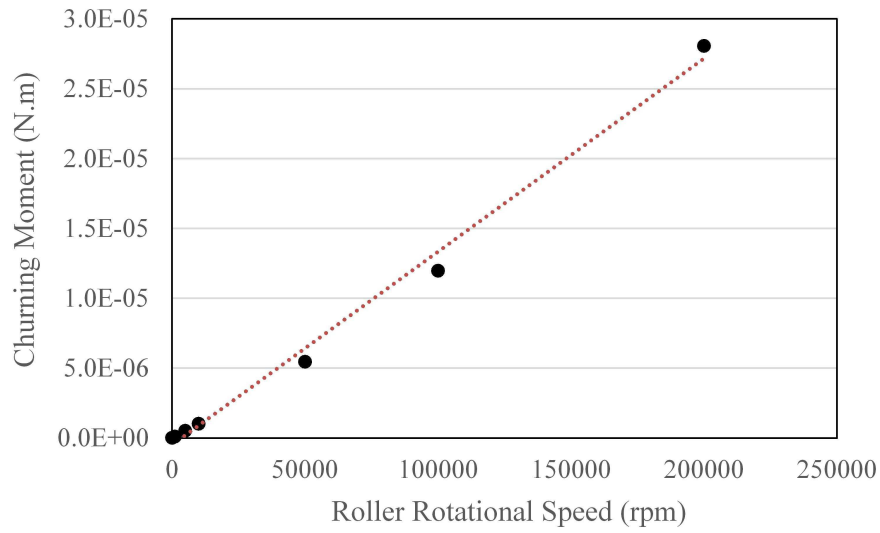
(a) Cylindrical surface



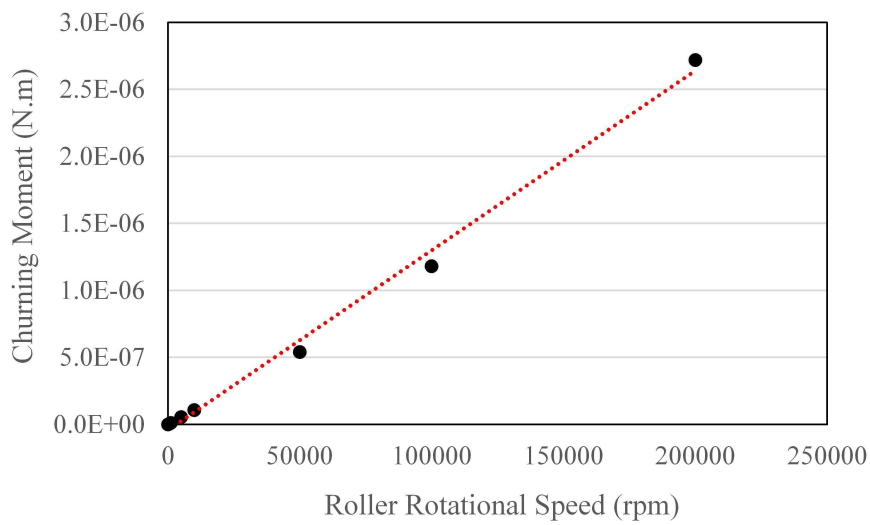
(b) Roller end

Figure 3.28: Churning moment as a function of the roller orbital speed (Configuration 2)

3. Drag coefficient and churning moment in roller bearings

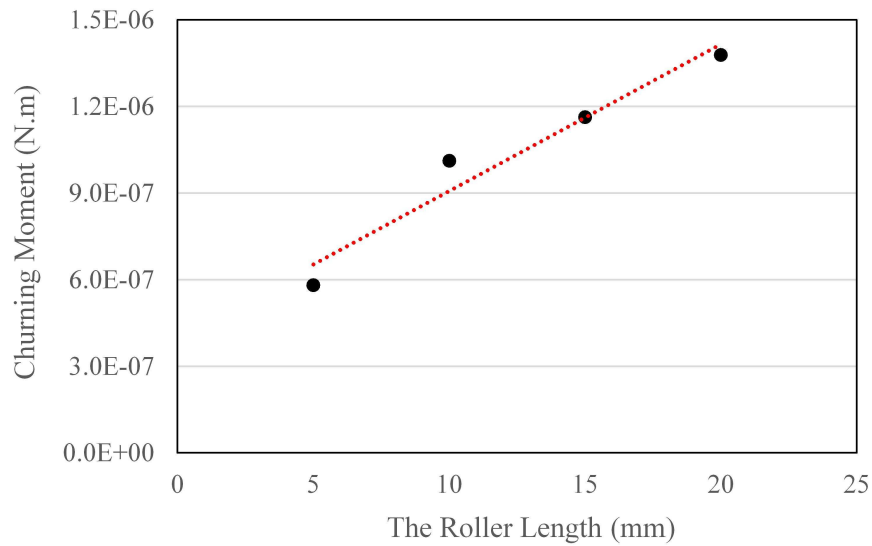


(a) Cylindrical surface

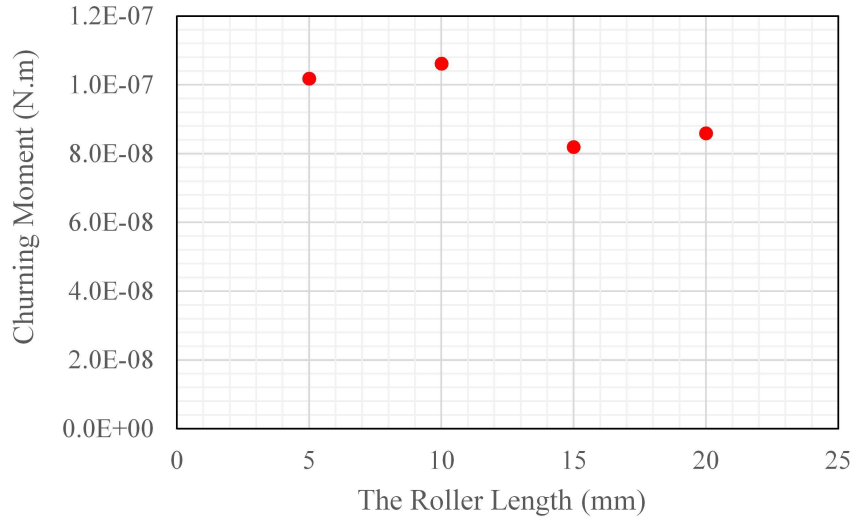


(b) Roller end

Figure 3.29: Churning moment as a function of the roller rotational speed (Configuration 2)



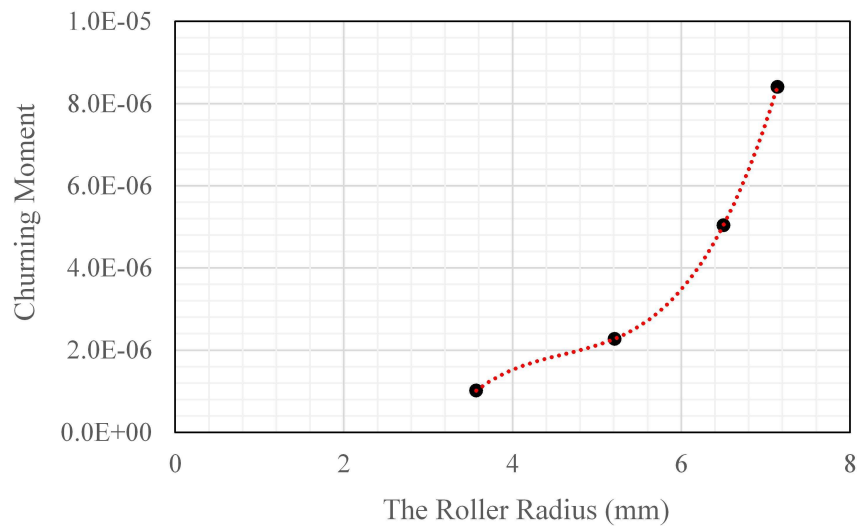
(a) Cylindrical surface



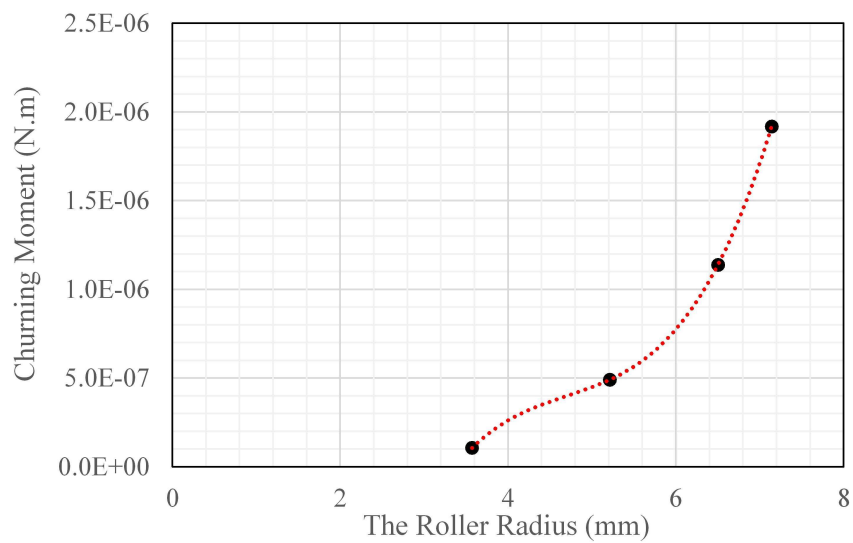
(b) Roller end

Figure 3.30: Churning moment as a function of the roller length (Configuration 2)

3. Drag coefficient and churning moment in roller bearings

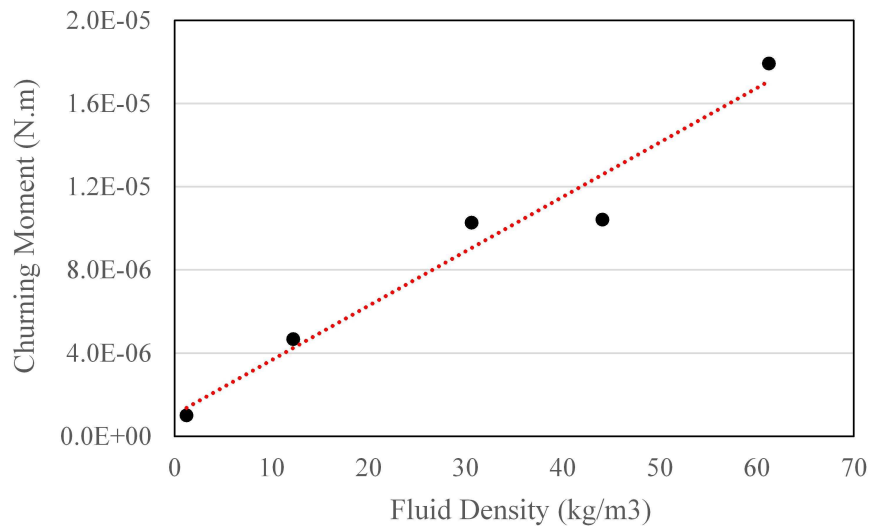


(a) Cylindrical surface

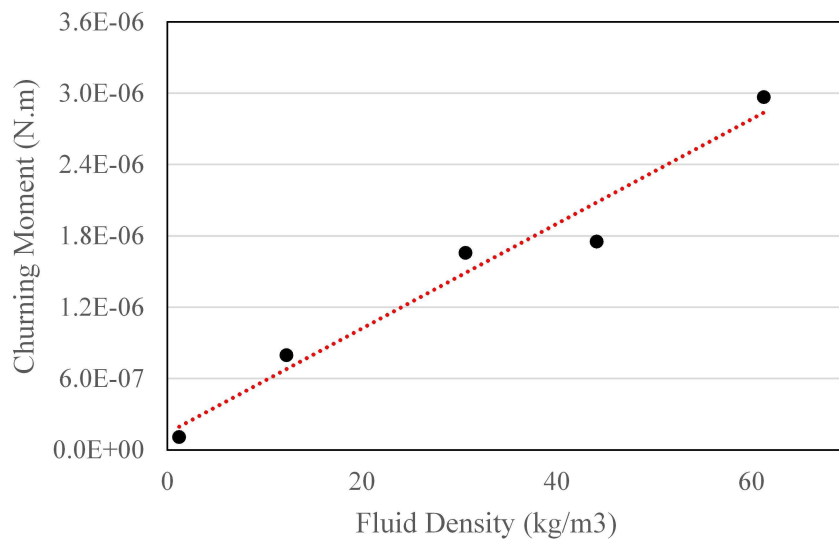


(b) Roller end

Figure 3.31: Churning moment as a function of the roller radius (Configuration 2)



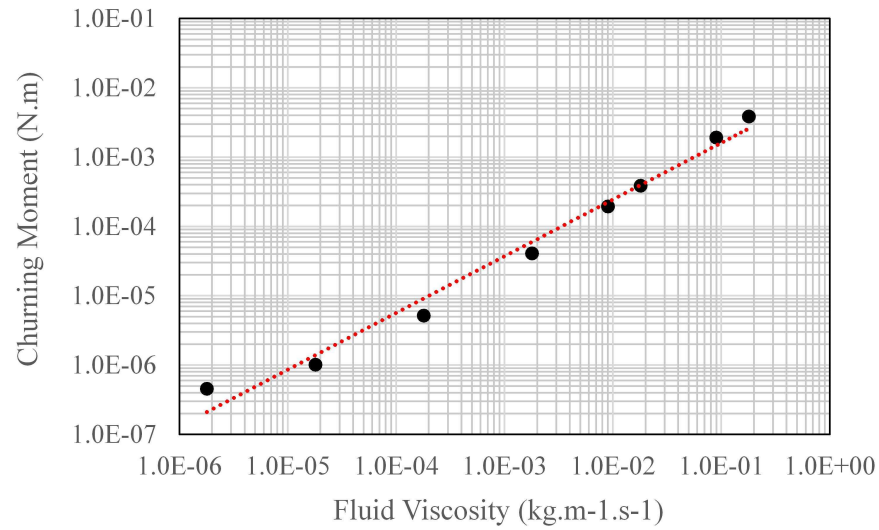
(a) Cylindrical surface



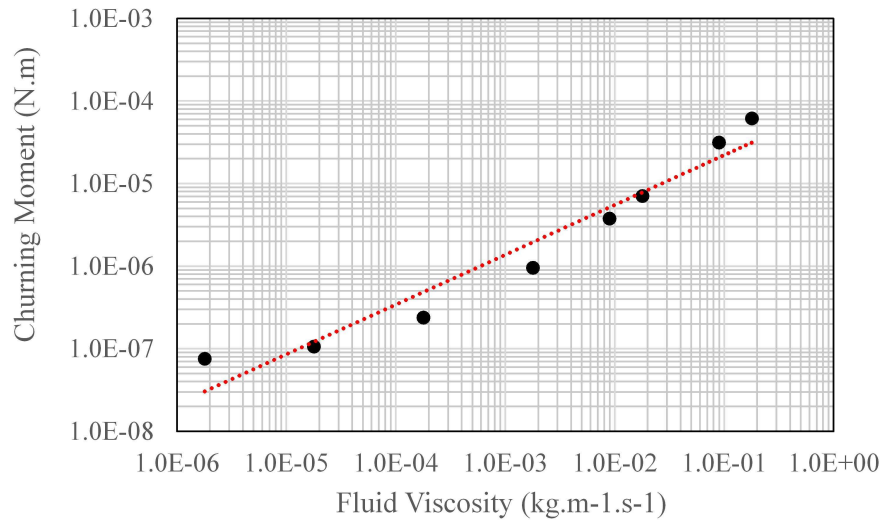
(b) Roller end

Figure 3.32: Churning moment as a function of the fluid density (Configuration 2)

3. Drag coefficient and churning moment in roller bearings



(a) Cylindrical surface



(b) Roller end

Figure 3.33: Churning moment as a function of the fluid viscosity (Configuration 2)

$$M_{e0} = \frac{1}{2} C_{e0} \rho \omega^2 r^5 \quad (3.15)$$

$$M_{es} = C_{es} \rho V \omega A_e r^2 \mu^{0.603}, C_{es} = 4.174 \quad (3.16)$$

It could be found that, in both configurations with different roller arrangements, the influence of the running conditions and the fluid properties, are the same, except the index number of the fluid viscosity. It indirectly demonstrates that appropriate simplification to the rolling bearing geometry structure does not affect the accuracy of the numerical model considerably.

3.4 Conclusion

Appropriate lubricant supply for roller bearing in high speed rotating machinery is essential for its efficient and reliable operation. While interaction between roller elements and lubricant oil in bearing cavity is empirical and uncertain so far, which could change the bearing's behavior obviously.

In this chapter, the numerical simulation method developed in Chapter 2 is employed to figure out drag force and churning moments acting on circular cylinder in high speed roller bearings. For the drag coefficient, first the configuration with one isolated rotating circular cylinder is analyzed to check the influence of the roller rotating by its own axis. And the relationship of drag coefficient varying with Reynolds number suitable for the circular cylinder of $1 < L/D < 6$ in open space is obtained. Then the flow field is sandwiched by two flat walls to represent a simplified arrangement of roller bearings, with several in-line cylinders. The flow passing the cylindrical surface is blocked, while the inflow is restricted by the sharp ends and the presentation of other cylinders in the vortex formation region, with local vortices limited in the gap between two adjacent cylinders. As a consequence, pressure distribution around the cylindrical surface is evened and drag coefficient is decreased to a low level. And the drag coefficient more suitable for drag force calculation in roller bearings is finally obtained.

For the churning moments analyzing, the configuration with one isolated circular cylinder is analyzed as well, to illustrate the influence of the roller orbiting motion, which is ignored in previous empirical formulas. It is found that the roller orbital speed is a remarkable element that has to be considered since it affects linearly the churning moments on the roller surface. After that, the configuration with several in-line rotating cylinders sandwiched between two flat walls is studied. Based on a series of CFD simulations, the effects of different factors, including the roller geometrical parameters, the running conditions and the fluid properties, are quantified in view of the application in rolling bearings. In the end, two individual formulations are proposed for evaluating churning moment components on the roller cylindrical surface and two circular ends, respectively.

However, it should be noted that this simulation is done in an one-phase environment, with equivalent fluid property. And the cage is ignored in the calculation either. As a

3. Drag coefficient and churning moment in roller bearings

result, the oil volume fraction inside the bearing cavity should be studied, which will be the main work in Chapter 4.

Besides, our ongoing and coming work on this topic focuses on investigating the flow in cylindrical roller bearings with other numerical methods, and taking the influence of the cage into account. Additionally, an experimental equipment is needed for the validation of the numerical-based formulation.

Chapter 4

Two-phase flow in bearing cavity

In this chapter the coupled level-set volume of fluid method is conducted to reveal oil/air two-phase flow inside the bearing cavity, for the quantification of oil volume fraction in different operating conditions.

Contents

4.1	Introduction	83
4.2	Numerical model	84
4.2.1	Problem definition and computational domain	84
4.2.2	Meshes and boundary conditions	85
4.2.3	The CLS-VOF model and governing equations	86
4.2.4	Fluid properties	88
4.2.5	Numerical Methods	88
4.3	Calculation results	89
4.3.1	Nonuniform oil/air distribution	89
4.3.2	Parameters effects to oil volume fraction	90
4.4	Comparion with existing hydraulic loss models	103
4.4.1	Existing hydraulic losses prediction models	104
4.4.2	Calculation results	106
4.5	Conclusion	110

4.1 Introduction

High speed roller bearing is commonly used as an important component in aircraft turbine engine, which needs lubricant oil to ensure its steady running and capability. Sufficient oil flow rate into the bearing is essential with an increasingly severe operating environment, to achieve sufficient lubricating and desired temperatures [GLO 11]. Larger amounts of oil flow can definitely enhance the heat dissipation. However, it leads to larger capacity pumps and higher power consumption of the engine. Further, larger oil feeding may increase excessive parasitic losses when rolling elements translate and rotate into the fluid environment [FLO 05]. These put increasing demands on deep understanding of oil behavior inside the bearing cavity, to optimize its lubricating and cooling method design.

Besides, in previous chapters, the interaction between the fluid and roller elements have been studied. Whereas there is an important assumption used in the investigation that the bearing element is completely flooded in a uniform fluid. The truth is that high speed roller bearings never are completely flooded with lubricant, and seldom are more than 15 to 20 percent full of oil within the bearing for very high speed operation [ADE 14]. Motion of the many moving parts within the bearing, in particular the pumping action of the rollers, will tend to induce an air oil mixture within the bearing cavity.

In view of that, it becomes necessary to quantify the oil/air volume ratio when comparing the mixture to an one-phase fluid [WU 17]. The equivalent fluid properties are taken as those in roller drag and churning effect calculations [NIC 17]. That's to say, it is of importance to select an appropriate oil volume fraction in the bearing cavity since heat generation and bearing temperatures are dependent on this factor [CAV 05]. Therefore, a detailed investigation of the oil/air two-phase flow inside the bearing cavity is important and valuable.

For two-phase flow investigation in bearing chamber or gearbox, the Volume of Fluid (VOF) method is widely used, which has been validated to be reliable and reasonable by a series of experiments [MAR 11][SEE 09]. The basic theory of the VOF model has been introduced in Chapter 1. Due to the high speed rotating and strong impact between the oil injection and bearing components, it is difficult to catch the oil/air interface. In view of this, an improved Coupled-Level-Set VOF model (CLS-VOF) is employed to study the oil-air two phase flow inside the bearing cavity [MÉN 07].

In this chapter, a numerical method is employed to investigate the oil/air two-phase flow behavior inside the high speed roller bearing with under-race lubrication, which is relatively unknown with somewhat scant attention. A detailed discussion of the oil distribution along the bearing circumference is proposed with different lubricating schemes and operating conditions. Particularly bearing components rotational speeds are studied separately to verify their effects. The results can be used for the precise lubrication design to optimize the oil volume fraction inside the bearing.

Tableau 4.1: Roller bearing specifications with under-race lubrication

Pitch diameter(mm)	48.5
Bearing width (mm)	14
Number of rollers	16
Roller diameter(mm)	7.14
Roller length(mm)	10

4.2 Numerical model

4.2.1 Problem definition and computational domain

For the under-race lubrication, the lubricant oil is supplied into the bearing cavity through the inner race apertures by centrifugal force and high pressure. The aperture, or named the nozzle in this work, is aimed vertically at the inner raceway surface and rotates along with the inner ring. The rollers rotate by its own axis and orbit along the circumference runway with the cage. Previous studies show that the oil volume fraction inside the bearing cavity after the bearing reaches thermal and dynamical equilibrium is a function of the bearing speed, oil property, and oil volume flow rate [YAN 16a]. In some cases, like the intershaft supporting bearing, the outer ring rotates together with the inner ring. This also exerts an impact on the oil distribution. After lubricating and cooling the bearing components, the oil removes into the bearing chambers on both sides of the bearing.

To simulate the oil/air two-phase flow inside the roller bearing with under-race lubrication, a simplified configuration is built, with 16 cylindrical cylinders as the rollers, two hollow rings as the inner and outer rings, and the cage. One nozzle is set to replace the apertures in the inner race for oil supplying. A schematic diagram of the cylindrical roller bearing with under-race lubrication is shown in Figure 4.2. The fluid domain contains the flow field inside the bearing cavity and the oil-inlet nozzle. The flow field hollows all rollers and the cage between the inner and outer runways. To deal with the contact feature between rollers and raceway in practical conditions [ADE 15], there is a gap of $1/20$ of roller radius between rollers and two rings in the simulation configuration. This gap is empirical but enough for the improvement of mesh quality. As a result, the pumping action of the rollers in the roller-raceway contact can't be revealed [GUH 93].

In the numerical investigation, the bearing chambers on both sides of the bearing is ignored and the bearing geometrical edge is taken as the flow field boundary, which is however unreasonable [ZHA 14]. The oil/air flow inside the bearing cavity is undoubtedly affected by that in the bearing chamber which plays a role of boundary condition. Nevertheless, the flow inside the bearing chamber is too complicated to be simulated together, with complicated oil droplet/oil film/wall/scavenge system/sealing air mixing interaction [LIU 13, HU 13, ZHO 14]. Thus here the flow space inside the bearing is assumed to be directly open to the ambient air.



Figure 4.1: Cylindrical roller bearing structure

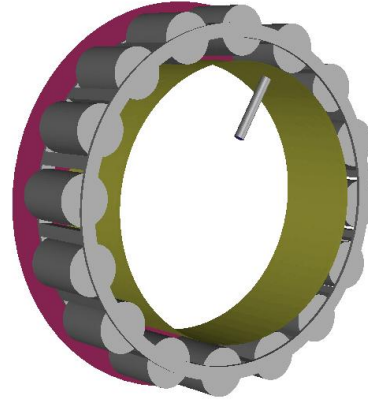


Figure 4.2: Configuration of the bearing with under-race lubrication

4.2.2 Meshes and boundary conditions

The cylindrical roller bearing specification used in the numerical investigation is listed in Table 4.1. The flow field inside the bearing is discretized with unstructured tetrahedral mesh in view of its complicated construction. And the nozzle is discretized with structure hexahedral mesh. The mesh density is designed following the research purpose. The total number of the combination element is about 472,737, with about 108,514 nodes, as shown in Figure 4.3. The mesh is built with ANSYS-ICEM.

In the contact regions, the gap between the raceway and rollers is enlarged to avoid mesh distortion. And there is a minimum of 3 elements between the gap at 10 levels of refinement and average y^+ (the dimensionless wall distance) in the range $7 < y^+ < 21$ on the walls. A grid independence test of the numerical solutions has been made primarily, to ensure the validity of the numerical results, which shows slight change to the results.

The nozzle in the inner ring is set as the only velocity inlet of the entire computation domain and the velocity value is determined by different operations. Both end faces of the outlet flow field are specified as the pressure outlet. The reference pressure is the standard atmospheric pressure. Considering the relative rotational motion between the flow field inside the bearing and the flow area of the nozzle, interferences are formed between them to complete the data transfer. The standard wall function is adopted for near wall treatment and no-slip boundary condition is adopted at the wall.

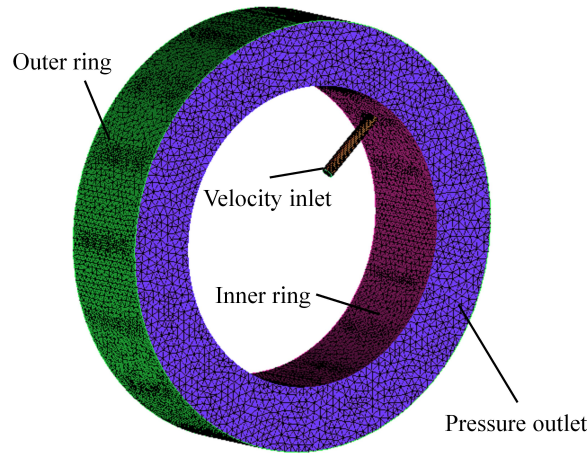


Figure 4.3: Computational mesh structure and boundary condition

4.2.3 The CLS-VOF model and governing equations

The analysis of the whole flow passage inside the roller bearing with under-race lubrication involves the air and oil two-phase flow. To track the air-oil two-phase flow, the coupled level-set volume of fluid (CLS-VOF) for multiphase flow is used [MÉN 07]. The level-set method is a popular interface-tracking method for computing two-phase flows with topo-logically complex interfaces [OSH 01]. This is similar to the interface tracking method of the VOF model. In the level-set method, the interface is captured and tracked by the level-set function [TOR 00], defined as a signed distance from the interface. Because the level-set function is smooth and continuous, its spatial gradients can be accurately calculated. This in turn will produce accurate estimates of interface curvature and surface tension force caused by the curvature. However, the level-set method is found to have a deficiency in preserving volume conservation.

On the other hand, the VOF method is naturally volume conserved, as it computes and tracks the volume fraction of a particular phase in each cell rather than the interface itself [PRO 09]. The weakness of the VOF method lies in the calculation of its spatial derivatives, since the VOF function (the volume fraction of a particular phase) is discontinuous across the interface. To overcome the deficiencies of the level-set method and the VOF method, a coupled level-set and VOF approach (CLSVOF) is advised, to take advantage of the mass conservation of the VOF method and the sharp interface capturing of LS method [YAN 06]. Although two separate fields are defined, the VOF advection equation is solved instead of both the VOF and LS equations as required in the standard CLS-VOF method.

In the level set method, a smooth level-set function ϕ is defined as a signed distance to the interface. Accordingly, the interface is the zero level-set, $\phi(x, t)$ and can be expressed as $\Gamma = \{x \mid \phi(x, t) = 0\}$ in a two-phase flow system:

$$\phi(x, t) = \begin{cases} +|d| & \text{if } x \in \text{the primary phase} \\ 0 & \text{if } x \in \Gamma \\ -|d| & \text{if } x \in \text{the secondary phase} \end{cases} \quad (4.1)$$

Where d is the distance from the interface. In the roller bearing, the primary phase means the air and the secondary phase is the injected lubricant oil.

The evolution of the level-set function can be given in a similar fashion as to the VOF model:

$$\frac{\partial \phi}{\partial t} + \nabla \cdot (\vec{u} \phi) = 0 \quad (4.2)$$

where \vec{u} is the underlying velocity field.

And the momentum equation can be written as

$$\frac{\partial(\rho \vec{u})}{\partial t} + \nabla \cdot (\rho \vec{u} \vec{u}) = -\nabla p + \nabla \cdot \mu [\nabla \vec{u} + (\nabla \vec{u})^T] - \vec{F}_{sf} + \rho \vec{g} \quad (4.3)$$

In the Eq.4.3, \vec{F}_{sf} is the force arising from surface tension effects given by:

$$\vec{F}_{sf} = \sigma k \delta(\phi) \vec{n} \quad (4.4)$$

where: $\sigma = \text{surface tension coefficient}$ $k = \text{local mean interface curvature}$ $\vec{n} = \text{local interface normal}$
and

$$\delta(\phi) = \begin{cases} 0 & |\phi| \geq \alpha \\ \frac{1 + \cos(\pi \phi / \alpha)}{2\alpha} & |\phi| < \alpha \end{cases} \quad (4.5)$$

where $\alpha = 1.5h$ is the thickness of the interface and h is the grid spacing.

In some cases, applying the default surface tension force as written in Equation 4.4 can lead to spurious currents appearing in the solution [SUS 98]. To mitigate these effects, Fluent offers two weighting functions that redistribute the surface tension force towards the heavier phase in the interface cells.

In the density correction formulation, Equation 4.4 is modified by introducing a density ratio:

$$\vec{F}_{sf} = \frac{\rho}{0.5(\rho_1 + \rho_2)} \sigma k \delta(\phi) \vec{n} \quad (4.6)$$

where ρ is the volume-based density.

The normal and curvature of the interface, which is needed in the computation of the surface tension force, can be estimated as

$$\vec{n} = \frac{\nabla\phi}{|\nabla\phi|} \Big|_{\phi=0} \quad (4.7)$$

$$k = \nabla \cdot \frac{\nabla\phi}{|\nabla\phi|} \Big|_{\phi=0} \quad (4.8)$$

By nature of the transport equation of the level-set function equation, it is unlikely that the distance constraint of $|\nabla\phi| = 1$ is maintained after its solution. The reasons for the lack of maintenance is due to the deformation of the interface, uneven profile, and thickness across the interface. Those errors will accumulate during the iteration process and cause large errors in mass and momentum solutions. A re-initialization process is therefore required for each time step. The geometrical interface-front construction method is used here. The geometrical method involves a simple concept and is reliable in producing accurate geometrical data for the interface front. The values of the VOF and the level-set function are both used to reconstruct the interface-front [XU 14]. Namely, the VOF model provides the size of the cut in the cell where the likely interface passes through, and the gradient of the level-set function determines the direction of the interface.

In this work, the coupled level-set volume of fluid method (CLS-VOF) is used for representing the free surface of the oil-air two phase flow inside the roller bearing cavity [YAG 16]. In this method the VOF method is used to capture interfaces, which can conserve the mass and overcome the disadvantage of nonconservation of mass in level-set method. By using the level-set function ϕ the disadvantages of VOF method, inaccuracy of curvature and bad smoothness of discontinuous physical quantities near interfaces, can be overcome. The performance of the CLS-VOF method has been evaluated by comparing with the available numerical and experimental results, and good agreement is obtained [ADE 14]. The CLS-VOF approach has been proven to have a very good potential and to be suitable for sharp interface simulation in roller bearing cavity and represent its oil distribution.

4.2.4 Fluid properties

The lubricant oil used here is respected to the MIL-L-23699 type lubricant oil with a popular trade name Mobile Jet 2, and the air is regarded as ideal at atmospheric pressure. Respectively, the lubricant oil density is 976 kg/m^3 while the air density is 1.225 kg/m^3 . The viscosity of the oil and air are respectively $0.018 \text{ kg/(m} \cdot \text{s)}$ and $1.7894 \times 10^{-5} \text{ kg/(m} \cdot \text{s)}$. The surface tension coefficient is taken as 0.43. During the calculations, the oil density is set as constant. With different operating conditions, the oil viscosity is varied to evaluate its effect.

4.2.5 Numerical Methods

The rotation of the inner and outer rings drives the rolling elements and the cage. After entering into the bearing, the lubricant oil is motivated by the orbiting rolling elements and the cage. The rotational speed of the cage is given as

$$\omega_c = \frac{1}{2} \frac{\omega_i(d_m - d_r)/2 + \omega_o(d_m + d_r)/2}{d_m/2} \quad (4.9)$$

where ω_c is the rotational speed of the cage, *rpm*; ω_i and ω_o are the rotational speed of the inner and outer rings respectively, *rpm*; d_r is the cylinder diameter and d_m is the pitch diameter of the bearing, *m*.

The CFD codes ANSYS Fluent is proposed to implement the complicated two-phase flow simulations. The finite volume method is used to discretely solve the governing equation. The central difference scheme is adopted for the diffusion and pressure terms of the momentum equation. The second-order upwind difference was adopted for the convection terms. The pressure was adopted for the PRESTO! (PREssure STaggering Option) format. The semi-implicit method for pressure-linked equations-consistent (SIMPLEC) method is adopted for the coupling solution of pressure and velocity.

To model the effect of turbulence in a high-speed rotating condition, the $k - e$ renormalization group (RNG) turbulence model is employed in this study. The RNG $k - e$ model considers the influence of high strain rate, large curvature overflowing and other factors, which can improve the accuracy under rotational flow [XIA 12].

The explicit CLSVOF formulation with transient time-stepping is used with the Global Courant number kept to less than 0.8 every time step. During the calculations, the convergence of the governing equations is detected by the residuals and the flux conservation of boundaries. The convergence criterion of residual of each velocity component and the volume of fluid function is set to be 10^{-5} , while the convergence criterion of residual of the turbulent kinetic energy and the turbulent kinetic energy dissipation rate is set to be 10^{-4} . In addition, the conservation of mass flow rate of inlet and outlet is monitored. When the net mass flow rate between the inlet and outlet decreases to one percent of the inlet flow rate, the calculation is considered to catch the convergence. The simulation results will be presented in detail.

4.3 Calculation results

4.3.1 Nonuniform oil/air distribution

The simulated flow pattern in bearing cavity at different flow time is shown in Figure 4.4. The bearing rotates counter-clockwise and the inner ring rotational speed is 5000 rpm. The jet flow rate is about 2.1 L/min, with the nozzle diameter 1.5 mm and the jet velocity 20 m/s. It can be seen that with the calculation time, the oil-phase in bearing cavity increases gradually and occupies the whole circumference. The average oil volume fraction reaches a steady value finally. The nozzle circumferential position changes together with the inner ring's rotating. The oil distribution along the circumference of the bearing is nonuniform. The oil volume fraction gradually increases along the bearing rotating direction. And it reaches the peak in the position quite close to the nozzle. It is because that most of the lubricant oil flows along the circumferential direction due to the rotating of

the inner ring and the agitation of the rolling elements and cage. The lubricant oil leaves the bearing from the end surface. Besides, more oil is thrown to the outer ring, not only because of the centrifugal force, but also the injecting kinetic energy [YAN 16b].

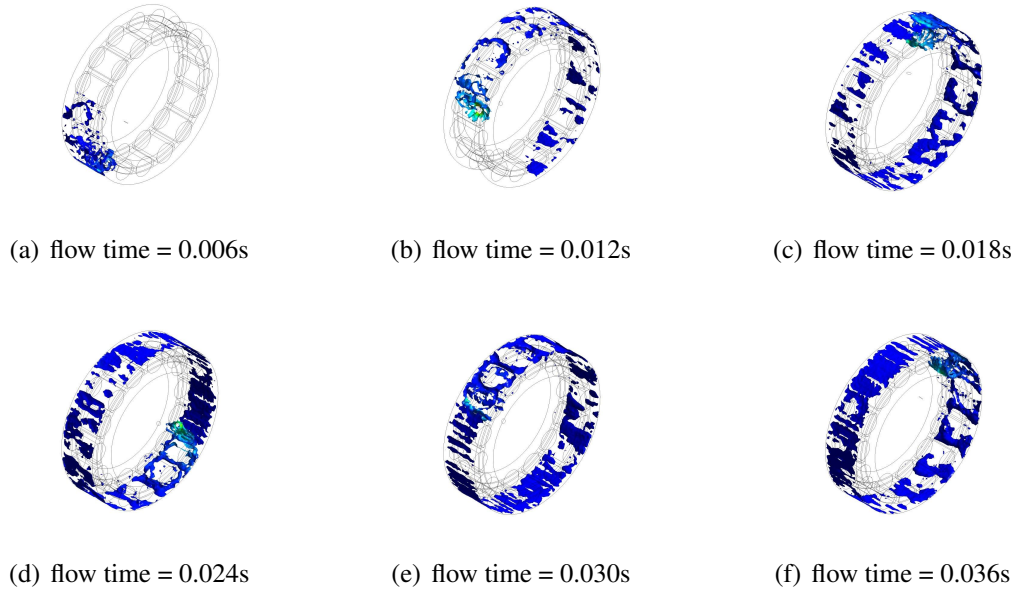


Figure 4.4: Oil distribution evolution inside the bearing cavity with flow time

The photographs of the flow pattern inside the bearing cavity at different rotational speeds (inner ring rotating) are shown in Figure 4.5. The inner ring rotating speeds are 5000 rpm, 10000 rpm, 20000 rpm and 40000 rpm, respectively. The injection velocity is 20m/s and the diameter of the inlet is 1.5mm, with a total oil volume flow rate of 2.1 L/min. It seems that the outer ring race is covered with oil phase at 5000 rpm and the bearing is poor-lubricated for the case at 40000 rpm, with most rollers naked in the air phase.

Figure 4.6 illustrates oil distribution along the circular of the bearing cavity at different inner ring rotational speeds. It could be summarized that, with the increasing of the inner ring rotating speed, oil volume fraction in bearing decreases and its distribution along the circumference is getting uniform. The influence of bearing rotating speed will be discussed carefully later.

4.3.2 Parameters effects to oil volume fraction

It is important to select an appropriate volume fraction of lubricant oil in the bearing cavity, since heat generation and bearing temperatures are dependent on this factor [YAN 17]. In general, a higher level of oil volume fraction inside the bearing cavity has an adverse effect on the windage drag and churning losses, while it is beneficial for the heat diffusion.

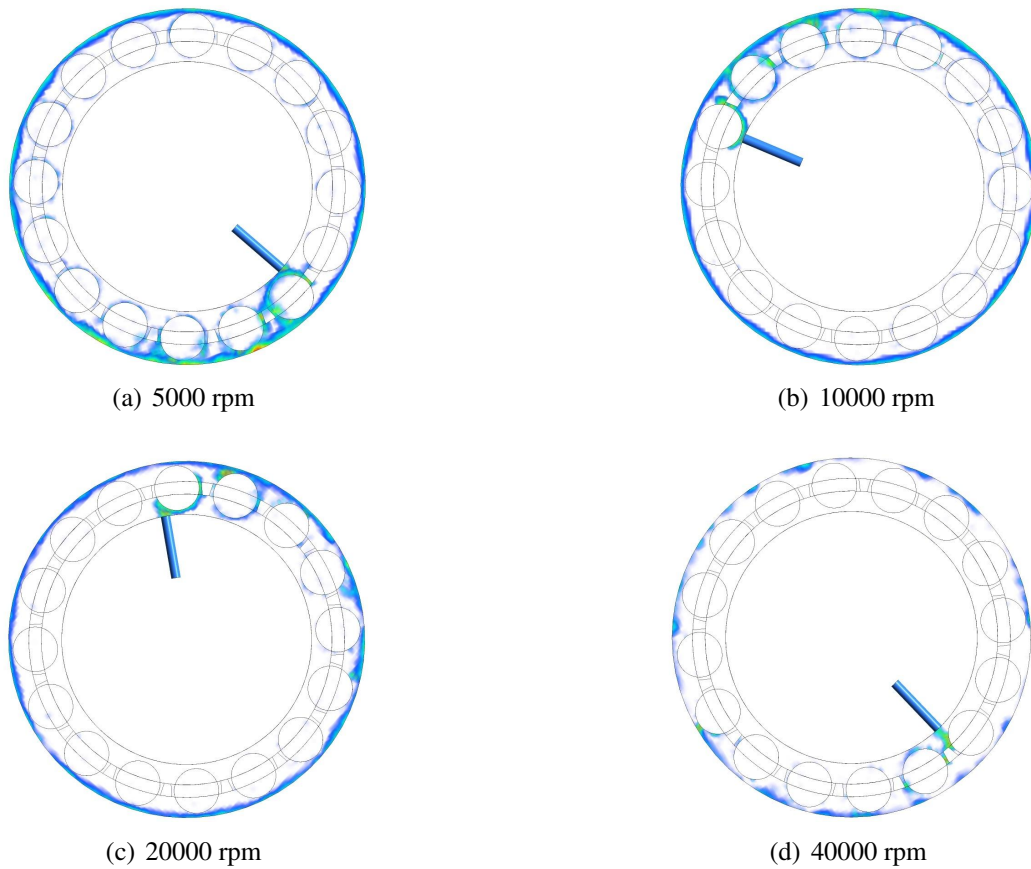


Figure 4.5: Oil volume fraction contours in the center cross-section with different rotational speeds

So that a balance between these two performance should be caught in the lubrication system design.

Thus, a reasonable estimate of the actual lubricant oil flow rate through the bearing cavity must be made, to improve the prediction performance. In this section, different parameters are tested numerically to quantify their effects to the oil volume fraction inside the bearing cavity. It is expected primarily that oil volume fraction varies with the oil flow rate, rotational speed, the nozzle design, and the oil property.

4.3.2.1 The effect of the roller rotating by its own axis

In roller bearings, each roller element transfers along with the cage and rotates by its own axis. It should be noted here that in the numerical investigation, the rotating of the roller by its own axis is ignored. Its effect is tested by another configuration, as shown in Figure 4.7. The oil is injected to a straight box with seven in-line cylinders through a moving nozzle, which represents a simplified approach. The average density of the fluid in the box is monitored during the calculation with different cylinder rotating speeds. The oil

4. Two-phase flow in bearing cavity

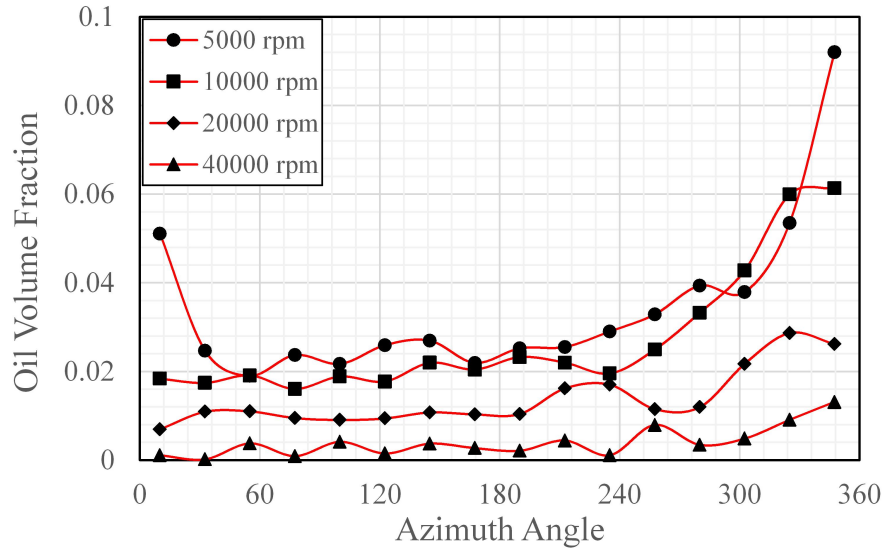


Figure 4.6: Oil volume fraction distributions around the circumference with different inner-ring rotational speeds

property is set as 931 kg/m^3 , 0.00486 kg/m-s and the nozzle moving speed is 10 m/s , with a 20 m/s injection velocity. As shown in Figure 4.8, it seems that the roller rotating by its own axis slightly changes the average oil volume fraction in the cavity. So that the treatment in the bearing model is somewhat acceptable.

4.3.2.2 Oil volume flow rate

There are two ways to change the oil volume flow rate with one single inlet nozzle, to change the oil inlet velocity or to change the inlet nozzle diameter. Figure 4.9 and 4.10 present the oil volume fraction as a function of the oil volume flow rate or the oil injection velocity with different nozzle diameters. The bearing rotating speed is 5000 rpm . From

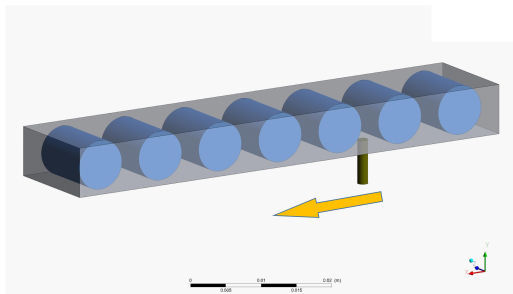


Figure 4.7: Simulation model for roller rotating validation

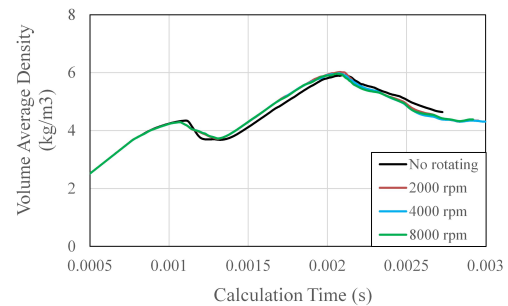


Figure 4.8: Average fluid density as a function of roller rotating speed

zero, oil volume fraction increases with the increasing of oil inlet velocity. After reaching the peak value, it decreases with the further increasing of oil inlet velocity. This could be explained that, at the first stage, the changing of oil inlet velocity changes the oil volume flow rate, which is the dominant element. The oil phase occupies larger region inside the bearing with the increasing of the oil flow rate. The effect of the impact between the injected oil and roller elements is not obvious.

Whereas, after that, the effect of further increasing oil flow rate drops and the oil inlet velocity is becoming the dominant element, which leads to strong fluid-structure impact. The maximum value of oil volume fraction reaches at the oil inlet velocity about 10 m/s for the under-race lubrication. At a lower inlet velocity, the oil is hard to enter the bearing cavity because of the hinder of the rolling elements. At a higher inlet velocity, the oil is fired straight to strick with the roller elements and flow outside the bearing cavity. Hence, the oil inlet velocity needs to be optimised in the design of the bearing lubrication devices.

With different combination of oil inlet velocity and nozzle diameter, the same oil volume flow rate could be obtained. Figure 4.11 shows oil volume fraction distributions around the circumference with the same oil volume flow rate. The bearing rotating speed is 5000 rpm.

With a higher inlet nozzle diameter, or a lower inlet velocity, a higher oil volume fraction level could be obtained, and the oil distribution are more uniform, as shown in Figure 4.12.

4.3.2.3 The oil inlet velocity

Figure 4.13 shows oil distribution around the circumference with different oil inlet velocity. The nozzle diameter is 1.5mm and the bearing rotating speed is 5000 rpm. Figure 4.14 shows turbulence kinetic energy distribution in bearing cavity, which demonstrates that the impact between the injected oil and rolling elements interacts strong at a higher inlet velocity. A higher oil inlet velocity could lead to a higher oil volume flow rate, while at the same time, the impact between the roller and injected oil is heightened. As mentioned above, there is an optimum oil inlet velocity for maximizing oil volume fraction, so that the best way to change the oil volume fraction is to change the nozzle diameter or nozzle number.

From Figure 4.10, it seems that for different nozzle diameters, their optimum inlet velocity to catch the maximum oil volume fraction is similar, close to the value of 10m/s. But if we want a lower oil retention in bearing cavity with sufficient lubrication, the inlet velocity 20m/s may be better.

4.3.2.4 Oil inlet diameter

For the same oil inlet velocity with different inlet nozzle diameters, a bigger diameter leads to a higher oil volume fraction in bearing cavity with the same oil-roller impacting intension. The distribution around the circumference becomes more uniform, as shown in Figure 4.15. The oil inlet velocity is 10 m/s and the roller rotating speed is 5000 rpm.

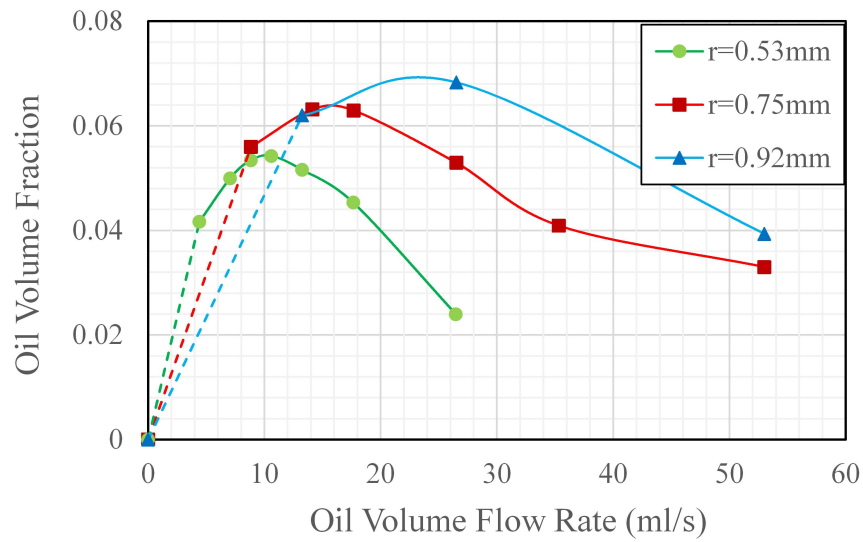


Figure 4.9: Oil volume fraction as a function of oil volume flow rate

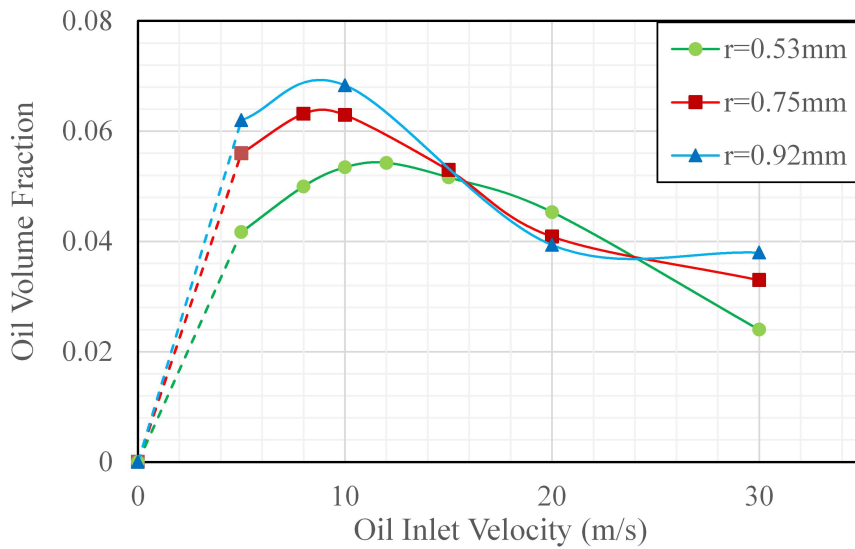


Figure 4.10: Oil volume fraction as a function of oil inlet vecocity

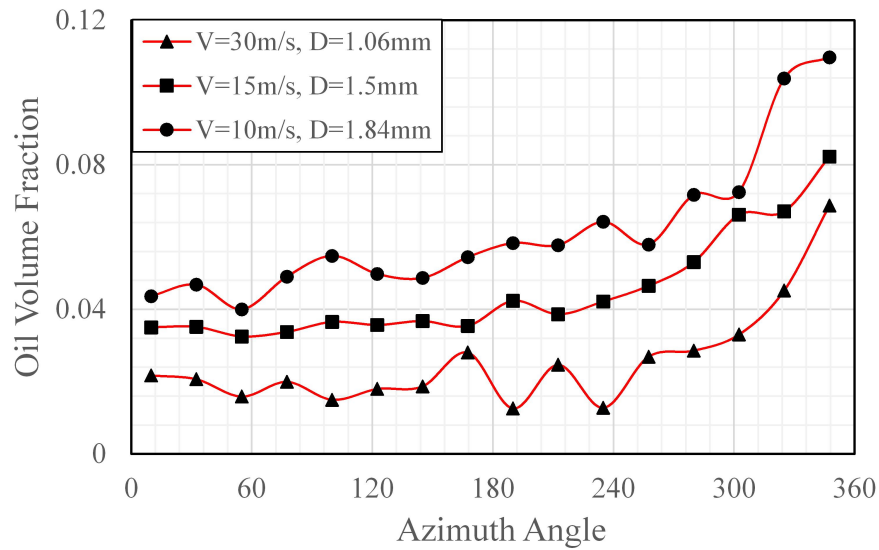


Figure 4.11: Oil volume fraction distributions with different oil inlet conditions

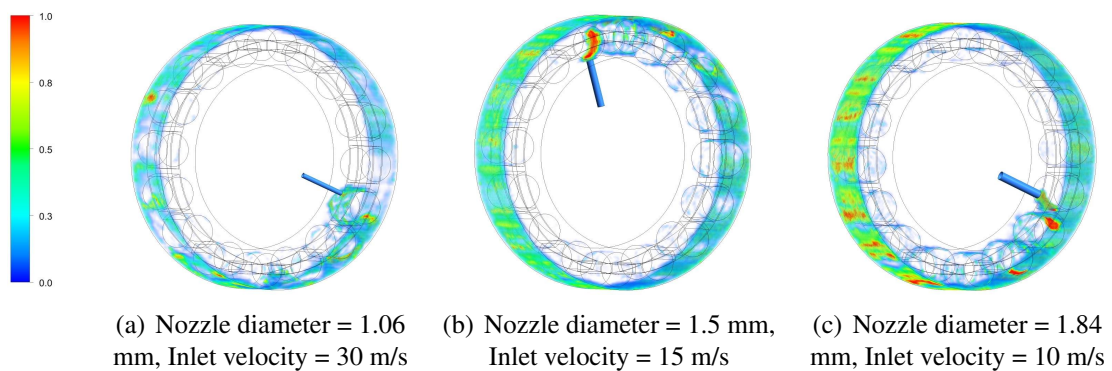


Figure 4.12: Oil volume fraction contours with different oil inlet conditions

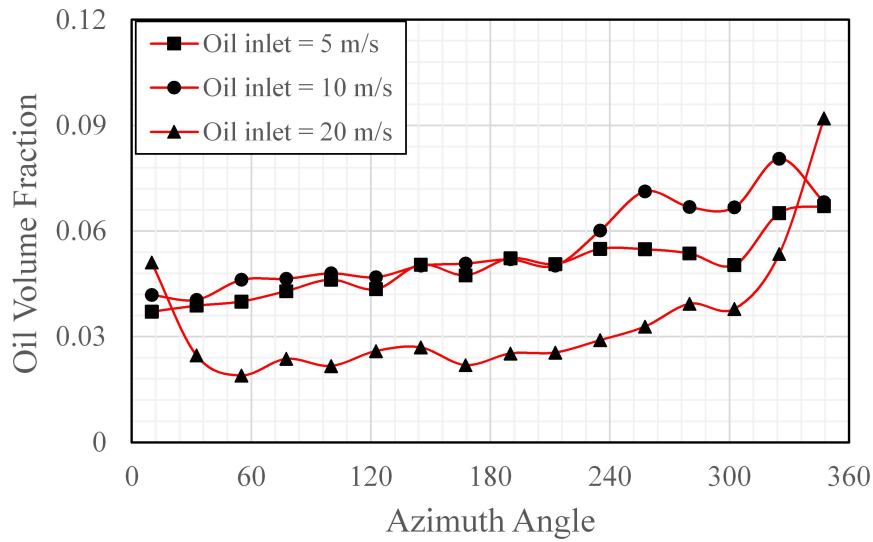


Figure 4.13: Oil volume fraction distributions with different oil inlet velocity

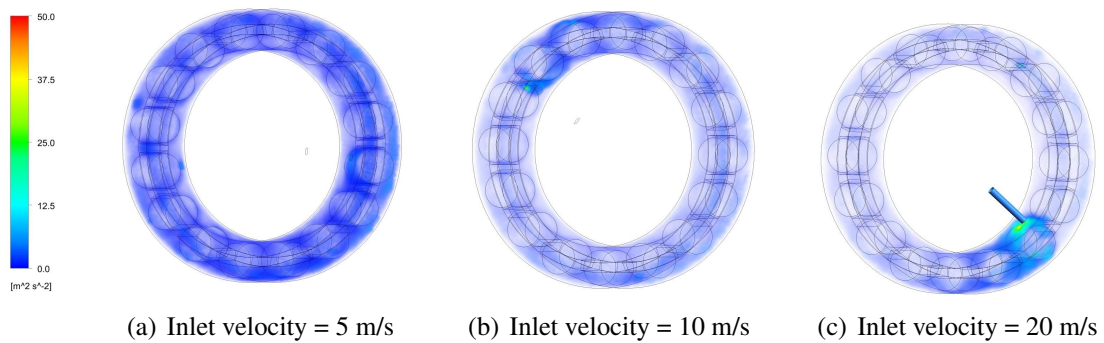


Figure 4.14: Turbulence kinetic energy distributions with different oil inlet velocity

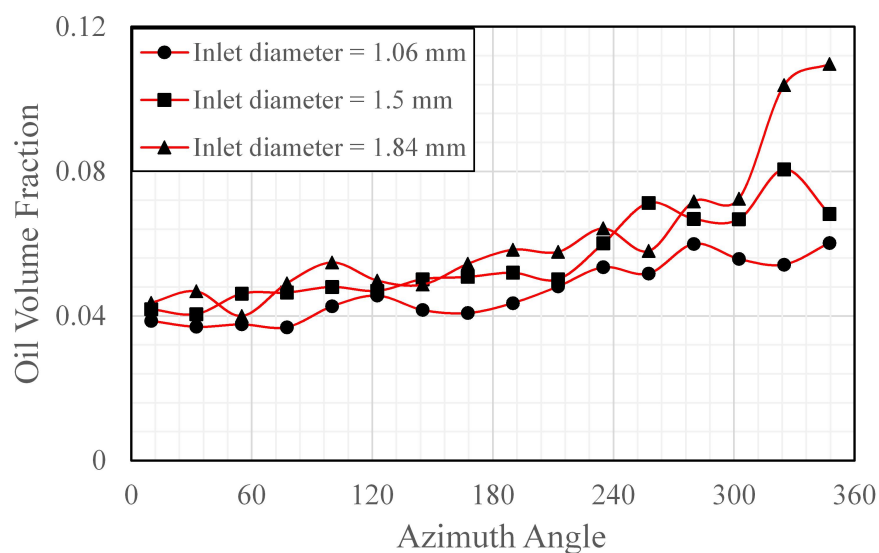


Figure 4.15: Oil volume fraction distributions with different oil inlet diameters

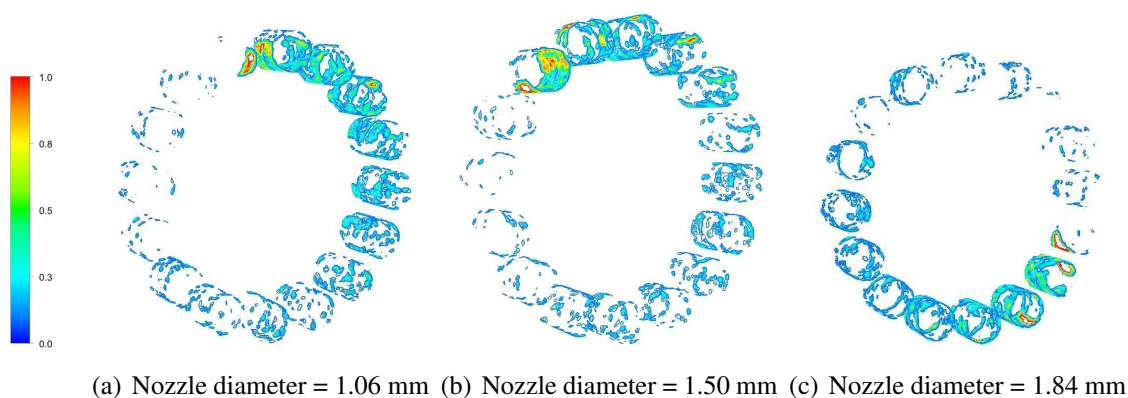


Figure 4.16: Oil volume fraction distributions around the rollers with different nozzle diameters

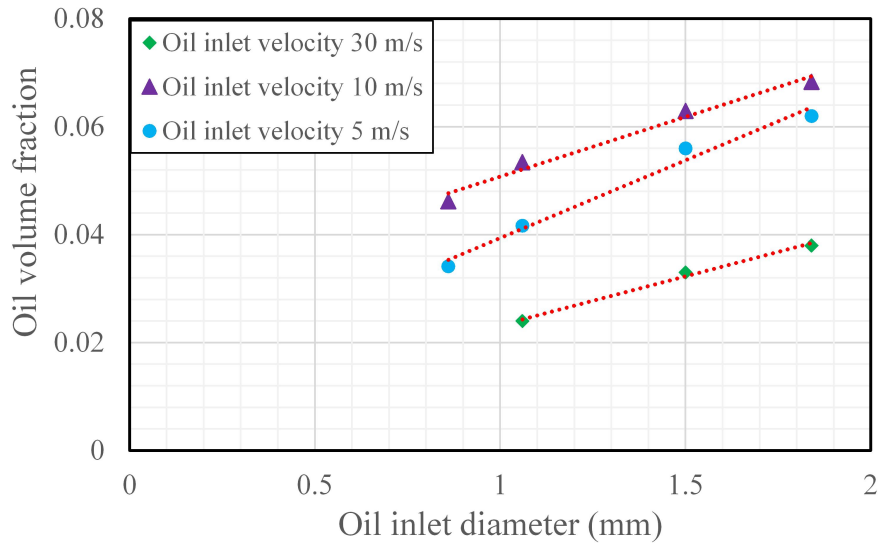


Figure 4.17: Oil volume fraction as a function of oil inlet diameter

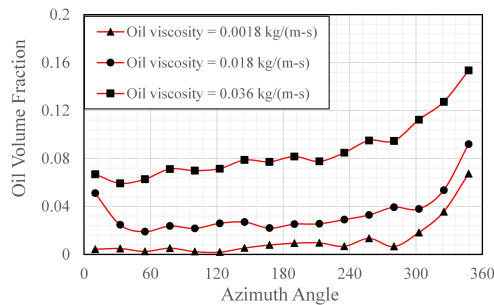


Figure 4.18: Oil volume fraction distribution with different oil viscosities

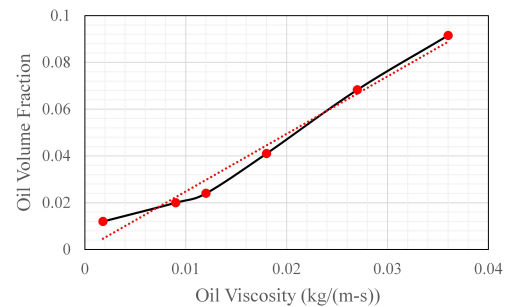


Figure 4.19: Oil volume fraction as a function of oil viscosity

As shown in Figure 4.17, the oil volume fraction inside the bearing cavity is proportional to the oil inlet diameter or the oil volume flow rate at the same inlet velocity.

4.3.2.5 Oil viscosity

In Parker' formula [PAR 84], all the tests and analysis were performed using MIL-L-23699 type lubricants, and it could not be used with lubricants whose properties vary significantly from MIL-L-23699.

The fluid viscosity is one of the most important properties for lubricant to determine its lubrication performance. It varies obviously with the lubricant type and the temperature, so that the effect of oil viscosity is studied numerically here.

It is illustrated in Figure 4.18 that the air/oil distribution becomes more uniform with a higher oil viscosity and the average oil volume fraction inside the bearing cavity is about

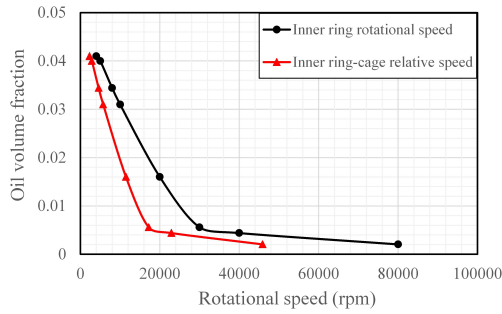


Figure 4.20: Oil volume fraction as a function of the bearing rotational speed

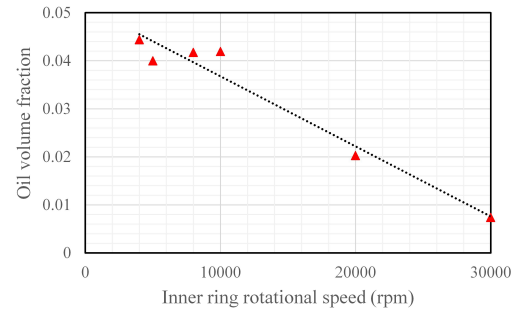


Figure 4.21: Oil volume fraction as a function of inner ring rotational speed

linear to the oil viscosity value (as shown in Figure 4.19).

4.3.2.6 Bearing rotational speed

Bearing rotational speed could be regarded as one of the most important parameters that change the oil volume fraction in bearing cavity. At the beginning, for the bearing with only the inner ring rotating, it has been mentioned that the oil volume fraction becomes lower when the bearing rotational speed increases. The oil distribution inside the bearing tends to be uniform. But the interaction between the air/oil flow and the bearing components becomes stronger with a higher inner ring rotating speed. In addition, it results in the increase of the flow velocity of the air/oil phase in the bearing [HU 14].

For the bearing with inner and outer rings rotating together, the rotation of the inner ring, the cage, and the outer ring, could change the oil volume fraction together at the same time 4.20. To highlight their individual effect, here these rotational parameters are studied separately. It should be noted that here the relationship different rotational speeds of different components may not follow their relationship in a real bearing.

Inner ring rotational speed

Figure 4.21 presents the simulated oil volume fraction with different inner ring rotational speed, with the same cage rotational speed (2132 rpm) and the fixed outer ring. The oil inlet diameter is 1.5 mm and oil injection velocity is 20 m/s. It can be seen that the oil phase occupies smaller region inside the bearing with higher inner ring rotational speed. This can be explained that with a higher inner ring rotational speed, the relative rotational speed between the under-race nozzle and the cage is increased and the interaction between the injected oil and the rolling elements becomes stronger. It seems that the average oil volume fraction is linear to the inner ring rotational speed.

Outer ring rotational speed

For inter-shaft supporting roller bearings, the outer ring rotates together with the inner ring, which may change the air/oil distribution inside the bearing cavity.

Figure 4.22 illustrates the calculated oil volume fraction with different outer ring rotational speed. In the simulation, the under-race oil nozzle rotates with the inner ring at

4. Two-phase flow in bearing cavity

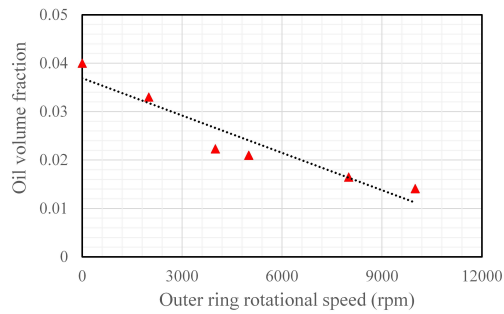


Figure 4.22: Oil volume fraction as a function of outer ring rotational speed

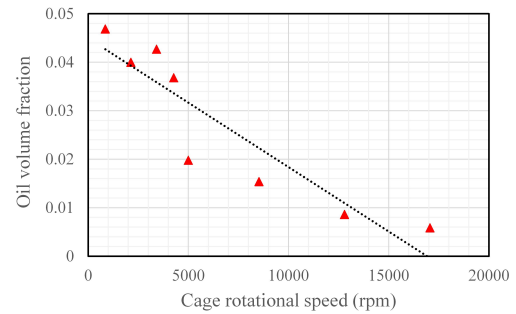


Figure 4.23: Oil volume fraction as a function of the cage rotational speed

a speed of 5000 rpm, and the cage rotational speed is fixed to 2132 rpm. The oil inlet diameter is 1.5 mm and oil injection velocity is 20 m/s. It could be found that the oil volume fraction decreases gradually with the increasing of the outer ring rotational speed. Since the rotational speed of the inner ring and the cage is constant, the changing could only be caused by the outer ring rotating. It could contribute to the exhausting of the oil phase that gathers near the outer ring, and leads to a linear decrease of the average oil volume fraction inside the bearing cavity.

Cage rotational speed

Except the inner and outer rings, the cage rotating may affect the oil distribution inside the bearing. Figure 4.23 presents the relationship between the oil volume fraction and the cage rotational speed. The inner ring rotational speed is fixed to 5000 rpm, with the inlet nozzle diameter 1.5 mm and oil inlet velocity 20 m/s. We know that the relative rotational speed between the inner ring and the cage determines the interaction between the oil and the rollers. But here the relative speed decreases at first to zero and then increases with the increasing of the cage speed. During this process, the oil volume fraction decreases continuously. This is because that the oil flows along the circumferential direction due to the agitation of the rolling elements. With a higher cage rotational speed, the oil flow velocity increases and it's easier for the oil to leave the bearing cavity. Additionally, the increasing centrifugal force contributes to this behavior, as well.

Inner ring-cage relative rotational speed

Compared with the rotational speed of the inner ring or the cage, the effect of the inner ring-cage relative rotational speed is a little confusing. For under-race lubrication, the relative rotational speed is beneficial for sharing the oil phase to the whole circumference of the bearing cavity. As shown in Figure 4.25, one calculation condition is that the inner and outer rings rotate together at the same rotational speed 5000 rpm so that the cage rotational speed is 5000 rpm and the relative inner ring-cage speed is zero. The other condition is that the inner ring rotates at the speed of 5000 rpm and the cage 2132 rpm. It could be found that without the relative speed, the oil gathers mainly near the region close to the nozzle and the other part of the bearing is poor-lubricated (Figure 4.26).

Figure 4.24 presents the calculated oil volume fraction inside the bearing cavity with

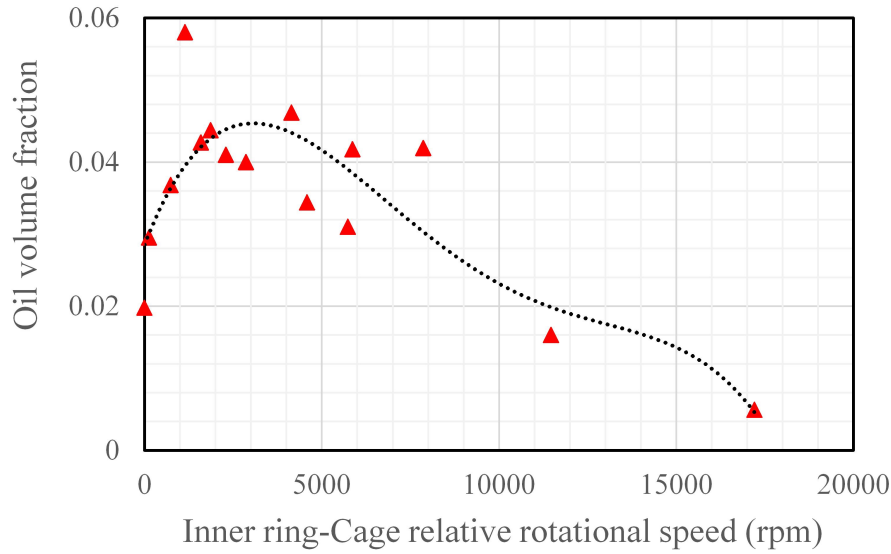


Figure 4.24: Oil volume fraction as a function of inner ring-cage relative speed

different inner ring-cage relative rotational speed. Here the outer ring is fixed. The oil volume fraction increases when the relative rotational speed increases from zero to about 2000 rpm. With the further increase of the relative speed, the oil volume fraction decreases. There is a special relative rotational speed value that can achieve a highest average oil volume fraction. This can be explained that at a small relative speed, the oil is hard to distribute to the whole circumference of the bearing cavity because of the blocking of the rollers near the nozzle. On the other hand, at a very high relative rotational speed, the interaction between the injected oil and the rolling elements is strong. The flow velocity of the oil phase is also high, being easier to leave the bearing cavity.

4.3.2.7 Number of nozzles

Figure 4.18 compares oil distribution between the single-nozzle inlet and dual-nozzle inlets, with the same oil volume flow rate and oil inlet velocity. The oil inlet velocity is 20 m/s and the bearing rotational speed is 5000 rpm. The oil volume flow rate is 2.1 L/min. The air/oil distribution becomes more homogeneous under the dual-nozzle inlets. The lowest volume fraction of the oil phase under both the single-nozzle inlet and the dual-nozzle inlets appears in the upstream side near the nozzle. Further, the average oil volume fraction is higher with the dual-nozzle inlets.

4.3.2.8 Injection deflection

Figure 4.29 illustrates oil volume fraction versus calculation time with different inlet nozzle deflection angle. The positive value means the injection direction is natural to the bearing rotating direction (only inner ring rotating), while the negative value means it's inverted (Figure 4.30). In the numerical simulation, the oil inlet velocity is 20 m/s. The

4. Two-phase flow in bearing cavity

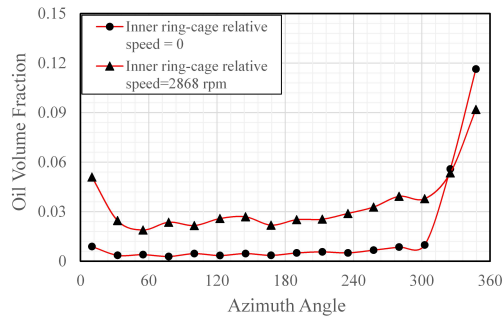


Figure 4.25: Oil volume fraction distribution with different relative rotational speeds

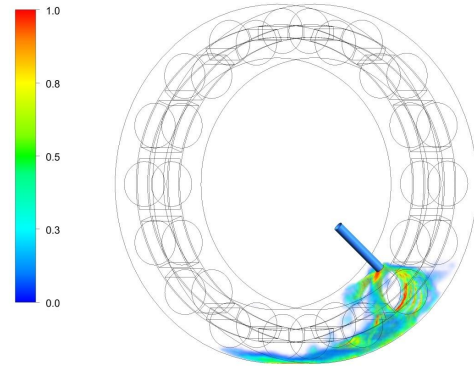


Figure 4.26: Oil volume fraction distribution with a zero relative rotational speed

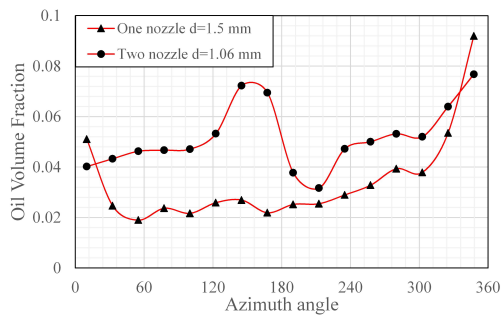


Figure 4.27: Comparison of oil volume fraction distribution with different inlet nozzle number

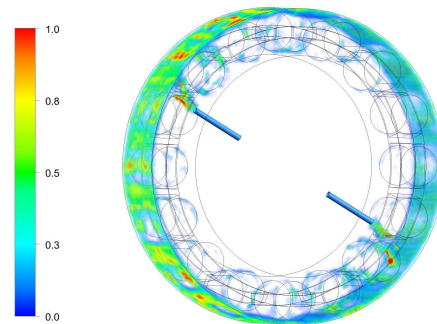


Figure 4.28: Oil volume fraction distribution with dual-nozzle inlets

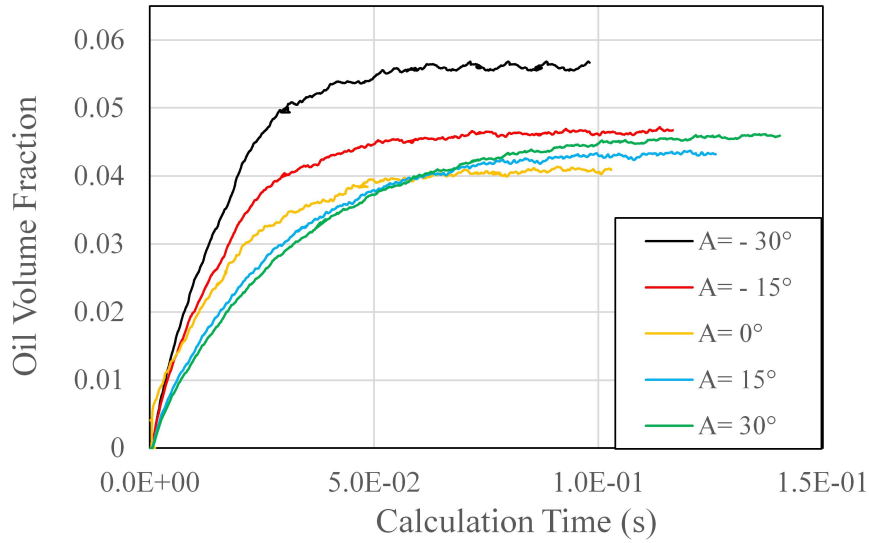


Figure 4.29: Oil volume fraction distributions with different oil inlet deflection angle

inner ring rotational speed is 5000 rpm and the cage rotational speed is 2132 m/s, with the relative speed of 2868 rpm. The deflection of the inlet nozzle decreases the relative vertical speed between the injected oil and the rollers, changing their relative tangential speed. The former has the similar effect with the changing oil inlet velocity while the latter has the same function as the inner ring-cage relative rotational speed, as shown in Figure 4.31.

With the conclusion for the oil inlet velocity, the decreasing of relative vertical speed could increase the oil volume fraction in the inlet velocity range around 20 m/s, which is corresponding with the results illustrated in Figure 4.29. For the natural deflection, the relative tangential speed increases (roller orbiting speed minus tangential component of oil inlet velocity), it is adverse to the increasing of oil volume fraction. While for the reverse deflection, the relative tangential speed is minused, increasing the oil volume fraction. It is in agreement with the conclusion about the relative rotational speed in the range bigger than 2000 rpm.

4.4 Comparion with existing hydraulic loss models

With all these numerical-based formulas in hand, total hydraulic losses of roller bearing, including the drag loss and the churning loss, could be predicted, and the results are compared with three existing hydraulic losses prediction models to verify its capability, e.g. Palmgren model, SKF model, and Parker model. Despite the existing hydraulic loss predicting models are empirical and the windage drag losses and churning losses are not distinguished, they are reliable and reasonable in view of its originating from a series of experimental tests.

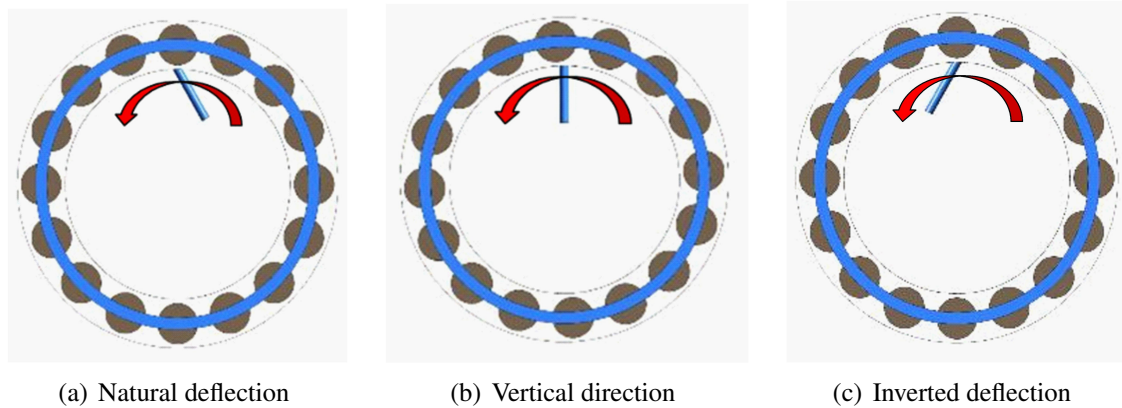


Figure 4.30: Configurations with different oil nozzle deflection direction

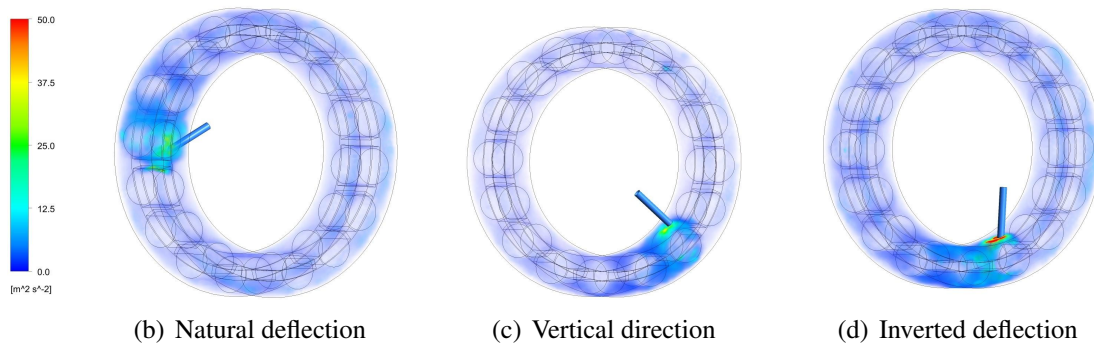


Figure 4.31: Turbulence kinetic energy distribution with different inlet nozzle deflection

4.4.1 Existing hydraulic losses prediction models

There have already been quite a few investigations of bearing friction torque. Palmgren presented a bearing model of friction torque and divided it into load-independent torque and load-dependent torque. SKF presented their model of bearing power loss by experimental fitting and gave some recommended values for the parameters in their equations. These models come from plenty of experimental studies and the results have been reduced to a simple model, in which the hydraulic losses or load-independent losses are accounted as a separated part.

Palmgren model

According to Palmgren, the bearing friction torque is divided into two parts which are load-independent friction torque and load-dependent friction torque. After converting the units of load-independent friction torque from kg/mm to N/m, the equation of load-independent friction torque of the bearing when lubricated by oil is shown in Equation 4.10.

$$\begin{cases} M_0 = 1.5572 \times 10^{-6} f_0 p d_m^3 & \text{if } \frac{\eta \omega}{p} < 2 \times 10^{-6} \\ M_0 = 9.81 \times 10^{-3} f_0 p d_m^3 \left(\frac{\eta \omega}{p} \right)^{\frac{2}{3}} & \text{if } \frac{\eta \omega}{p} \geq 2 \times 10^{-6} \end{cases} \quad (4.10)$$

Then the method of Palmgren was used by Harris but the values of parameters were updated.

$$\begin{cases} M_v = 10^{-10} f_0 (v_0 n)^{\frac{2}{3}} d_m^3 & v_0 n \geq 2000 \\ M_v = 160 \times 10^{-10} f_0 d_m^3 & v_0 n < 2000 \end{cases} \quad (4.11)$$

Where v_0 is the kinematic viscosity, cSt; n is the bearing rotating speed, rpm; d_m is the pitch diameter of the bearing, mm; f_0 is the factor depending on bearing design and lubricating method in Palmgren model (for cylindrical roller bearing = 2 – 3) and Harris model (for cylindrical roller bearing = 2.2 – 4).

SKF model

According to SKF, the friction torque of bearings can be divided into four parts. Load-independent friction torque can be divided into friction torque of seals and friction torque of drag losses, churning, splashing etc. Load-dependent friction torque can be divided into rolling friction torque and sliding friction torque. And the hydraulic losses (named drag loss by SKF) could be calculated as following.

$$M_{drag} = 4 \times 10^{-3} V_M K_{roll} C_w B d_m^4 n^2 + 1.093 \times 10^{-10} n^2 d_m^3 \left(\frac{n d_m^2 f_t}{v} \right)^{-1.379} R_s \quad (4.12)$$

$$K_{roll} = \frac{K_L K_Z (d + D)}{D - d} 10^{-12} \quad (4.13)$$

$$C_w = 2.789 \times 10^{-10} l_D^3 - 2.786 \times 10^{-4} l_D^2 + 0.0195 l_D + 0.6439 \quad (4.14)$$

$$l_D = 5 \frac{K_L B}{d_m} \quad (4.15)$$

$$f_t = \begin{cases} \sin(0.5t) & \text{when } 0 \leq t \leq \pi \\ 1 & \text{when } \pi < t < 2\pi \end{cases} \quad (4.16)$$

$$R_s = 0.36 d_m^2 (t - \sin t) f_A \quad (4.17)$$

$$t = 2 \cos^{-1} \left(\frac{0.6 d_m - H}{0.6 d_m} \right) \quad \text{When } H \geq d_m, \text{ use } H = d_m \quad (4.18)$$

$$f_A = 0.05 \frac{K_Z (D + d)}{D - d} \quad (4.19)$$

Where H is the oil level for the bearing with oil bath lubrication, while for oil jet lubrication, H is at half of the diameter of the lowest rolling element and M_{drag} should be multiplied by a factor of two.

It should be emphasized that in the two models above, the effect of the oil volume flow rate is not considered and the bearing is regared as full-lubricated. Theoretically,

with more oil flow rate, the oil phase volume fraction inside the bearing cavity is higher, with more windage drag and churning losses.

Parker model

Parker deduced an equation to calculate the oil percent volume in bearing cavity based on a range of experimental tests. The computer program SHABERTH was used to calculate the thermal performance of three selected ball bearings for the comparison [NIC 17]. The oil volume fraction was derived as a function of lubricant flow rate, shaft speed, and bearing pitch diameter.

$$XCAV = 10.0 \times 10^6 \frac{W^{0.37}}{nd^{1.7}} \quad (4.20)$$

Where W is the inlet oil flow, cm^3/min , n is the inner shaft speed, rpm, and d is the bearing pitch diameter, mm. Depending on the oil/air volume ratio inside the bearing cavity, the effective density and viscosity of the equivalent fluid could therefore be expressed as

$$\begin{aligned} \rho_{eff} &= (\rho_{oil} \times oilvolume + \rho_{air} \times airvolume) / totalvolume \\ &\cong \rho_{oil} \times \frac{oilvolume}{totalvolume} = \rho_{oil} \times XCAV \end{aligned}$$

$$\begin{aligned} \mu_{eff} &= (\mu_{oil} \times oilvolume + \mu_{air} \times airvolume) / totalvolume \\ &\cong \mu_{oil} \times \frac{oilvolume}{totalvolume} = \mu_{oil} \times XCAV \end{aligned}$$

In the program SHABERTH, all hydraulic losses are named drag loss and accounted by the model of one isolated element in an uniform fluid.

$$F_r = \frac{1}{2} C_d \rho V^2 A \quad (4.21)$$

Where F_r is the drag force, N , ρ the mass density of the fluid, kg/m^3 , V the velocity at which the body is traveling, m/s , and A the frontal area of the body to the flow direction, m^2 . Here the drag coefficient C_d plays a dominant part in the drag force calculation, as a function of the Reynolds number, both for a smooth cylinder and a smooth sphere, as shown in Figure 4.32. Since all the analysis are performed using MIL-L-23699 type lubricants, the Parker model should not be used with lubricants whose properties vary significantly from MIL-L-23699.

4.4.2 Calculation results

The cylindrical roller bearing specification used for the analysis is the same as the bearing employed in the oil/air two phase flow investigation. The lubricant oil used here is

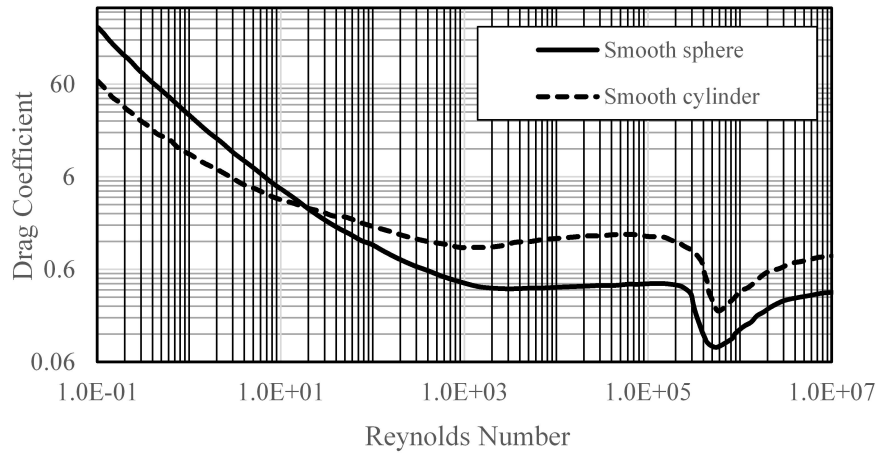


Figure 4.32: Drag coefficient of the isolated sphere and cylinder

respected to the MIL-L-23699 type lubricant oil with a popular trade name Mobile Jet 2. Respectively, the lubricant oil density is 976 kg/m^3 and the viscosity is 0.018 kg/(m.s) . The oil is supplied through the inner ring and the oil injection velocity is 20 m/s.

The three existing models (Palmgren, SKF, Parker) were built according to a series of experimental tests for bearing with inner ring rotating, having a certain accuracy for its specific operating conditions. For example, the SKF model is developed for bearings lubricated by the oil bath method, partially submerged or, in special situations, completely submerged. Despite the effect of oil volume flow rate is not considered, it could be assumed that the bearing is full-lubricated or, excessive-lubricated.

The effect of bearing rotating speed

The bearing rotating speed has a very significant effect on the roller bearing power loss so that drag and churning losses changing with the rotating speed are analyzed first. Figure 4.33 illustrates the calculation results of different drag and churning losses prediction models. The oil volume flow rate is set as $2000 \text{ cm}^3/\text{min}$ and the inner ring rotating speed ranges from 2000 to 80000 rpm. It could be found that the SKF model gets the largest predicted hydraulic losses and Palmgren model is the lowest for most inner ring rotating speeds. This results correspond with the fact that the bearing in the SKF model is assumed to be full-lubricated. Noting when the bearing rotating speed reaches up to 80000 rpm, the oil flow rate $2000 \text{ cm}^3/\text{min}$ is not enough for lubricating. Thus the SKF model has the largest predicted value. In addition, the numerical model results match well with the Parker model, which is proposed from the comparison of bearing thermal performance over a range of test conditions. This demonstrates that the numerical model is reliable and valuable in terms of the total drag and churning losses prediction.

If we increase the oil volume flow rate up to $3000 \text{ cm}^3/\text{min}$, as shown in Figure 4.34, only the results of the Parker model and numerical model could be changed, which take this factor into account. For the bearing rotating speed from 2000 rpm to 80000 rpm, results of the SKF model, Parker model and numerical model are similar, and larger than that

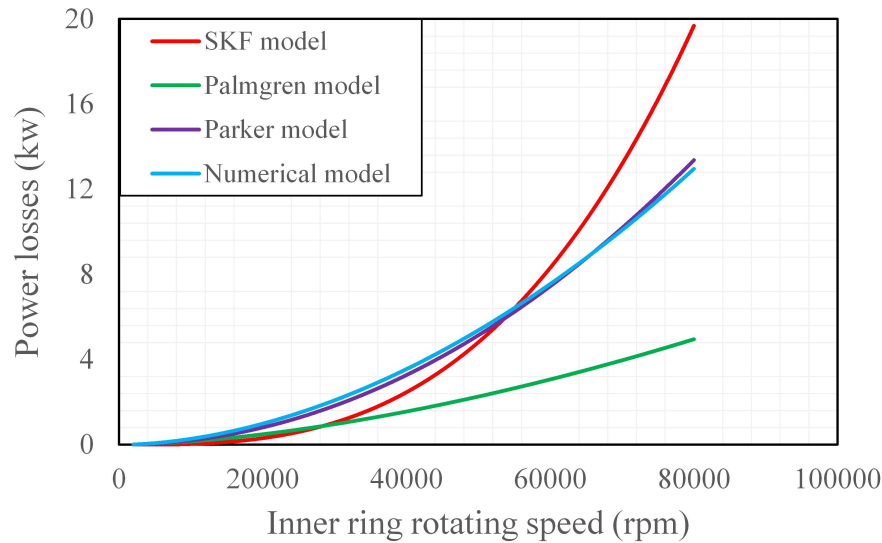


Figure 4.33: Hydraulic losses from different models at different inner ring rotating speed (Oil flow rate 2000 cm³/min)

of the Palmgren model. In this condition, the bearing is regarded as sufficient-lubricated. If the oil volume flow rate is increased further to 4000 cm³/min, as shown in Figure 4.35, the bearing is over-lubricated and the result of the numerical model is obviously larger than the other three models. It means that larger amounts of lubricant oil flow can definitely lead to larger heat generation.

The effect of the oil flow rate

Now that a large amount of oil volume flow leads to a higher power loss and too small oil flow may cause a lubrication failure, a sufficient assessment of the lubricated bearing is of particular importance. Figure 4.36 shows results of these four models with a fixed bearing rotating speed 72200 rpm, as a function of the oil volume flow rate. The SKF model and Palmgren model are constant which are regarded as full-lubricated by default. The results of the Parker model and the numerical model are close and increase obviously with the increase of the oil flow rate.

Based on the above analysis, it is demonstrated that the numerical model for drag and churning losses estimation in roller bearings is reliable and reasonable. The predicted result of the SKF model is usually a little too high while the Palmgren model is always too low. For the Parker model, its result is close to the numerical one, but it can't distinguish the drag and churning effects, and it can't be used directly for the counter-rotating roller bearing with under-race lubrication.

As shown in the Figure 4.37, the total hydraulic losses, caused by the roller rotating and translating in the fluid environment, are contributed by three parts, drag loss, churning loss on the cylindrical surface, and churning loss on the free end. The churning loss on the cylindrical surface takes the most proportion of the total hydraulic losses and the other two parts only take a small percentage. This is disagreed with the previous research which

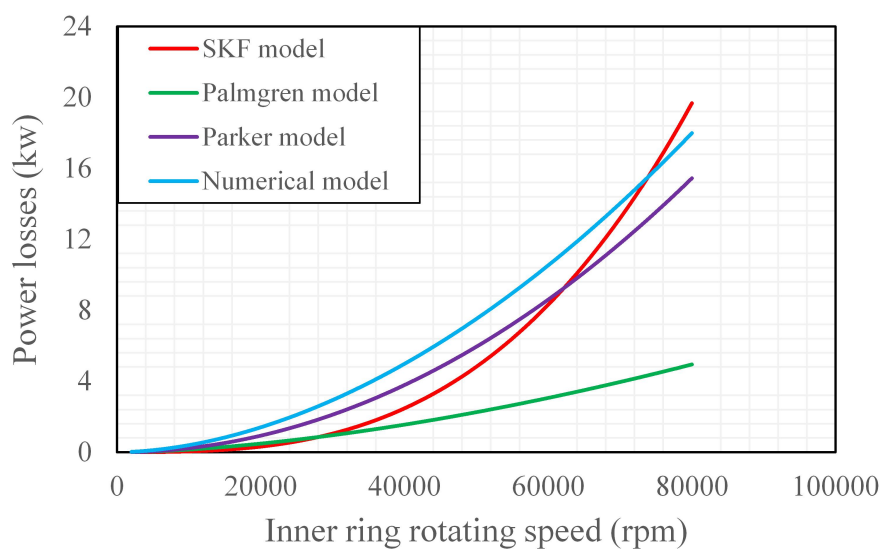


Figure 4.34: Hydraulic losses from different models at different inner ring rotating speed (Oil flow rate $3000 \text{ cm}^3/\text{min}$)

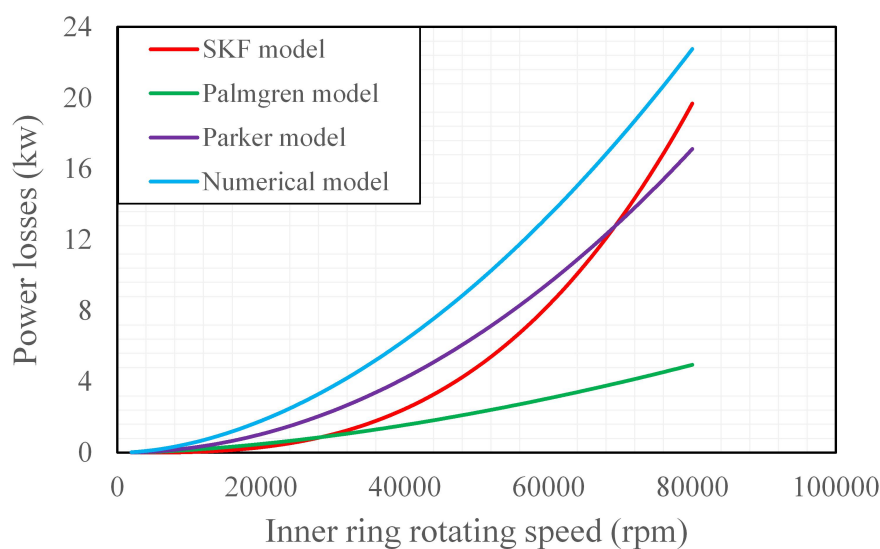


Figure 4.35: Hydraulic losses from different models at different inner ring rotating speed (Oil flow rate $4000 \text{ cm}^3/\text{min}$)

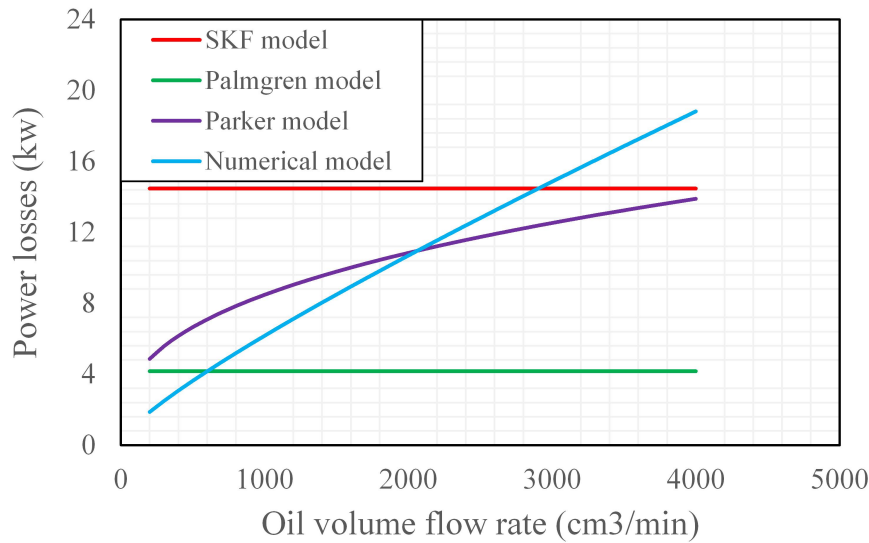


Figure 4.36: Hydraulic losses from different models at different oil flow rate (Inner ring rotating 72200 rpm)

named the total hydraulic losses as drag loss.

4.5 Conclusion

In this chapter, the numerical CLS-VOF model is employed to simulate the oil/air two-phase flow inside high speed roller bearings with under-race lubrication. The oil distribution along the circumference between the inner and outer rings is studied with different lubricating schemes and operating conditions. The effects of rotational speeds of different bearing components are investigated in detail. It is found that:

(1) The oil phase distribution in the bearing is not uniform. It varies with the bearing rotational speed, oil volume flow rate, oil viscosity, *etc.* There is an optimum oil injection velocity to catch a high level of oil volume fraction inside the bearing.

(2) The average oil volume fraction inside the bearing is proportional to the oil viscosity. With a specified oil injection velocity, it is linear to the oil inlet diameter.

(3) Rotational speeds of all bearing components could change the oil distribution inside the bearing, e.g. the inner ring, the cage, and the outer ring, including the inner ring-cage relative rotational speed. The results can be used for the precise lubrication design to optimize the oil distribution inside the bearing.

(4) Based on the numerical simulation results, a formula to predict the average oil volume fraction in roller bearings with under-race lubrication could be obtained (For oil

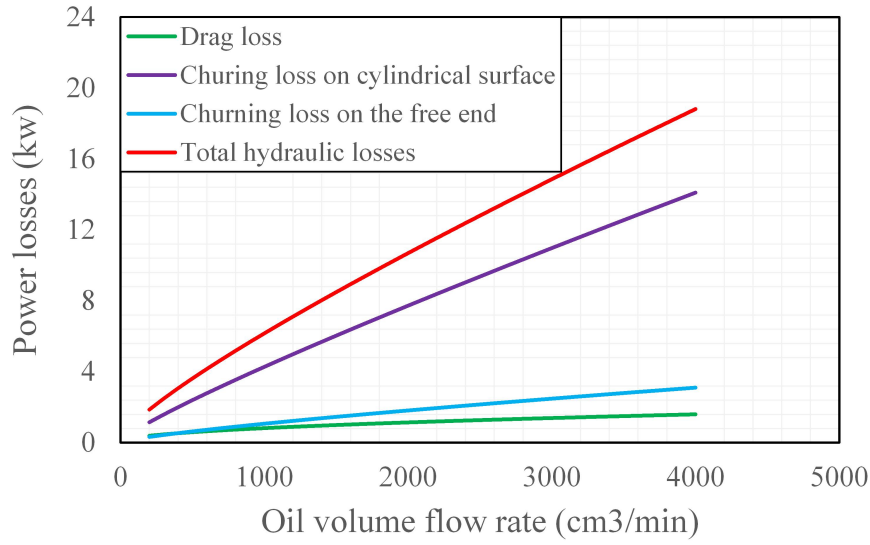


Figure 4.37: Partial of hydraulic losses at different oil flow rate (Inner ring rotating 72200 rpm)

injection velocity 20 m/s). Noting that the bearing dimension is not analyzed in this article, its relationship follows the Parker's model [PAR 84].

$$XCAV = 2.58 \times 10^4 \times \frac{(\omega_i - 0.1972\omega_{re})^{1.313} W^{0.5} \mu}{(\omega_i + \omega_o)(\omega_i + 1.768\omega_c) d_m^{1.7}} \quad (4.22)$$

Where ω_i , ω_o , ω_c are the inner ring, outer ring and the cage rotational speed, respectively, *rpm*. ω_{re} is the inner ring-cage relative speed, *rpm*. W is the oil volum flow, cm^3/min . μ is the oil dynamic viscosity, *Pa.s*. And d_m is the bearing pitch diameter, *mm*.

Finally, it should be mentioned that the results of the numerical study are sensitive to the simulated geometry and boundary conditions, thus it could only provide a gross approximation, with the absence of reliable experimental validation.

General conclusions and perspectives

General conclusion

In this thesis, the numerical method is employed to explore both windage drag and churning losses in high speed rolling element bearings. The drag coefficient and churning moments on the special finite circular cylinder with two free ends in roller bearings are investigated using the CFD approach. Additionally, the oil/air two-phase flow inside the bearing cavity is studied numerically to quantify the oil phase distribution in the bearing circumference.

In Chapter 2, the flow around one finite circular cylinder with two free ends in open space is discussed carefully. Despite relative simple geometry, scant attention has been attracted so far to demonstrate its flow pattern and turbulent structure varying with the aspect ratio and Reynolds number. The results show that the drag coefficient decreases dramatically in comparison to the two-dimensional model and the horseshoe vortex around the mounted cylinder with one free end disappears. Instead, a pair of stationary recirculating eddies behind the cylinder is found in the axis direction at low Reynolds number. With the increasing of Reynolds number, four spiral vortices are formed by the interaction of the two three-dimensional separating flows from two free ends and the wake formed by the cylindrical surface. The separated flow recirculates to the backside of the cylinder and increases its local pressure. Additionally, an intersection zone and a backflow is found close to the end surface, caused by the up-wash flow from the sharp leading edge of the cylinder. The work in Chapter 2 builds a foundation for the further analysis of windage drag and churning losses investigation in roller bearings.

A detailed numerical implementation of windage drag coefficient and churning moments is described and validated in Chapter 3. For the windage drag coefficient, it is previously accounted with a two-dimensional infinite cylinder model. Whereas the roller in bearings is rotating finite-length, which could be interacted by its two free ends, surrounding rings and other rollers. Based on the CFD method developed in Chapter 2, the configuration with several in-line cylinders sandwiched by two flat walls is analyzed, which represent a simplified approach. Finally, a new relationship between the drag coefficient and the Reynolds number suitable for circular cylinders in roller bearings is proposed.

For the churning loss in roller bearings, there are few approaches used directly for churning loss estimation, which could only provide a rather gross approximation. In one-phase environment, the churning moments on the cylinder are quantified considering var-

ious factors, e.g. operating conditions, roller geometry parameters, and fluid properties. It is also demonstrated that the roller orbital speed, the presence of adjacent rollers, and the rings have a significant impact on the churning moments. In conclusion, a formulation is proposed for churning losses prediction in cylindrical roller bearings. This is of particular interest for high-speed applications where drag and churning losses may represent up to 50% of the total power dissipated.

More important, there is an assumption used in Chapter 3 that the oil/air two-phase flow inside the bearing cavity is replaced by an equivalent fluid whereas the oil volume fraction is unknown. In Chapter 4, the CLS-VOF model is used to study the oil flow inside the bearing with under-race lubrication. The oil distribution around the circumference between the inner and outer rings is studied with different lubricating schemes and operating conditions. Rotational speeds of all the bearing components are studied particularly and the results demonstrate that not only the inner ring-cage relative rotational speed, but the cage speed itself could change the oil distribution. A formula to predict the oil volume fraction inside the bearing cavity is finally proposed. The results could be used for the precise lubrication design to optimize the oil distribution inside the bearing.

Perspectives

After this thesis, the future work could be considered in these aspects:

- Experiment validations

Now that the numerical methods for the simulation of flow around several in-line circular cylinders sandwiched by two flat walls, it would be an important step to validate them against experimental tests. The drag force and churning moments on the cylinder should be measured with different fluids and flow conditions to validate the relationship between the drag coefficient and Reynolds number summarized in this thesis, and the formulation for churning moments prediction.

For the oil/air two phase flow inside the bearing, an effective visualization technique is needed to display the oil distribution around the bearing circumference.

- Further numerical simulations

In the thesis the drag force and churning moments are numerically simulated in one-phase environment. The truth is that high speed roller bearings never are completely flooded with lubricant, and seldom are more than 15 to 20 percent full of oil within the bearing for very high speed operation. Motion of the bearing components tends to induce an oil/air two phase flow, which is more complicated. To improve the accuracy of the windage drag and churning losses prediction model, a further numerical simulations are needed.

Besides, for the oil/air two phase flow inside the bearing cavity, it has been proven that the results are sensitive to the simulated geometry and boundary conditions, and

the oil flow are traced with the VOF model. We believe that there is still room to optimise the numerical techniques in this domain, or try another numerical method, like the SPH method.

- The effect of the cage

In Chapter 3, the effect of the cage is ignored to highlight the effects of two free ends, the rings, and the adjacent rollers, regarding that the cage has been demonstrated experimentally that its effect is of second order on the flow. In the next step, the cage should be accounted in the numerical investigation and experimental test.

Bibliography

- [ABR 70] ABRAHAM F. F.
Functional dependence of drag coefficient of a sphere on Reynolds number. *The Physics of Fluids*, vol. 13, n° 8, 1970, p. 2194–2195, AIP.
- [ADE 14] ADENIYI A. A., MORVAN H. P., SIMMONS K. A.
A transient CFD simulation of the flow in a test rig of an aeroengine bearing chamber. *ASME Turbo Expo 2014: Turbine Technical Conference and Exposition* American Society of Mechanical Engineers, 2014, p. V05CT16A030–V05CT16A030.
- [ADE 15] ADENIYI A. A., MORVAN H. P., SIMMONS K. A.
A multiphase computational study of oil-air flow within the bearing sector of aeroengines. *ASME Turbo Expo 2015: Turbine Technical Conference and Exposition* American Society of Mechanical Engineers, 2015, p. V05CT15A024–V05CT15A024.
- [ADE 17] ADENIYI A. A., MORVAN H., SIMMONS K.
A computational fluid dynamics simulation of oil–air flow between the cage and inner race of an aero-engine bearing. *Journal of Engineering for Gas Turbines and Power*, vol. 139, n° 1, 2017, p. 012506, American Society of Mechanical Engineers.
- [APP 15] APPELQUIST E., SCHLATTER P., ALFREDSSON P. H., LINGWOOD R. J.
Investigation of the global instability of the rotating-disk boundary layer. *Procedia IUTAM*, vol. 14, 2015, p. 321–328.
- [BAI 96] BAI C., GOSMAN A.
Mathematical modelling of wall films formed by impinging sprays. rapport, 1996, SAE Technical Paper.
- [BAK 85] BAKER C.
The position of points of maximum and minimum shear stress upstream of cylinders mounted normal to flat plates. *Journal of wind engineering and industrial aerodynamics*, vol. 18, n° 3, 1985, p. 263–274, Elsevier.
- [BLA 15] BLAZEK J.
Computational fluid dynamics: principles and applications. Butterworth-Heinemann, 2015.

- [CAV 05] CAVALLARO G., NELIAS D., BON F.
Analysis of high-speed intershaft cylindrical roller bearing with flexible rings. *Tribology transactions*, vol. 48, n° 2, 2005, p. 154–164, Taylor & Francis.
- [CHU 10a] CHUESHOV I., LASIECKA I.
Von Karman Models with Rotational Forces. *Springer Monographs in Mathematics*, p. 129–194 Springer New York, 2010.
- [CHU 10b] CHUNG T.
Computational fluid dynamics. Cambridge university press, 2010.
- [CON 15] CONCLI F., GORLA C., DELLA TORRE A., MONTENEGRO G.
Churning power losses of ordinary gears: a new approach based on the internal fluid dynamics simulations. *Lubrication Science*, vol. 27, n° 5, 2015, p. 313–326, Wiley Online Library.
- [FER 93] FERREIRA C., RICHTER E.
Detailed design of a 250-kW switched reluctance starter/generator for an aircraft engine. rapport, 1993, SAE Technical Paper.
- [FER 15] FERNANDES C. M., MARQUES P. M., MARTINS R. C., SEABRA J. H.
Gearbox power loss. Part I: Losses in rolling bearings. *Tribology International*, vol. 88, 2015, p. 298–308.
- [FLO 05] FLOUROS M.
The impact of oil and sealing air flow, chamber pressure, rotor speed, and axial load on the power consumption in an aeroengine bearing chamber. *Journal of engineering for gas turbines and power*, vol. 127, n° 1, 2005, p. 182–186, American Society of Mechanical Engineers.
- [FLO 06] FLOUROS M.
Reduction of power losses in bearing chambers using porous screens surrounding a ball bearing. *Journal of Engineering for Gas Turbines and Power*, vol. 128, n° 1, 2006, p. 178–182, American Society of Mechanical Engineers.
- [FLU 11] FLUENT A.
Ansys fluent theory guide. *ANSYS Inc., USA*, vol. 15317, 2011, p. 724–746.
- [FRI 70] FRITZ R.
The effects of an annular fluid on the vibrations of a long rotor, part 1: Theory. *Journal of Basic Engineering*, vol. 92, n° 4, 1970, p. 923–929, American Society of Mechanical Engineers.
- [FRÖ 04] FRÖHLICH J., RODI W.
LES of the flow around a circular cylinder of finite height. *International journal of heat and fluid flow*, vol. 25, n° 3, 2004, p. 537–548, Elsevier.

- [GAO 18] GAO W., NELIAS D., BOISSON N., LYU Y.
Model formulation of churning losses in cylindrical roller bearings based on numerical simulation. *Tribology International*, , 2018, Elsevier.
- [GLO 11] GLOECKNER P., DULLENKOPF K., FLOUROS M.
Direct outer ring cooling of a high speed jet engine mainshaft ball bearing: experimental investigation results. *Journal of Engineering for Gas Turbines and Power*, vol. 133, n° 6, 2011, p. 062503, American Society of Mechanical Engineers.
- [GOH 14] GOHARZADEH A., MOLKI A.
Measurement of fluid velocity development behind a circular cylinder using particle image velocimetry (PIV). *European Journal of Physics*, vol. 36, n° 1, 2014, p. 015001, IOP Publishing.
- [GUH 93] GUHA S.
Analysis of dynamic characteristics of hydrodynamic journal bearings with isotropic roughness effects. *Wear*, vol. 167, n° 2, 1993, p. 173–179, Elsevier.
- [GUP 79] GUPTA P.
Dynamics of rolling-element bearing—Part I: Cylindrical roller bearing analysis. *Journal of lubrication technology*, vol. 101, n° 3, 1979, p. 293–302, American Society of Mechanical Engineers.
- [GUP 12] GUPTA P. K.
Advanced dynamics of rolling elements. Springer Science & Business Media, 2012.
- [HAR 73] HARRIS T., MINDEL M.
Rolling element bearing dynamics. *Wear*, vol. 23, n° 3, 1973, p. 311–337, Elsevier.
- [HAR 06] HARRIS T. A., KOTZALAS M. N.
Advanced concepts of bearing technology: rolling bearing analysis. CRC Press, 2006.
- [HAR 10] HARICHANDAN A. B., ROY A.
Numerical investigation of low Reynolds number flow past two and three circular cylinders using unstructured grid CFR scheme. *International Journal of heat and fluid flow*, vol. 31, n° 2, 2010, p. 154–171, Elsevier.
- [HES 03] HESELTINE J. L.
Flow around a circular cylinder with a free end. Thèse de doctorat, 2003.
- [HIL 11] HILL M. J., KUNZ R. F., MEDVITZ R. B., HANDSCHUH R. F., LONG L. N., NOACK R. W., MORRIS P. J.
CFD analysis of gear windage losses: validation and parametric aerodynamic studies. *Journal of Fluids Engineering*, vol. 133, n° 3, 2011, p. 031103, American Society of Mechanical Engineers.

- [HIR 81] HIRT C. W., NICHOLS B. D.
Volume of fluid (VOF) method for the dynamics of free boundaries. *Journal of computational physics*, vol. 39, n° 1, 1981, p. 201–225, Elsevier.
- [HON 16] HONG S.-W., TONG V.-C.
Rolling-element bearing modeling: A review. *International Journal of Precision Engineering and Manufacturing*, vol. 17, 2016, p. 1729–1749.
- [HOU 09] HOUPERT L.
CAGEDYN: a contribution to roller bearing dynamic calculations part I: basic tribology concepts. *Tribology Transactions*, vol. 53, n° 1, 2009, p. 1–9, Taylor & Francis.
- [HU 13] HU J.-P., LIU Z.-X., LV Y.-G., ZHAO J.-Y.
Comparison of simulation and measurement for film thickness in bearing chamber. *Aeronautical Computing Technique*, vol. 2, 2013, p. 019.
- [HU 14] HU J., WU W., WU M., YUAN S.
Numerical investigation of the air–oil two-phase flow inside an oil-jet lubricated ball bearing. *International Journal of Heat and Mass Transfer*, vol. 68, 2014, p. 85–93, Elsevier.
- [HUT 17] HUTCHINGS I., SHIPWAY P.
Tribology: friction and wear of engineering materials. Butterworth-Heinemann, 2017.
- [JAV 14] JAVADI K., KINAI F.
On the turbulent flow structures over a short finite cylinder: numerical investigation. *International Conference on Heat Transfer and Fluid Flow (HTFF), Prague, Czech Republic, Aug, 2014*, p. 11–12.
- [KAJ 16] KAJISHIMA T., TAIRA K.
Computational Fluid Dynamics. Springer, 2016.
- [KAW 84a] KAWAMURA T., HIWADA M., HIBINO T., MABUCHI I., KUMADA M.
Flow around a finite circular cylinder on a flat plate: Cylinder height greater than turbulent boundary layer thickness. *Bulletin of JSME*, vol. 27, n° 232, 1984, p. 2142–2151, The Japan Society of Mechanical Engineers.
- [KAW 84b] KAWAMURA T., KUWAHARA K.
Computation of high Reynolds number flow around a circular cylinder with surface roughness. *22nd Aerospace Sciences Meeting*, 1984, p. 340.
- [KIA 16] KIANI F., JAVADI K.
Investigation of turbulent flow past a flagged short finite circular cylinder. *Journal of Turbulence*, vol. 17, 2016, p. 400–419.

- [KIM 15] KIM S., WILSON P. A., CHEN Z.-M.
Large-eddy simulation of the turbulent near wake behind a circular cylinder: Reynolds number effect. *Applied Ocean Research*, vol. 49, 2015, p. 1–8, Elsevier.
- [KLE 05] KLEEFSMAN K., FEKKEN G., VELDMAN A., IWANOWSKI B., BUCHNER B.
A volume-of-fluid based simulation method for wave impact problems. *Journal of computational physics*, vol. 206, n° 1, 2005, p. 363–393, Elsevier.
- [KOL 11] KOLEV N. I.
Numerical solution methods for multi-phase flow problems. *Multiphase Flow Dynamics 1*, p. 497–602 Springer, 2011.
- [KRA 11] KRAJNOVIĆ S.
Flow around a tall finite cylinder explored by large eddy simulation. *Journal of Fluid Mechanics*, vol. 676, 2011, p. 294–317, Cambridge University Press.
- [KUM 18] KUMAR A., RAY R. K.
Numerical simulation of flow around square cylinder with an inlet Shear in a Closed Channel. *Applications of Fluid Dynamics*, p. 297–304 2018.
- [LAR 17] LARUELLE S., FOSSIER C., CHANGENET C., VILLE F., KOECHLIN S.
Experimental investigations and analysis on churning losses of splash lubricated spiral bevel gears. *Mechanics & Industry*, vol. 18, 2017, p. 412.
- [LEB 09] LEBLANC A., NELIAS D., DEFAYE C.
Nonlinear dynamic analysis of cylindrical roller bearing with flexible rings. *Journal of Sound and Vibration*, vol. 325, n° 1-2, 2009, p. 145–160, Elsevier.
- [LEV 12] LEVOLD P.
Viscous Flow Around Finite Length Circular Cylinder. Master's thesis, Institutt for marin teknikk, 2012.
- [LIE 15] LIEBRECHT J., SI X., SAUER B., SCHWARZE H.
Investigation of drag and churning losses on tapered roller bearings. *Journal of Mechanical Engineering*, vol. 61, 2015, p. 399–408.
- [LIU 13] LIU Z., ZHAO J., HU J., LU Y.
A numerical model for unsteady oil film motion in aero-engine bearing chambers and experimental verification. *ASME 2013 Gas Turbine India Conference* American Society of Mechanical Engineers, 2013, p. V001T04A007–V001T04A007.
- [LIU 17a] LIU H., JURKSCHAT T., LOHNER T., STAHL K.
Determination of oil distribution and churning power loss of gearboxes by finite volume CFD method. *Tribology International*, vol. 109, 2017, p. 346–354, Elsevier.

- [LIU 17b] LIU Y., GUAN X., XU C.
A production limiter study of SST-SAS turbulence model for bluff body flows. *Journal of Wind Engineering and Industrial Aerodynamics*, vol. 170, 2017, p. 162–178.
- [MAL 14] MALLICK M., KUMAR A.
Study on drag coefficient for the flow past a cylinder. *International Journal of Civil Engineering Research*, vol. 5, n° 4, 2014, p. 301–306.
- [MAR 11] MARCHESSE Y., CHANGENET C., VILLE F., VELEX P.
Investigations on CFD simulations for predicting windage power losses in spur gears. *Journal of Mechanical Design*, vol. 133, n° 2, 2011, p. 024501, American Society of Mechanical Engineers.
- [MAR 14a] MARCHESSE Y., CHANGENET C., VILLE F.
Numerical investigations on drag coefficient of balls in rolling Element Bearing. *Tribology Transactions*, vol. 57, 2014, p. 778–785.
- [MAR 14b] MARCHESSE Y., VOELTZEL N., CHANGENET C., VILLE F., VELEX P.
Investigations on CFD simulation for predicting windage power losses generated by helical gears. *2014 STLE Annual Meeting and Exhibition*, 2014, p. CD–Rom.
- [MAR 15] MARCHESSE Y., CHANGENET C., VILLE F., VELEX P.
Numerical investigation of the cage and rings influence on the ball drag coefficient. *STLE 70th Annual Meeting & Exhibition*, 2015.
- [MÉN 07] MÉNARD T., TANGUY S., BERLEMONT A.
Coupling level set/VOF/ghost fluid methods: Validation and application to 3D simulation of the primary break-up of a liquid jet. *International Journal of Multiphase Flow*, vol. 33, n° 5, 2007, p. 510–524, Elsevier.
- [MEN 10] MENTER F., EGOROV Y.
The scale-adaptive simulation method for unsteady turbulent flow predictions. Part 1: theory and model description. *Flow, Turbulence and Combustion*, vol. 85, n° 1, 2010, p. 113–138, Springer.
- [MIC 16] MICHAELIDES E., FENG Z.
Fundamentals of Multiphase Flow. *Multiphase Flow Handbook, Second Edition*. CRC Press Taylor & Francis Group, , 2016, p. 1–78.
- [NEL 73] NELKA J. J.
Evaluation of a rotating disk apparatus: drag of a disk rotating in a viscous fluid. rapport, 1973, DAVID W TAYLOR NAVAL SHIP RESEARCH AND DEVELOPMENT CENTER BETHESDA MD SHIP PERFORMANCE DEPT.
- [NEL 94] NELIAS D., SEABRA J., FLAMAND L., DALMAZ G.
Power Loss Prediction in High-Speed Roller Bearings. *Tribology Series*, vol. 27, p. 465–478 Elsevier, 1994.

- [NIC 17] NICHOLSON B. D., GIVAN G. D., THOMPSON K. L., MASON J., GUPTA P. K., TRIVEDI H. K.
Assessment of Bearing Heat Generation Prediction by the Program ADORE With Respect to Experimental Results and SHABERTH Predictions. *ASME Turbo Expo*, 2017, p. V001T01A001.
- [OKA 73] OKAMOTO T., YAGITA M.
The experimental investigation on the flow past a circular cylinder of finite length placed normal to the plane surface in a uniform stream. *Bulletin of JSME*, vol. 16, n° 95, 1973, p. 805–814, The Japan Society of Mechanical Engineers.
- [O'R 96] O'ROURKE P., AMSDEN A.
A particle numerical model for wall film dynamics in port-injected engines. rapport, 1996, SAE Technical Paper.
- [OSH 01] OSHER S., FEDKIW R. P.
Level set methods: an overview and some recent results. *Journal of Computational physics*, vol. 169, n° 2, 2001, p. 463–502, Elsevier.
- [PAL 10] PALAU-SALVADOR G., STOESSER T., FRÖHLICH J., KAPPLER M., RODI W.
Large eddy simulations and experiments of flow around finite-height cylinders. *Flow, turbulence and combustion*, vol. 84, n° 2, 2010, p. 239, Springer.
- [PAR 84] PARKER R. J.
Comparison of predicted and experimental thermal performance of angular-contact ball bearings. , 1984.
- [PAR 98] PARK J., KWON K., CHOI H.
Numerical solutions of flow past a circular cylinder at Reynolds numbers up to 160. *KSME international Journal*, vol. 12, n° 6, 1998, p. 1200–1205, Springer.
- [PAR 00] PARK C.-W., LEE S.-J.
Free end effects on the near wake flow structure behind a finite circular cylinder. *Journal of Wind Engineering and Industrial Aerodynamics*, vol. 88, n° 2-3, 2000, p. 231–246, Elsevier.
- [PAT 85] PATEL V. C., RODI W., SCHEUERER G.
Turbulence models for near-wall and low Reynolds number flows-a review. *AIAA journal*, vol. 23, n° 9, 1985, p. 1308–1319.
- [PAT 05] PATTENDEN R., TURNOCK S., ZHANG X.
Measurements of the flow over a low-aspect-ratio cylinder mounted on a ground plane. *Experiments in Fluids*, vol. 39, n° 1, 2005, p. 10–21, Springer.

- [PAT 07] PATTENDEN R., BRESSLOFF N., TURNOCK S., ZHANG X.
Unsteady simulations of the flow around a short surface-mounted cylinder. *International journal for numerical methods in fluids*, vol. 53, n° 6, 2007, p. 895–914, Wiley Online Library.
- [PED 11] PEDUTO D., HASHMI A. A., DULLENKOPF K., BAUER H.-J., MORVAN H.
Modelling of an aero-engine bearing chamber using enhanced CFD technique. *ASME 2011 Turbo Expo: Turbine Technical Conference and Exposition* American Society of Mechanical Engineers, 2011, p. 809–819.
- [POU 10a] POULY F.
Modélisation thermo mécanique d'un roulement à billes grande vitesse. Thèse de doctorat, Villeurbanne, INSA, 2010.
- [POU 10b] POULY F., CHANGENET C., VILLE F., VELEX P., DAMIENS B.
Investigations on the power losses and thermal behaviour of rolling element bearings. *Proceedings of the Institution of Mechanical Engineers, Part J: Journal of Engineering Tribology*, vol. 224, n° 9, 2010, p. 925–933, SAGE Publications Sage UK: London, England.
- [PRO 09] PROSPERETTI A., TRYGGVASON G.
Computational methods for multiphase flow. Cambridge university press, 2009.
- [QIA 13] QIAN W.
Dynamic simulation of cylindrical roller bearings. Thèse de doctorat, Aachen, Techn. Hochsch., Diss., 2013.
- [RAG 80] RAGEN M., CHIU Y., DEROMEDI T., DYBA G., GASSEL S.
User's Manual for SKF Computer Program SHABERTH. *SKF Report No. AT80Y002, US Army Contract DAAK11-79-C-0092*, 1980.
- [ROH 03] ROH S., PARK S.
Vortical flow over the free end surface of a finite circular cylinder mounted on a flat plate. *Experiments in Fluids*, vol. 34, n° 1, 2003, p. 63–67, Springer Nature.
- [ROS 61] ROSHKO A.
Experiments on the flow past a circular cylinder at very high Reynolds number. *Journal of Fluid Mechanics*, vol. 10, n° 3, 1961, p. 345–356, Cambridge University Press.
- [RUM 73] RUMBARGER J., FILETTI E., GUBERNICK D.
Gas turbine engine mainshaft roller bearing-system analysis. *Journal of lubrication technology*, vol. 95, n° 4, 1973, p. 401–416, American Society of Mechanical Engineers.
- [SCH 96] SCHÄFER M., TUREK S., DURST F., KRAUSE E., RANNACHER R.
Benchmark computations of laminar flow around a cylinder. *Flow simulation with high-performance computers II*, p. 547–566 Springer, 1996.

- [SEE 09] SEETHARAMAN S., KAHRAMAN A.
Load-independent spin power losses of a spur gear pair: model formulation. *Journal of Tribology*, vol. 131, n° 2, 2009, p. 022201, American Society of Mechanical Engineers.
- [SEL 11] SELVARAJ A., MARAPPAN R.
Experimental analysis of factors influencing the cage slip in cylindrical roller bearing. *The International Journal of Advanced Manufacturing Technology*, vol. 53, n° 5-8, 2011, p. 635–644, Springer.
- [SHE 04] SHEARD G., THOMPSON M. C., HOURIGAN K.
Flow past a cylinder with free hemispherical ends: Comments on grid independence and wake symmetry characteristics. *Under consideration for presentation at the Fifteenth Australasian Fluid Mechanics Conference*, 2004.
- [SIM 02] SIMMONS K., HIBBERD S., WANG Y., CARE I.
Numerical study of the two-phase air/oil flow within an aero-engine bearing chamber model using a coupled Lagrangian droplet tracking method. *ASME 2002 Pressure Vessels and Piping Conference* American Society of Mechanical Engineers, 2002, p. 325–331.
- [SIN 10] SINGHA S., SINHAMAHAPATRA K.
Flow past a circular cylinder between parallel walls at low Reynolds numbers. *Ocean Engineering*, vol. 37, n° 8-9, 2010, p. 757–769, Elsevier.
- [SOH 15] SOHANKAR A., KHODADADI M., RANGRAZ E.
Control of fluid flow and heat transfer around a square cylinder by uniform suction and blowing at low Reynolds numbers. *Computers & Fluids*, vol. 109, 2015, p. 155–167, Elsevier.
- [SUM 04] SUMNER D., HESELTINE J., DANSEREAU O.
Wake structure of a finite circular cylinder of small aspect ratio. *Experiments in Fluids*, vol. 37, n° 5, 2004, p. 720–730, Springer.
- [SUM 13] SUMNER D.
Flow above the free end of a surface-mounted finite-height circular cylinder: a review. *Journal of Fluids and Structures*, vol. 43, 2013, p. 41–63, Elsevier.
- [SUN] SUNDEN B.
TUBES, CROSSFLOW OVER. *A-to-Z Guide to Thermodynamics, Heat and Mass Transfer, and Fluids Engineering* Begellhouse.
- [SUN 09] SUN W., ZHAO J., DI J., WANG Q., WANG L.
Real-time visualization of Karman vortex street in water flow field by using digital holography. *Optics express*, vol. 17, n° 22, 2009, p. 20342–20348, Optical Society of America.

- [SUS 98] SUSSMAN M., FATEMI E., SMEREKA P., OSHER S.
An improved level set method for incompressible two-phase flows. *Computers & Fluids*, vol. 27, n° 5-6, 1998, p. 663–680, Elsevier.
- [TOR 00] TORNBERG A.-K., ENGQUIST B.
A finite element based level-set method for multiphase flow applications. *Computing and Visualization in Science*, vol. 3, n° 1-2, 2000, p. 93–101, Springer.
- [TRA 00] TRAVIN A., SHUR M., STRELETS M., SPALART P.
Detached-eddy simulations past a circular cylinder. *Flow, Turbulence and Combustion*, vol. 63, n° 1-4, 2000, p. 293–313, Springer.
- [TSU 11] TSUKROV I., DRACH A., DECEW J., SWIFT M. R., CELIKKOL B.
Characterization of geometry and normal drag coefficients of copper nets. *Ocean Engineering*, vol. 38, n° 17-18, 2011, p. 1979–1988, Elsevier.
- [TUM 17] TUMKUR R. K. R., PEARLSTEIN A. J., MASUD A., GENDELMAN O. V., BLANCHARD A. B., BERGMAN L. A., VAKAKIS A. F.
Effect of an internal nonlinear rotational dissipative element on vortex shedding and vortex-induced vibration of a sprung circular cylinder. *Journal of Fluid Mechanics*, vol. 828, 2017, p. 196–235, Cambridge University Press (CUP).
- [VAK 09] VAKIL A., GREEN S. I.
Drag and lift coefficients of inclined finite circular cylinders at moderate Reynolds numbers. *Computers & Fluids*, vol. 38, n° 9, 2009, p. 1771–1781, Elsevier.
- [VON 46] VON KARMAN T.
On laminar and turbulent friction. , 1946, National Advisory Committee on Aeronautics.
- [WEH 15] WEHINGER G. D., EPPINGER T., KRAUME M.
Detailed numerical simulations of catalytic fixed-bed reactors: Heterogeneous dry reforming of methane. *Chemical Engineering Science*, vol. 122, 2015, p. 197–209, Elsevier.
- [WIL 93] WILCOX D. C. et al.
Turbulence modeling for CFD, vol. 2. DCW industries La Canada, CA, 1993.
- [WU 16] WU W., HU C., HU J., YUAN S.
Jet cooling for rolling bearings: Flow visualization and temperature distribution. *Applied Thermal Engineering*, vol. 105, 2016, p. 217–224, Elsevier.
- [WU 17] WU W., HU C., HU J., YUAN S., ZHANG R.
Jet cooling characteristics for ball bearings using the VOF multiphase model. *International Journal of Thermal Sciences*, vol. 116, 2017, p. 150–158, Elsevier.

- [XIA 12] XIAO J., ZHU E., WANG G.
Numerical simulation of emergency shutdown process of ring gate in hydraulic turbine runaway. *Journal of Fluids Engineering*, vol. 134, n° 12, 2012, p. 124501, American Society of Mechanical Engineers.
- [XU 14] XU J.-J., HUANG Y., LAI M.-C., LI Z.
A coupled immersed interface and level set method for three-dimensional interfacial flows with insoluble surfactant. *Communications in Computational Physics*, vol. 15, n° 2, 2014, p. 451–469, Cambridge University Press.
- [YAG 16] YAGUO L., JINGYU Z., ZHENXIA L., GUOZHE R.
NUMERICAL STUDY ON THE EFFECT OF OIL REMOVAL FROM AERO-ENGINE BEARING CHAMBER AND IMPROVEMENT. , 2016.
- [YAN 06] YANG X., JAMES A. J., LOWENGRUB J., ZHENG X., CRISTINI V.
An adaptive coupled level-set/volume-of-fluid interface capturing method for unstructured triangular grids. *Journal of Computational Physics*, vol. 217, n° 2, 2006, p. 364–394, Elsevier.
- [YAN 15] YAN K., WANG N., ZHAI Q., ZHU Y., ZHANG J., NIU Q.
Theoretical and experimental investigation on the thermal characteristics of double-row tapered roller bearings of high speed locomotive. *International Journal of Heat and Mass Transfer*, vol. 84, 2015, p. 1119–1130, Elsevier.
- [YAN 16a] YAN K., WANG Y., ZHU Y., HONG J., ZHAI Q.
Investigation on heat dissipation characteristic of ball bearing cage and inside cavity at ultra high rotation speed. *Tribology International*, vol. 93, 2016, p. 470–481, Elsevier.
- [YAN 16b] YAN K., ZHANG J., HONG J., WANG Y., ZHU Y.
Structural optimization of lubrication device for high speed angular contact ball bearing based on internal fluid flow analysis. *International Journal of Heat and Mass Transfer*, vol. 95, 2016, p. 540–550, Elsevier.
- [YAN 17] YAN K., WANG Y., ZHU Y., HONG J.
Investigation on the effect of sealing condition on the internal flow pattern of high-speed ball bearing. *Tribology International*, vol. 105, 2017, p. 85–93, Elsevier.
- [ZAC 16] ZACHARZEWSKI P., SIMMONS K., JEFFERSON-LOVEDAY R., CAPONE L.
Evaluation of the SST-SAS model for prediction of separated flow inside turbine internal cooling passages. *ASME Turbo Expo*, 2016, p. V05BT11A003.
- [ZDR 89] ZDRAVKOVICH M., BRAND V., MATHEW G., WESTON A.
Flow past short circular cylinders with two free ends. *Journal of fluid mechanics*, vol. 203, 1989, p. 557–575, Cambridge University Press.

- [ZDR 03] ZDRAVKOVICH M. M.
Flow around Circular Cylinders: Volume 1: Applications. Oxford university press, 2003.
- [ZHA 14] ZHAO J., LIU Z., HU J., LU Y.
Motion of wall oil film with consideration of oil-gas coupled heat and mass transfer in the bearing chamber. *J Propul Technol*, vol. 35, 2014, p. 973–80.
- [ZHA 15] ZHAO J., LIU Z., LU Y., HU J.
Numerical modeling of unsteady oil film motion characteristics in bearing chambers. *International Journal of Turbo & Jet-Engines*, vol. 32, 2015, p. 233–245.
- [ZHO 14] ZHONG C., HU J.-P., LIU Z.-X., LU Y.-G., HAO Y.-Y.
Application of the Ultrasonic Oil Film Thickness Measurement System in Bearing Chambers. *International Journal of Turbo & Jet-Engines*, vol. 31, n° 2, 2014, p. 159–165, De Gruyter.
- [ZHU 17] ZHU L., LIM H.-C.
Hydrodynamic characteristics of a separated heave plate mounted at a vertical circular cylinder. *Ocean Engineering*, vol. 131, 2017, p. 213–223, Elsevier BV.



FOLIO ADMINISTRATIF

THESE DE L'UNIVERSITE DE LYON OPEREE AU SEIN DE L'INSA LYON

NOM : GAO

DATE de SOUTENANCE : 27 Juin 2018

Prénoms : Wenjun

TITRE : Modelling of windage and churning losses in high speed rolling element bearings

NATURE : Doctorat

Numéro d'ordre : 2018LYSEI048

Ecole doctorale : Mécanique, Énergétique, Génie Civil, Acoustique (ED 162 MEGA)

Spécialité : MÉCANIQUE – GÉNIE MÉCANIQUE – GÉNIE CIVIL

RESUME : In a rotating machinery system like turbine engine, high speed rolling element bearings play an important role in supporting the rotating shaft or rotor, and need lubrication to insure their function. Except a small quantity of oil is needed to form the elastohydrodynamic lubricant film in the contact zone, most of lubricant remains in suspension in air, forming an oil/air mixture. This phenomenon leads to excessive parasitic hydraulic losses when rolling elements translate and rotate into the fluid environment, which may constitute a relatively large portion of the bearing's total power loss, named windage drag and churning losses. For high speed applications, i.e. for rotational speed up to 3×10^6 Ndm, the contribution of drag/windage loss to the total one may reach up to 50%. However, so far there are few approaches used directly for drag and churning losses estimation, which could only provide a rather gross approximation.

In this thesis, the Computational Fluid Dynamics (CFD) method is employed to analyze first the flow around one finite-length circular cylinder with two free ends in an open space. Then the model is changed to several in-line circular cylinders sandwiched by two flat walls, which represents a simplified approach. The fluid here is regarded as incompressible, representing an equivalent one-phase fluid for the oil/air two-phase flow inside the bearing cavity with specified fluid properties. The results indicate that the flow around the finite length roller element is perturbed by its two free ends, the surrounding rings, the cage and other rolling elements. A relationship between the drag coefficient and the Reynolds number suitable for circular cylinder in roller bearings ($1 < L/D < 6$) is proposed, as well as a formulation for churning losses prediction.

The oil/air two-phase flow inside the bearing cavity with under-race lubrication is also studied in this work. The coupled level-set volume of fluid (CLS-VOF) method is employed to demonstrate the lubricant distribution along the bearing circumference. The effect of various factors is studied, e.g. the oil injection velocity, the nozzle diameter, the oil properties, and the oil injecting angle. Rotational speed of all the bearing components are studied particularly to quantify their influence to the oil volume fraction inside the bearing cavity. The results demonstrate that not only the inner-ring relative rotational speed, but the cage speed itself could change the oil distribution. The results can be used for the precise lubrication design to optimize the oil distribution inside the bearing.

MOTS-CLÉS : Numerical simulation, Rolling element bearing, Drag coefficient, Churning moment, Finite length, Free ends, Reynolds number, Oil volume fraction, Two-phase flow

Laboratoire (s) de recherche : Laboratoire de Mécanique des Contacts et des Structures, UMR CNRS 5259 – INSA de Lyon

Directeur de thèse: Daniel NELIAS

Président de jury : Yann Marchesse

Composition du jury : Mihai ARGHIR
Lifen ZHANG
Daniel NELIAS
Damien LECOUVREUR

Jean-Luc BOZET
Yann MARCHESSE
Nicolas BOISSON